HOLLOW-CORE FIBER ASSISTED HIGH SENSITIVITY SPECTROSCOPIC GAS SENSING

CHEN FEIFAN

PhD

The Hong Kong Polytechnic University

2023

The Hong Kong Polytechnic University

Department of Electrical and Electronic Engineering

Hollow-core fiber assisted high sensitivity spectroscopic gas sensing

Chen Feifan

A thesis submitted in partial fulfillment of the requirements for the degree of Doctor of Philosophy

July 2023

CERTIFICATE OF ORIGINALITY

I hereby declare that this thesis is my own work and that, to the best of my knowledge and belief, it reproduces no material previously published or written, nor material that has been accepted for the award of any other degree or diploma, except where due acknowledgement has been made in the text.

(Signed)

Chen Feifan
(Name of student)

Abstract

Among various gas sensing technologies, laser absorption spectroscopy (LAS) stands out due to its advantages in sensitivity and selectivity. Hollow-core fiber (HCF) has been proven to be an efficient platform for light-gas interactions. Although HCF-based LAS was first demonstrated in 2004, its sensitivity long remained at the tens of parts per million (ppm) level. In 2015, the first HCF-based gas sensor with parts-per-billion (ppb) level sensitivity was demonstrated using photothermal spectroscopy (PTS) with near-infrared (NIR) pump.

It is well known that gas molecules have stronger absorption in the mid-infrared (MIR) due to fundamental vibrational absorption. Thus, we employ a MIR pump to access the strongest absorption lines for high sensitivity but still use a NIR probe for cost-effective high-performance fiber-optic circuits. We demonstrate the use of a HCF Fabry-Perot interferometer (FPI) to detect photothermal (PT) phase modulation. A 14-cm-long anti-resonant HCF is used and ethane detection with a limit of detection (LOD) of 2.6 ppb with 410 s averaging time is achieved. Through noise analysis, we have concluded that the FPI structure requires a probe laser with narrow linewidth.

Apart from the single-component gas detection, we also demonstrate simultaneous detection of multiple gases with FPI-PTS using a single HCF gas cell. Our system utilizes three pump lasers with wavelengths of 1.39 μm, 2.00 μm, and 4.60 μm, corresponding to the absorption lines of H_2O, CO_2, and CO. These lasers were frequency-division multiplexed (FDM) to generate PT phase modulations simultaneously at different frequencies. A common probe FPI operating at 1.55 μm is used to detect the phase modulations. This simple system combines multiple pump beams from NIR to MIR for the most efficient interaction among the gas sample, the pump beams, and the probe beam in the same gas cell, minimizing the usage of expensive MIR components.

Phase noise is dominant due to the long optical path difference (OPD) between the interference beams in FPI structure. We then demonstrate the use of an in-fiber dual-mode interferometer (DMI) as the probe. The DMI has a much smaller OPD, and hence, smaller phase noise level. A gas sensing method named MIR reflective DMI-PTS is then demonstrated. With a 1.8-m-long double-pass HCF gas cell and a 3.27 μm pump source, a noise-equivalent absorption coefficient (NEA) of 2.16×10^{-9} cm^{-1} is achieved. According to the noise analysis, this system is near shot-noise limited after using a balanced detector.

For gases with no strong optical absorption but Raman active, Raman spectroscopy offers a solution for tracing them. We demonstrate cavity-enhanced stimulated Raman gain spectroscopy (CE-SRGS) for hydrogen detection. The combination of a high-finesse cavity with a HCF has enabled us to demonstrate high sensitivity hydrogen detection with a short sensing length. With the Stokes light locked to an 8-cm-long HCF cavity of 300 finesses, the enhancement factor of 100 has been achieved. Targeting the $Q_1(1)$ transition, we achieved a LOD of 62 ppm using 1 s time constant at 1 atm, making our results comparable with the best existing hydrogen sensors.

Acknowledgements

I would like to express my heartfelt gratitude to Professor Wei Jin for providing me with the invaluable opportunity to collaborate with him and the exceptional colleagues in his research group. Professor Jin's unwavering dedication to intellectual rigor and integrity has served as a constant source of inspiration throughout my journey. Under his mentorship, generous support, and patient guidance, I have experienced tremendous personal and professional growth as a researcher. I am committed to carrying forward the spirit of curiosity and exploration that he has instilled in me as I embark on my future career.

I extend my special thanks to Dr. Shoulin Jiang and Dr. Haihong Bao for their enlightening discussions and kind assistance, particularly during the initial stages of my Ph.D. project. Your expertise and support have been invaluable in shaping my research.

I would also like to acknowledge the contributions of Dr. Hoi Lut Ho, Dr. Chao Wang, Dr Kaiyuan Zheng, Dr. Shuangxiang Zhao, Dr. Yan Zhao, Dr. Yun Qi, Dr. Pengcheng Zhao, Dr. Han Gao, Dr. Tianye Zheng. Mr. Hanyu Liao, Mr. Linhao Guo and Miss Yingzhen Hong, and Your support, both academically and personally, has been instrumental in my studies and daily life.

Lastly, I want to express my heartfelt gratitude to my beloved family for their unwavering love and support. Their encouragement and belief in me have been the driving force behind my achievements.

Publications Arising from the Thesis

Journal articles

[1] **Chen, F.**, Jiang, S., Ho, H. L., Gao, S., Wang, Y., & Jin, W. (2022). Frequency-Division Multiplexed Multicomponent Gas Sensing with Photothermal Spectroscopy and a Single NIR/MIR Fiber-Optic Gas Cell. Analytical Chemistry, 94(39), 13473-13480.

[2] **Chen, F.**, Jiang, S., Jin, W., Bao, H., Ho, H. L., Wang, C., & Gao, S. (2020). Ethane detection with mid-infrared hollow-core fiber photothermal spectroscopy. Optics Express, 28(25), 38115-38126.

[3] **Chen, F. (co-first author),** Hong, Y., Bao, H., Jin, W., Jiang, S., Ho, H. L., Gao, S., Wang, Y., Amplified photothermal phase modulation for carbon dioxide detection by operating a dual-mode interferometer at destructive interference. Analytical Chemistry, 2023 95 (8), 4204-4211.

[4] Jiang, S., **Chen, F.**, Zhao, Y., Gao, S., Wang, Y., Ho, H. L., & Jin, W. (2022). Broadband all-fiber optical phase modulator based on photo-thermal effect in a gas-filled hollow-core fiber. Opto-Electronic Advances, 220085-1.

[5] 姜寿林, 靳伟, **陈非凡**, 高寿飞, & 何海律. (2021). 基于空芯光纤光热光谱技术的高灵敏度 CO_2 检测. 光学学报, 41(13), 1306004.

Conference articles

[1] **Chen, F.**, et al. “Mid-infrared reflective mode-phase-difference photothermal spectroscopy for methane detection in a hollow-core fiber”, the 27th International Conference on Optical Fiber Sensors, Sept. 1, 2022.

[2] **Chen, F.**, et al. “Ppb-level ethane detection with hollow-core fiber photothermal spectroscopy”, the 26th Optoelectronics and Communications Conference, July 5, 2021.

[3] Hong, Y., **Chen, F.**, Bao, H., Gao, S., Ho, H. L., Wang, Y., Jin, W., “Sensitivity Enhancement of Photothermal gas Detection via Optical Phase-Modulation Amplification” the 27th International Conference on Optical Fiber Sensors, Sept. 2, 2022.

Table of Contents

List of Figures

List of Tables

List of Acronyms

AOM	acousto-optic modulator
AR-HCF	anti-resonant hollow-core fiber
BPD	balanced detector
CE-SRGS	cavity-enhanced stimulated Raman gain spectroscopy
DAS	direct absorption spectroscopy
DFB	distributed feedback
DMI	dual-mode interferometer
ECDL	external cavity diode lasers
EOM	electro-optic modulator
FDM	frequency-division-multiplexing
FG	function generator
FMS	frequency modulation spectroscopy
FPI	Fabry-Perot interferometer
FWHM	full-width at half-maximum
GMS	gas mixing system
HCF	hollow-core fiber
HC-PBF	hollow-core photonic bandgap fiber
HWHM	half width at half maximum
ICL	inter-band cascade laser
IM	intensity modulation
IR	infrared
LIA	lock-in amplifier
LOD	limit of detection
MFD	mode field diameter
MI	mode interference
MPD	mode-phase-difference
NEA	noise-equivalent absorption coefficient
NEC	noise equivalent concentration
NICE-OHMS	noise-immune cavity-enhanced optical heterodyne molecular spectroscopy
OC	optical circulator
OPMA	optical-phase modulation amplifying
OSA	optical spectrum analyzer
PAS	photoacoustic spectroscopy
PC	polarization controller
PD	photodetector
PDH	Pound-Drever-Hall
ppb	parts-per-billion
ppm	parts-per-million
ppt	parts-per-trillion
PTS	photothermal spectroscopy
QCL	quantum cascade laser
RI	refractive index
RMS	root-mean-square
RPTS	Raman photothermal spectroscopy
SCCM	standard cubic centimeter per minute
SEM	scanning electron microscopy
SMF	single mode fiber

SNR	signal-to-noise ratio
SRD	stimulated Raman induced dispersion
SRG	stimulated Raman gain
SRGS	stimulated Raman gain spectroscopy
SRL	stimulated Raman loss
SRS	stimulated Raman scattering
TC	time constant
TDLAS	tunable diode laser absorption spectroscopy
TDM	time-division-multiplexing
TECF	thermally expanded core fiber
VRT	vibrational relaxation time
WDM	wavelength division multiplexer
WMS	wavelength modulation spectroscopy

List of Symbols

α	absorption coefficient
α_{FI}	polarizability tensor of molecule
β	modulation index of optical phase
γ_n	natural HWHM linewidth
γ_D	Doppler 1/e half-linewidth
γ_l	Lorentzian HWHM linewidth
γ_{air}	air-broadened HWHM linewidth
γ_{self}	self-broadened HWHM linewidth
γ_{FI}	polarizability anisotropy
γ_R	FWHM Raman linewidth
ΔN_{fi}	density difference between the initial state i and the final state f
c	speed of light in the vacuum
C	concentration of absorptive gas
C_p	specific heat capacity
D_{LIA}	Detection bandwidth of lock-in amplifier
ε_0	vacuum permittivity
g_R	Raman gain coefficient
η_{PD}	responsibility of photodetector
η_H	efficiency of heat generation
k_B	Boltzmann constant
κ	gas thermal conductivity
k^*	phase modulation coefficient
$J_k\left(\beta\right)$	Bessel functions
N_A	Avogadro's number
N_g	number density of the target gas molecules
N_0	molecular density under Normal Temperature and Pressure
τ_V	vibrational relaxation time
σ	absorption cross-section

Chapter 1

1 Introduction

1.1 Background

Gas sensing is import in several domains, such as environmental surveillance and respiratory testing [1-4]. Many techniques have been applied to achieve quantitative gas sensing, like gas chromatography (GS) [5], semiconductor or electrochemical gas sensors (SEGS) [6], and pellistors [7]. Each approach bears unique merits and demerits: GS has unparalleled sensitivity and selectivity in the way of isolating individual components through metallic, yet its incapacity for real-time measurement stands as a significant drawback. In contrast, SEGS presents a cost-efficient and compact solution, yielding notable sensitivity down to ppm or ppb levels, despite wrestling with issues like gas cross effect, and restricted service life.

Optical gas sensing techniques, using the principles of light-gas interaction, are highly sensitive and have excellent selectivity while facilitating contactless measurements. With the swift progress of laser technology, optical gas sensing has seen substantial growth. Broadly, optical gas sensing techniques are bifurcated into two groups: those which gauge the difference in laser intensity, as exemplified by tunable diode laser absorption spectroscopy (TDLAS) [8] and Raman spectroscopy [9]; and those which probe the indirect effects, such as photoacoustic spectroscopy [10] (PAS) and photothermal spectroscopy (PTS) [11]. Common optical LAS often utilizes laser modulation techniques that include wavelength, frequency [12], and intensity modulation [13]. These modulation techniques change the sensing frequency to a few kHz or MHz , effectively reducing frequency noise. [12, 13]. Multi-pass gas cell[14], and optical cavity [15] constitute a crucial component of LAS, bolstering detection limit by augmenting the effective length.

In these LAS techniques, noise-immune cavity-enhanced optical heterodyne molecular spectroscopy (NICE-OHMS) has emerged as best one, accomplishing ppt-level sensitivity. Despite the benefits offered by NICE-OHMS, it encounters limitations in increasing sensitivity further due to the saturation power limitations of photodetectors, and the intricate optical alignment prerequisites of high-finesse cavities pose challenges for their operation in rough environments [15].

LAS techniques which assess the indirect effects of light absorption are able to attain remarkable sensitivity, using shorter effective length. For instance, PAS and PTS evaluate the sound wave and refractive index (RI) changes, respectively. The sound wave can be detected using a microphone, while the RI change via an optical interferometer. A range of microphones has been developed to enhance acoustic detection sensitivity in PAS, such as quartz-tuning forks [16], cantilever-type microphones [17], and fiber-tip-based microphones [18]. Furthermore, the acoustic wave induced by absorption could be amplified using a cavity to achieve superior detection limit [19].

Traditional LAS relies on bulk gas chambers, like Herriott gas cells or gas cavity. Maintaining the performance of these gas cells over extended periods in real-world environments proves difficult due to the need for meticulous adjustments or complex locking methods. The invention of hollow-core fibers (HCFs) demonstrated their effectiveness as a platform for long-distance light-gas interactions [20]. HCFs could be used to improve the sensitivity of conventional spectroscopies.

HCF-based gas cells can be seamlessly connected to single-mode fibers [21, 22]. As a result, HCFs have unlocked new possibilities for gas detection applications, overcoming the limitations of traditional bulky optical gas cell-based spectroscopy methods.

By capitalizing on the unique characteristics of HCFs, researchers and engineers can develop more sensitive, reliable, and versatile gas detection systems for a wide array of applications [23]. The integration of HCFs with optical gas spectroscopy methods holds the potential to revolutionize the field, culminating in gas detection systems that are better suited to address the diverse requirements of various industries and applications.

In conclusion, the integration of hollow-core fibers (HCFs) with optical gas spectroscopy methods marks a significant advancement in gas detection across various fields [20]. HCFs overcome the limitations of traditional gas cell-based spectroscopy methods, providing improved performance in terms of sensitivity, reliability, and versatility. Consequently, HCFs are paving the way for the development of more effective and practical gas detection systems that cater to the diverse needs of multiple industries and applications. The potential impact of HCFs in the field of gas detection is immense, as they enable innovative and efficient solutions for monitoring and controlling air quality, ensuring safety in industrial settings, and facilitating accurate medical diagnostics. As research and development in this area continue to progress, the incorporation of HCFs with optical gas spectroscopy methods will undoubtedly lead to more robust and adaptable gas detection systems, better equipped to meet the ever-evolving demands of our modern world [24].

1.2 Literature review

Cregan first proposed using a hollow-core photonic bandgap fiber (HC-PBF) to build up an efficient cells in 1999 [25], with the initial exploration of HC-PBF gas cells reported around 2004 [26]. These fibers offer high light-gas interaction efficiency by confining light and molecules within their core. Additionally, they are suitable for creating practical, compact, and user-friendly all-fiber devices and systems. A typical HC-PBF's transmission window can be designed to work near 1550 nm, which includes the fairly strong absorption lines of various gases, enabling integration with commom single-mode fiber components.

Hoo first reported the investigation of gas diffusion processes within HC-PBFs in 2005 [26]. Numerous studies have since been conducted, exploring the potential of HC-PBF sensors [27]. However, mode interference (MI) noises have limited the ultimate sensitivity of these sensors when using direct absorption spectroscopy (DAS) [28].

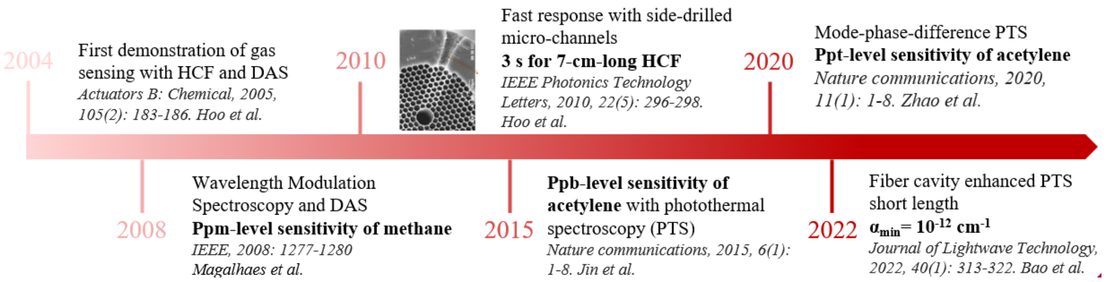

Figure 1.1 Timelines of gas sensing with HCFs

Researchers have attempted to increase sensitivity by using longer HC-PBFs, but this approach can significantly compromise response time. Hoo et al. [29] built an optical fiber methane sensor using a 7-cm long HC-PBF with several micro-channels. This sensor has a sensitivity of 647 parts-per-million (ppm) for methane and a response time of 3 seconds.

Instead of measuring spectral attenuations, PTS detects accumulated phase changes caused by the optical absorption of a modulated light. An optical interferometry is used to detect these phase modulations. The PTS with HCF has realized a detection limit of 2 parts-per-billion (ppb) of C_2H_2 in 1530.37 nm using 10-m-long HC-PBFs [30]. This PT gas sensor with HC-PBFs has achieved ultra-sensitivity and an unprecedented dynamic range, significantly surpassing previous HC-PBF ones [29, 31].

In 2018 [32], Zhao et al. demonstrated PTS with a mode-phase-difference (MPD) interferometer achieving sensitive gas sensing over a large dynamic range. By detecting MPD, environmental perturbations effects are minimized, enabling significant enhancements in signal-to-noise ratio (SNR). Utilizing an HCF of several meters, they realized a detection limits lower to parts-per-trillion (ppt) levels and.

Highly sensitive gas sensing using HCF optical phase modulation amplification (OPMA)-PTS was reported by Bao et al in 2022. The all-fibre OPMA-PTS scheme is more compact and less expensive than a free-space cavity. Using different pump lasers, they realizeed the sensing of CH_4, C_2H_2 and O_2 at detection limit of 15 ppt, 2.7 ppt and 0.56 ppm [33].

1.3 Motivation of this work

To date, fiber-optic gas sensing technologies based on LAAS have made significant progress. However, the absorption lines used in most of these techniques are primarily in the NIR region. Indeed, improving sensing sensitivity could be significantly realized by selecting gas absorption in the MIR region. It is in this region that numerous gases display most pronounced absorption characteristics because fundamental rovibrational transitions. Line strengths of these primary transitions are typically much stronger, at least by a hundredfold, compared to their associated overtone transitions. Particular emphasis is placed on the so-called atmospheric window, which spans from 3-5 micrometers as shown in Fig. 1.2. This span holds the strongest absorption bands for compounds like carbohydrates (characterized by C-H stretching) and molecules exhibiting N-H or O-H stretching vibrations [33]. An important detail to note within this atmospheric window is the relatively modest absorption of water vapor. This attribute is crucial for some applications, like in environmental surveillance , in which the presence of abundant water molecules often complicates the spectral measurement of trace gases.

A breakthrough in the technological landscape has been realized through the introduction of quantum cascade lasers (QCLs) and inter-band cascade lasers (ICLs) functioning at ambient temperature[34]. This innovation has successfully broadened the operational reach of tunable semiconductor lasers beyond the visible and NIR spectrum, extending into the MIR territory. Along this trajectory, the evolution of MIR hollow-core optical fibers has substantiated this concept, bringing it to fruition. Nevertheless, the nascent stage of MIR optical devices, especially detectors, poses limitations on the sensitivity of detection. Normally speaking, MIR detectors exhibit inferior noise performance in comparison to their NIR counterparts, unless the detector is sufficiently cooled. Recognizing this inherent challenge, we pioneer the development of a photothermal sensor employing a MIR pump in conjunction with a NIR probe. This hybrid approach harnesses the superior absorption coefficients inherent in the MIR region while mitigating the drawbacks associated with the underdeveloped MIR optical devices. Our initial implementation involves high-precision ethane detection using a simple Fabry-Perot interferometer (FPI) structure with a 3.3 μm pump laser.

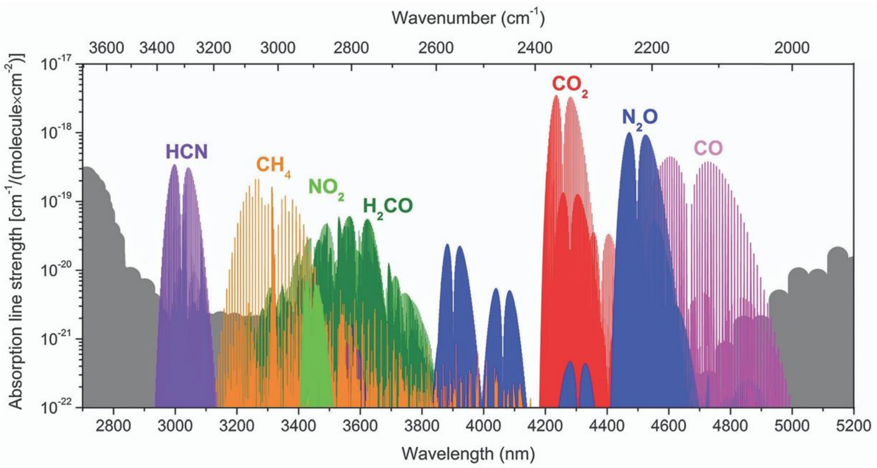

Figure 1.2 Absorption spectra of gases.[33]

Progressing beyond singular gas detection technologies, we demonstrate multi-gas sensing using PTS. The sensor we have developed has a distinctive design that enables simultaneous detection of multiple gas species. One of the key features of our sensor is its capability to combine multiple pump beams spanning the NIR to MIR range within a single gas cell. This design ensures optimal interaction between the gas sample, pump beams, and probe beam, resulting in enhanced efficiency and sensitivity. The system's versatile design offers the latitude to judiciously select pump wavelengths, considering a balance between the strength of gas absorption lines, component performance, and cost-effectiveness. This strategic selection is integral in meeting the diverse requirements of practical applications, demonstrating the real-world potential of our novel multi-gas sensor technology.

In our quest to enhance detection ability, one strategy is to diminish the noise. Our approach employs a dual-mode interferometer (DMI) within the HCF, still using MIR pump and NIR probe. The unique advantage of this DMI is its sensitivity to gas absorption within the hollow-core, coupled with an impressive resilience to external disturbances. This symbiosis significantly boosts the SNR. Importantly, the DMI exhibits insensitivity to laser phase noise due to short optical path difference, which allows us to leverage longer optical fibers to elevate system detection sensitivity. When compared with a FPI of the same length, the dual-mode interferometer has lower optical noise and is more stable.

Beyond the realm of gases with strong absorption in the IR region, some gases showcase little or no absorption, which renders conventional absorption spectroscopy techniques ineffective in terms of sensitivity and specificity. To counter this issue, we explore Raman spectroscopy as an alternative means for measuring these gases. In recent years, stimulated Raman gain spectroscopy (SRGS) based on HC-PBFs has shown promise. These systems typically employ lengthy HCFs, up to tens of meters, to enhance detection performance. However, these systems are largely restricted by residual MI within the HCF[35]. Concurrently, the requirement for high pressure to push the gas sample into such a lengthy fiber is impractical for many applications. Addressing these limitations, we adopted an anti-resonant HCF (AR-HCF) for its superior single-mode performance and opted for a shorter fiber length, about 8 cm, to reduce the gas filling time. By implementing cavity enhancement, we effectively increased the interaction distance between the gas and light, thereby enabling high sensitivity hydrogen detection. This cavity-enhanced SRGS (CE-SRGS) presents a practical and efficient alternative for sensing gases that exhibit weak absorption in the IR region but are Raman active.

1.4 Outlines

The structure of the thesis is the following:

In **chapter 1**, we explore the background of gas detection and review the current developments in gas detection technologies, with a particular focus on optical-based detection methods and their associated historical progression. We also introduce the motivation behind this research, emphasizing the need for advanced sensing techniques that can address the increasing demands for accurate and reliable gas detection in various application fields.

Chapter 2 provides a comprehensive exploration of gas sensing fundamentals. We demystify the principles of gas molecular absorption spectroscopy, introduce key concepts of modulation techniques like intensity, wavelength and frequency modulation, and delve into photothermal and Raman spectroscopy. This foundational understanding paves the way for accurate and efficient gas detection and analysis.

In **chapter 3**, we demonstrate the utility of MIR HCF PTS that utilizes an FPI for high sensitivity detection of a single gas. i.e., ethane. Additionally, we dissect and examine the noise sources associated with the FPI, offering crucial insights into the variables that affect the efficacy of this optical gas sensing approach.

In **chapter 4**, we explore the use of FPI for simultaneous sensing of multi-component gases by using hybrid MIR/NIR pumps with frequency-division-multiplexing (FDM). Beneficially, our system's simultaneous detection capabilities enable us to investigate the impact of H_2O concentration on photothermal signals. Using the derived correlation, we can calibrate the photothermal signals of gases at different humidity levels.

In **chapter 5**, we demonstrate further enhancement of detection sensitivity by implementing a reflective DMI with a NIR probe source and a MIR pump. We analyze the noise sources and discuss its insensitivity to external disturbances. Leveraging this system configuration, we demonstrate measurement of methane at the ppt level.

In **chapter 6**, we detail our exploration into the detection of Raman-active gases, like hydrogen, using CE-SRGS. We study the effects of variations in polarization and gas pressures on the Raman gain for hydrogen. We also analyze the magnifying impact of the HCF cavity on SRGS. By merging the HCF cavity with SRGS, we demonstrate significantly enhanced Raman signal and realize highly sensitive hydrogen detection.

In **chapter 7**, we summarize the thesis and discuss future works.

1.5 Reference

1. G. A. WATCH, "WMO Global Atmosphere Watch (GAW) Strategic Plan: 2008–2015," (2011).
2. P. Paredi, S. A. Kharitonov, and P. J. Barnes, "Elevation of exhaled ethane concentration in asthma," American journal of respiratory and critical care medicine **162**, 1450-1454 (2000).
3. B. K. Puri, B. M. Ross, and I. H. Treasaden, "Increased levels of ethane, a non-invasive, quantitative, direct marker of n-3 lipid peroxidation, in the breath of patients with schizophrenia," Progress in Neuro-Psychopharmacology and Biological Psychiatry **32**, 858-862 (2008).
4. K. Skeldon, L. McMillan, C. Wyse, S. Monk, G. Gibson, C. Patterson, T. France, C. Longbottom, and M. Padgett, "Application of laser spectroscopy for measurement of exhaled ethane in patients with lung cancer," Respiratory medicine **100**, 300-306 (2006).
5. K. D. Bartle, and P. Myers, "History of gas chromatography," TrAC Trends in Analytical Chemistry **21**, 547-557 (2002).
6. F. Wang, and S. Hu, "Electrochemical sensors based on metal and semiconductor nanoparticles," Microchimica Acta **165**, 1-22 (2009).
7. P. Moseley, "Solid state gas sensors," Measurement Science and technology **8**, 223 (1997).
8. M. Lackner, "Tunable diode laser absorption spectroscopy (TDLAS) in the process industries–a review," Reviews in Chemical Engineering **23**, 65-147 (2007).
9. X. Yang, A. S. Chang, B. Chen, C. Gu, and T. C. Bond, "High sensitivity gas sensing by Raman spectroscopy in photonic crystal fiber," Sensors and Actuators B: Chemical **176**, 64-68 (2013).
10. A. Rosencwaig, "Photoacoustic spectroscopy," Annual review of biophysics and bioengineering **9**, 31-54 (1980).
11. S. E. Bialkowski, *Photothermal spectroscopy methods for chemical analysis* (John Wiley & Sons, 1996).
12. J. M. Supplee, E. A. Whittaker, and W. Lenth, "Theoretical description of frequency modulation and wavelength modulation spectroscopy," Appl. Opt. **33**, 6294-6302 (1994).
13. B. Lang, "Laser intensity modulation method (LIMM): review of the fundamentals and a new method for data analysis," IEEE transactions on dielectrics and electrical insulation **11**, 3-12 (2004).
14. Y. Liu, and Y. Ma, "Advances in multipass cell for absorption spectroscopy-based trace gas sensing technology," Chinese Optics Letters **21**, 033001 (2023).
15. A. Foltynowicz, F. M. Schmidt, W. Ma, and O. Axner, "Noise-immune cavity-enhanced optical heterodyne molecular spectroscopy: Current status and future potential," Applied Physics B **92**, 313 (2008).
16. X. Chen, H. Liu, M. Hu, Z. Xu, H. Deng, X. Fan, and R. Kan, "QEPAS sensor for simultaneously sensitive detection of NH3 and H2S based on frequency-division

multiplexing," in *Eighth Symposium on Novel Photoelectronic Detection Technology and Applications*(SPIE2022), pp. 1888-1895.

17. V. Koskinen, J. Fonsen, K. Roth, and J. Kauppinen, "Progress in cantilever enhanced photoacoustic spectroscopy," Vibrational spectroscopy **48**, 16-21 (2008).

18. Z. Li, Z. Wang, C. Wang, and W. Ren, "Optical fiber tip-based quartz-enhanced photoacoustic sensor for trace gas detection," Applied Physics B **122**, 147 (2016).

19. A. Miklós, P. Hess, and Z. Bozóki, "Application of acoustic resonators in photoacoustic trace gas analysis and metrology," Review of scientific instruments **72**, 1937-1955 (2001).

20. W. Jin, H. Bao, P. Zhao, Y. Zhao, Y. Qi, C. Wang, and H. L. Ho, "Recent advances in spectroscopic gas sensing with micro/nano-structured optical fibers," Photonic Sensors **11**, 141-157 (2021).

21. C. Wang, R. Yu, B. Debord, F. Gérôme, F. Benabid, K. S. Chiang, and L. Xiao, "Ultralow-loss fusion splicing between negative curvature hollow-core fibers and conventional SMFs with a reverse-tapering method," Optics Express **29**, 22470-22478 (2021).

22. J. Nicholson, B. Mangan, L. Meng, A. DeSantolo, P. Vannasouk, E. Warych, and T. Taunay, "Low-loss, low return-loss coupling between SMF and single-mode, hollow-core fibers using connectors," in *CLEO: Applications and Technology*(Optica Publishing Group2014), p. JTu4A. 71.

23. J. Li, H. Yan, H. Dang, and F. Meng, "Structure design and application of hollow core microstructured optical fiber gas sensor: A review," Optics & Laser Technology **135**, 106658 (2021).

24. J. Hodgkinson, and R. P. Tatam, "Optical gas sensing: A review," (2013).

25. R. Cregan, B. Mangan, J. Knight, T. Birks, P. S. J. Russell, P. Roberts, and D. Allan, "Single-mode photonic band gap guidance of light in air," science **285**, 1537-1539 (1999).

26. Y. Hoo, W. Jin, H. Ho, J. Ju, and D. Wang, "Gas diffusion measurement using hollow-core photonic bandgap fiber," Sensors and Actuators B: Chemical **105**, 183-186 (2005).

27. F. Magalhaes, J. Carvalho, L. Ferreira, F. Araújo, and J. Santos, "Methane detection system based on wavelength modulation spectroscopy and hollow-core fibres," in *SENSORS, 2008 IEEE*(IEEE2008), pp. 1277-1280.

28. L. Hu, C. Zheng, D. Yao, D. Yu, Z. Liu, J. Zheng, Y. Wang, and F. K. Tittel, "A hollow-core photonic band-gap fiber based methane sensor system capable of reduced mode interference noise," Infrared Physics & Technology **97**, 101-107 (2019).

29. Y. L. Hoo, S. Liu, H. L. Ho, and W. Jin, "Fast Response Microstructured Optical Fiber Methane Sensor With Multiple Side-Openings," IEEE Photonics Technology Letters **22**, 296-298 (2010).

30. W. Jin, Y. Cao, F. Yang, and H. L. Ho, "Ultra-sensitive all-fibre photothermal spectroscopy with large dynamic range," Nature Communications (2015).

31. F. Yang, W. Jin, Y. Cao, H. L. Ho, and Y. Wang, "Towards high sensitivity gas detection with hollow-core photonic bandgap fibers," Optics express **22**, 24894-24907 (2014).

32. P. Zhao, Y. Zhao, H. Bao, H. L. Ho, W. Jin, S. Fan, S. Gao, Y. Wang, and P. Wang, "Mode-phase-difference photothermal spectroscopy for gas detection with an anti-resonant hollow-core optical fiber," Nature communications **11**, 1-8 (2020).

33. M. Vainio, and L. Halonen, "Mid-infrared optical parametric oscillators and frequency combs for molecular spectroscopy," Physical Chemistry Chemical Physics **18**, 4266-4294 (2016).

34. Y. Yao, A. J. Hoffman, and C. F. Gmachl, "Mid-infrared quantum cascade lasers," Nature Photonics **6**, 432-439 (2012).
35. F. Yang, and W. Jin, "All-fiber hydrogen sensor based on stimulated Raman gain spectroscopy with a 1550 nm hollow-core fiber," in *2017 25th Optical Fiber Sensors Conference (OFS)*(IEEE2017), pp. 1-4.

Chapter 2

2 Basic Principles

This chapter provides a exploration of gas sensing. We demystify the principles of gas molecular absorption spectroscopy, introduce key concepts of modulation techniques, including intensity, wavelength, and frequency, and delve into photothermal and Raman spectroscopy. This foundational understanding paves the way for accurate and efficient gas detection and analysis.

2.1 Absorption spectroscopy of gas molecules

2.1.1 Parameters of optical absorption

The absorption cross-section, often denoted by the Greek letter sigma (σ), is a key parameter in describing how a single molecule of a gas absorbs light. It provides a measure of the probability that a photon will be absorbed by the molecule. The absorption cross-section is conceptually represented as the effective area "presented" by the molecule for the absorption of the photon. If we imagine the beam of light as a stream of photons, the cross-section is effectively the 'target size' of the molecule for these photons. The intensity of the beam, $I\ (x, y)$, is the power per unit area of the beam, and it will typically decrease as it propagates through a gas due to absorption and scattering. The total amount of light absorbed by a collection of molecules then depends on both this cross-section and the number density of the molecules [1].

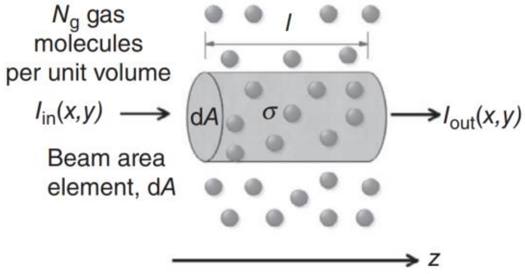

Figure 2.1 Description of the parameters used in the Beer–Lambert law.[1]

Given a cross-sectional area, as shown in Fig. 2.1, denoted as $dA = dxdy$, the likelihood of a molecule capturing or absorbing a photon is represented as σ / dA. As the beam travels a small distance, dz, along its propagation path, it encounters gas molecules. Consequently, the rate of photon absorption, also interpretable as the alteration in beam intensity, is governed by this interaction:

$$dI(x,y) = -I(x,y)(\frac{\sigma}{dA})(N_g dAdz) = -I(x,y)\sigma N_g dz \tag{2.1}$$

N_g signifies the number density, defined as quantity per unit volume. It's presumed that this density remains consistent across the transverse plane (x,y) and along the direction of the beam's propagation, z. Therefore, the integration of Equation (2.1) gives the Beer-Lambert law of the transmitted power, P_{out}, after a path length, L:

$$P_{out} = P_{in} e^{-\sigma N_g L} \tag{2.2}$$

where P_{in} is the incident light power.

As depicted in Fig. 2.1, the absorption cross-section, denoted as σ, is contingent on the optical frequency (ν), gas pressure (*p*), and temperature (*T*). It can be expressed as $\sigma(v,\ p,\ T) = S(T)\phi(v,\ p,\ T)$. Here, $\phi(v,\ p,\ T)$ characterizes the line shape function in Fig. 2.2, while *S* represents the line strength per molecule, defined as follows:

$$S(T) = \int_{-\infty}^{\infty} \sigma(v,p,T)dv \tag{2.3}$$

Please note, with the definitions provided above, $\phi(v,\ p,\ T)$ is normalized such that $\int \phi(v,\ p,\ T)\ dv = 1$ over all frequencies. The number density, N_g, in equation (2.2), can be formulated by applying the ideal gas law and Dalton's law. We can therefore write for the number density:

$$N_g = N_A(\frac{n_g}{V}) = \frac{pX_g}{k_B T} = \frac{p_g}{k_B T} \tag{2.4}$$

Here, N_A represents Avogadro's number, while $k_B = R / N_A$ is identified as the Boltzmann constant and *R* is the ideal gas constant. The total gas pressure is denoted as

p, n_g signifies the number of moles, p_g stands for the partial pressure, and $X_g = n_g / n$ is the mole fraction of the target gas.

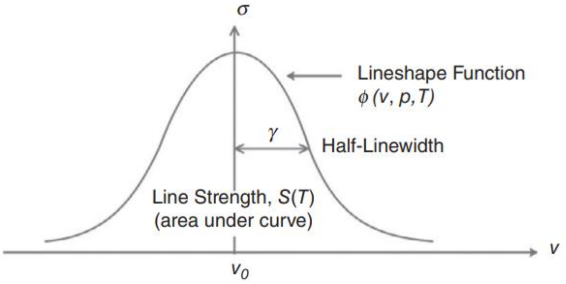

Figure 2.2 Typical absorption cross-section of a gas molecule and the associated parameters.[1]

Hence the Beer–Lambert law may be written as:

$$P_{out} = P_{in} exp[-S'(T)\phi(v, p, T) p X_g L] = P_{in} exp[-S'(T)\phi(v, p, T) p_g L] \tag{2.5}$$

Where $S'(T) = S(T) / (k_B T)$.

Another frequently utilized parameter is the absorption coefficient, represented as α. In this case, the absorption cross-section or line strength for a single molecule is multiplied by N_0, as shown in the following equation:

$$\alpha(v, p, T) = N_0 \sigma(v, p, T) = N_0 S(T) \phi(v, p, T) \tag{2.6}$$

$N_0 = p_0 / (k_B T_0) \cong 2.5 \times 10^{25} m^{-3}$ is the molecular density under Normal Temperature and Pressure (NTP), with $T_0 = 293.15\, K$ as the normal temperature, and $p_0 = 1\, atm$, equivalent to 101.325 kPa.

The Beer–Lambert law is then:

$$P_{out} = P_{in} exp[-\alpha C L] \tag{2.7}$$

where the target gas concentration at NPT is given by:

$$C = N_g / N_0 \tag{2.8}$$

2.1.2 Absorption Line shape Functions

The shape of absorption lines for gases is influenced by three mechanisms that broaden the lines. These mechanisms are natural broadening, Doppler broadening, and collisional (or pressure) broadening. [2, 3].

2.1.2.1 Natural Broadening

Photon absorption occurs when the energy level of an electron, atom, or molecule transition from a lower state to a higher state. However, due to the inherent uncertainty principle, there is a natural uncertainty associated with these energy states. As a result, absorption takes place over a small range of optical frequencies. [4].

This phenomenon bears resemblance to the exponential decay observed in spontaneous emission of light from transitions involving lower energy levels, commonly represented by a Lorentzian function in the frequency domain. Similarly, the line shape resulting from natural broadening in absorption processes is also represented by a normalized Lorentzian function. This function exhibits a characteristic natural half width at half maximum (HWHM) linewidth, γ_n .

Natural broadening specifies the spectral line sharpness limit. Yet, it won't be extensively examined here, as the linewidth in most practical scenarios is mostly influenced by Doppler or pressure-broadening effects, which will be discussed later.

2.1.2.2 Doppler Broadening

Doppler Broadening refers to the broadening of spectral lines due to the Doppler effect, which arises from the relative motion between the observer and the source of the waves. In the context of gas molecules absorbing light, it pertains to the change in observed frequencies due to the random thermal motions of the gas molecules.

Molecules moving towards the light source see the incoming light as slightly blue-shifted (towards higher frequencies), while molecules moving away see the light as slightly red-shifted (towards lower frequencies). This results in a broadening of the absorption line, as molecules absorb photons across a wider range of frequencies. This broadening is temperature-dependent, as the speed of the gas molecules is determined by the temperature of the gas.

Doppler Broadening is generally dominant at low pressures, where the molecules have fewer collisions and thus their thermal velocities are more relevant. At higher pressures, pressure broadening, or collisional broadening may become more significant.

The line shape function for Doppler broadening in the context of light absorption by a gas is typically given by a Gaussian distribution. This is because the velocities of the gas molecules follow a Maxwell-Boltzmann distribution, which is Gaussian.

For a gas at temperature *T* and molecules of mass *M*, the Doppler broadened lineshape function, $g(\nu)$, at optical frequency *v* around a center frequency ν_0, is given by[1]:

$$g(\nu) = \left(1/\sqrt{\pi}\gamma_D\right)\ exp\left[-(\nu - \nu_0)^2\ /\ \gamma_D{}^2\right] \tag{2.9}$$

where γ_D is the Doppler *1/e* half-linewidth, given by:

$$\gamma_D = \nu_0 \sqrt{(2k_B T)\ /\ M} \tag{2.10}$$

where k_B is the Boltzmann constant and *M* is the molecular weight in atomic mass units.

This Doppler lineshape function is Gaussian, centered around the line center frequency ν_0. The Doppler width is larger for lighter molecules and at higher temperatures, reflecting the higher speeds and therefore larger Doppler shifts under these conditions.

2.1.2.3 Collisional Broadening

Collisional broadening[1], also known as pressure broadening, occurs when the gas molecules frequently collide with each other. These collisions disturb the energy levels of the molecules, which in turn broadens the range of frequencies at which they can absorb light.

The more often the molecules collide, the shorter the lifetime of their energy states, and due to the uncertainty principle, the greater the uncertainty in their energy. This results in a broader range of frequencies for light absorption. Pressure broadening is more significant at higher pressures, where the gas molecules are more likely to collide with each other. The lineshape function for pressure broadening is typically given by a Lorentzian distribution:

$$l(\nu) = (\gamma_l / \pi) \ / \ \left[(\nu - \nu_0)^2 + (\gamma_l)^2\right] \qquad (2.11)$$

where:

- v is the frequency of the light,

- ν_0 is the center frequency of the absorption line,

- γ_l is the Lorentzian HWHM linewidth.

The parameter γ_l corresponds to the rate of collisions. The more frequently the molecules collide, the shorter the lifetime of their excited states, and the greater the energy uncertainty. This is why γ_l is larger at higher pressures where collisions are more frequent.

Mathematically, the parameter γ_l is often represented as:

$$\gamma_l = \gamma_0 \ (p / p_0) \ (T_0 / T)^n \qquad (2.12)$$

where:

γ_0 is the HWHM linewidth at NPT, p is the actual pressure of the gas, T is the actual temperature of the gas, n is a factor that usually ranges from 0.5 to 1 (0.5 for hard collisions and 1 for soft collisions).

In this formula, the pressure broadening is directly proportional to the pressure. This formula demonstrates how pressure and temperature can influence the line broadening in a gas.

Both self-broadening and cross-broadening are types of collisional or pressure broadening. They refer to the perturbations to the energy levels of molecules due to collisions, which result in a broadening of the spectral lines. The distinction between the two comes from the types of molecules involved in the collisions[5]:

Self-broadening: This occurs when a molecule collides with another molecule of the same type. For example, in a sample of pure nitrogen, the nitrogen molecules will collide with each other, leading to self-broadening of the nitrogen absorption or emission lines.

Cross-broadening: This occurs when a molecule collides with a molecule of a different type. For example, in air (which is a mixture of many types of molecules), a nitrogen molecule might collide with an oxygen molecule, leading to cross-broadening.

In many applications, it's important to consider both self-broadening and cross-broadening, especially when dealing with mixtures of gases. The overall broadening is often a weighted average of the self- and cross-broadening, with the weights determined by mole fractions involved.

The combination of Doppler broadening (which has a Gaussian lineshape) and collisional broadening (which has a Lorentzian lineshape) is often modeled by a Voigt profile[1]. In many situations, this provides a good approximation for the overall lineshape function.

This convolution function is also normalized and may be written as:

$$\phi_V(v - v_0) = \frac{1}{\gamma_D\sqrt{\pi}} V(b,a) \tag{2.13}$$

where *V(b, a)* is the Voigt function[6] defined by the integral:

$$V(b,a) = \frac{a}{\pi}\int_{-\infty}^{\infty} \frac{e^{-u^2}}{a^2 + (b-u)^2}\, du \tag{2.14}$$

Where $b = (v - v_0)/\gamma_D, a = \gamma_l/\gamma_D$.

2.1.3 Absorption lines of gases

Absorption lines, which are visible in spectroscopy, are primarily the result of the excitation of molecules' rotational and vibrational states, as well as electron transitions between atomic orbitals. These energy states are quantized, leading to distinct energy levels and absorption lines[1, 7].

For a simple comparison, the energy differences related to rotational levels typically correspond to the microwave region of the electromagnetic spectrum. Vibrational transitions, on the other hand, generally correspond to the MIR region. Electronic transitions, involving changes in an electron's energy level within an atom, usually correspond to regions with wavelengths less than 1 μm.

It's important to note that both rotational and vibrational transitions contribute significantly to the NIR absorption spectrum.

Interestingly, diatomic molecules made up of two identical atoms, such as oxygen (O_2) or hydrogen (H_2), do not exhibit changes in their electric dipole moment during rotational or vibrational movements. Consequently, they do not possess rotational or vibrational spectra. The spectral characteristics of interest for these types of molecules are predominantly the result of electronic transitions.

2.1.3.1 Rotational and Vibrational Lines of Gases

The excitation of a molecule into rotational states can occur through the interaction of the molecule's electric dipole moment with the oscillating electric field of radiation. The presence of a pure rotational line spectrum depends on whether the molecule possesses a permanent dipole moment. Linear symmetric molecules like CO_2 and highly symmetric spherical molecules such as CH_4 lack a permanent electric dipole moment, and therefore, they do not exhibit a pure rotational line spectrum in the microwave region. However, their rotational line spectra can be observed in conjunction with vibrational states.

To understand molecular rotation, it is useful to consider three principal axes of rotation that pass through the molecule's center of gravity. The rotational energy states and resulting line spectrum are primarily influenced by the moment of inertia associated with each axis, which is determined by the molecule's shape and symmetry. For example, diatomic gases like CO and linear molecules like CO_2 possess only one series of rotational absorption lines since the moment of inertia for rotation around the bond axis is close to zero. Similarly, highly symmetric spherical molecules like CH_4, which have approximately the same moment of inertia for all three principal axes, also exhibit a single series of rotational lines, at least as a first approximation. In contrast, molecules with more intricate structures, like H_2O, SO_2, and NO_2, often have three distinct moments of inertia. As a result, these molecules exhibit three fundamental series of rotational line spectra, each corresponding to rotation about a different axis. Additionally, combination series can arise from the simultaneous rotation about multiple axes in these molecules.

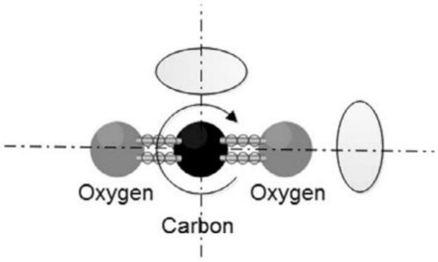

Figure 2.3 The three axes of rotation.[1]

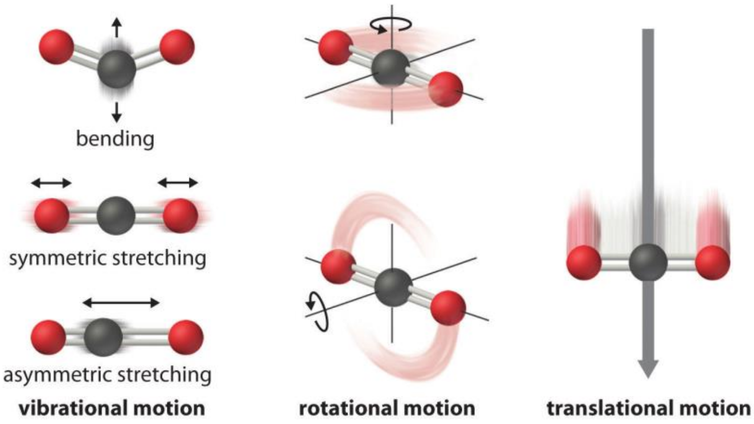

Figure 2.4 Molecular Motions. Vibrational, rotational, and translational motions of a carbon dioxide molecule are illustrated here.[8]

When considering the vibrational motion of molecules (as shown in Fig. 2.3 and 2.4), a simplistic model treats the bond between the atoms within the molecule as a spring, following Hooke's law. In this model, molecular vibrations resemble a mass-spring system, behaving as a simple harmonic oscillator. According to quantum mechanics, the energy states of this oscillator are quantized.

However, the actual behavior of molecular bonds deviates from the idealized Hooke's law model. Vibrations are better described as an anharmonic oscillator, where the energy states are still quantized but with non-uniform spacing. The transitions between energy states follow the selection rule, $\Delta V = \pm 1, \pm 2, \pm 3$, and so on. However, large energy jumps between states are less probable, and at normal temperatures, the populations of higher vibrational states are small. Consequently, the primary vibrational transitions of interest are the fundamental, first overtone, and second overtone, as illustrated in Fig. 2.5.

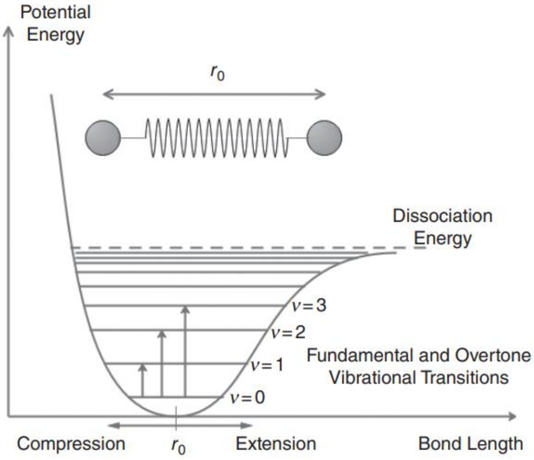

Figure 2.5 The energy levels of the anharmonic oscillator.[1]

In general, a molecule consisting of N atoms has 3N - 6 vibrational modes of motion (3N - 5 for linear molecules). These modes include N - 1 bond-stretching vibrations, while the remaining modes involve bending motions. It is important to note that for a vibration mode to interact with the exciting radiation, it must induce a change in the molecule's dipole moment.

In addition to the fundamental vibrational modes, molecules can also be excited into a blend of vibrational modes. These mixed states lead to vibrational energy levels corresponding to what are known as combination and difference bands.

It's noteworthy that vibrational modes which are typically inactive in the infrared may become apparent in combination with other modes. This interplay of vibrational modes and their combinations offers a rich and complex landscape for absorption phenomena, which is a fundamental aspect of spectroscopy.

2.1.3.2 Rovibrational Lines

In a general context, molecules can undergo combined vibration and rotation, resulting in rovibrational energy states. This phenomenon is observed in molecules like carbon dioxide (CO_2), methane (CH_4), and others, which do not possess a permanent dipole moment and therefore do not exhibit purely rotational spectra. However, during vibration, these molecules undergo variations in their dipole moments.

As previously mentioned, the energy difference between vibrational states in gas molecules typically falls within the mid-infrared range, while rotational states have much smaller energy gaps, typically in the microwave range. Due to this significant disparity, a rough approximation considers the total energy of a combined rovibrational state as the sum of the separate rotational and vibrational energies.

Each vibrational absorption line is accompanied by a series of closely spaced rotational lines. In the case of linear molecules where the vibration mode induces dipole changes parallel to the main axis of rotational symmetry (e.g., the antisymmetric stretching mode of CO_2), transitions between vibrational states require a change in the rotational state, denoted as $\Delta J = \pm 1$. However, for vibration modes that trigger perpendicular dipole changes (e.g., the bending mode of Nitrous oxide, N_2O), transitions with $\Delta J = 0, \pm 1$ are permitted.

For vibration modes of non-linear molecules, the selection rules become more intricate, but often $\Delta J = 0, \pm 1$ transitions are still allowed (e.g., for the asymmetric stretching mode of CH_4). The rovibrational lines corresponding to $\Delta J = 1, 0, +1$ are known as the P, Q, R branches, respectively, as illustrated in Fig. 2.6.

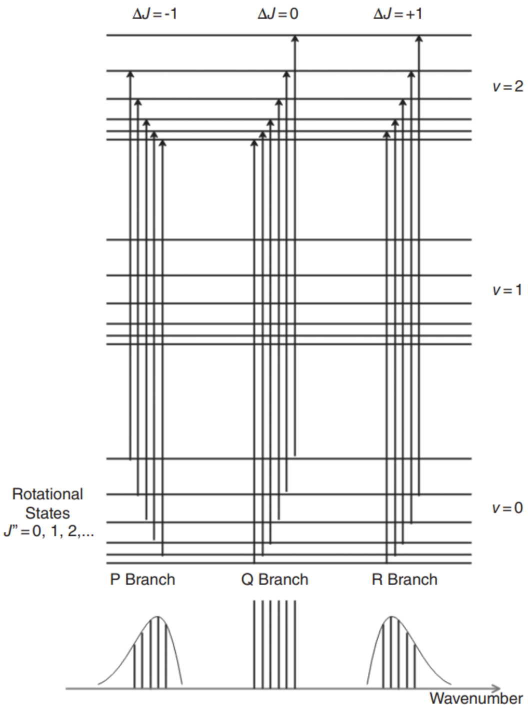

Figure 2.6 Characteristics of typical rovibrational absorption lines in the near-IR showing the P, Q and R branches[1].

2.1.3.3 Calculation of absorption coefficient

Having gained an understanding of the various parameters associated with absorption, including concepts such as absorption cross-section, absorption line strength, and line shape functions among others, we are now prepared to delve into the calculation of the absorption coefficient for a gas given specific conditions of temperature and pressure.

In real-world applications, the absorption coefficients are commonly sourced from the HITRAN database. The data output from this resource typically includes the following parameters that are instrumental for calculating the desired absorption coefficient: the position or wavenumber of absorption, the line strength(S), the air-broadened HWHM linewidth γ_{air}, and the self-broadened HWHM linewidth γ_{self}. In the context of the weak absorption approximation, where the gas concentration is exceedingly low and buffered by N_2 or air, the HWHM of the Lorentzian profile can be approximated to be equivalent to the air-broadening parameter, γ_{air}.

Take the R16 line in the *2υ1+υ3* band of CO_2 as an example. The wavenumber is $4989.971\ cm^{-1}$. $S_0 = 1.319\times10^{-21} cm^{-1}/(molecule\cdot cm^{-2})$ and $\gamma_l = \gamma_{air} = 0.074 cm^{-1}$. N_{tot} is the total molecular number density at NPT and is equal to 2.479×10^{19}[molecules/cm^3]. For a relative concentration of 100 ppm, the absorption coefficient at 1 atm and 293.15 K is:

$$
\begin{aligned}
a(v_0) &= C\ N_{tot}\ S\ l(v_0) \\
&= 100\times10^{-6}\times2.479\times10^{19}[\text{molecules/cm}^3] \\
&\quad \times1.319\times10^{-21}[cm^{-1}/(molecule\cdot cm^{-2})] \\
&\quad \times1/(\pi\times0.074[cm^{-1}]) \\
&= 1.406\times10^{-5}[cm^{-1}]
\end{aligned}
\tag{2.15}
$$

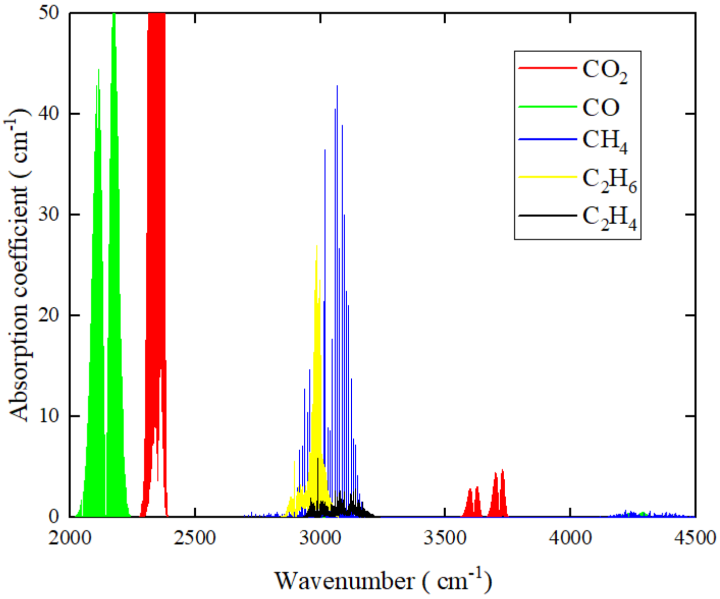

Figure 2.7 Calculated absorption coefficients for different gases.

As shown in Fig. 2.7, we have calculated the absorption coefficient for CO_2, CO, CH_4, C_2H_6 and C_2H_4 in the wavenumber range from 2000 cm^{-1} to 4500 cm^{-1} based on the Hitran database.

2.2 Direct absorption spectroscopy and laser modulation techniques

2.2.1 Direct absorption spectroscopy

Direct absorption spectroscopy (DAS) is a robust method employed for exploring the interaction between light and matter, typically used in identifying and measuring the number of specific substances in a sample.

In the DAS technique, a optical source is directed at the sample. The light interacts with the sample, being absorbed uniquely depending on the molecular composition of the substance under investigation. This resultant absorption spectrum is then scrutinized and measured.[9]

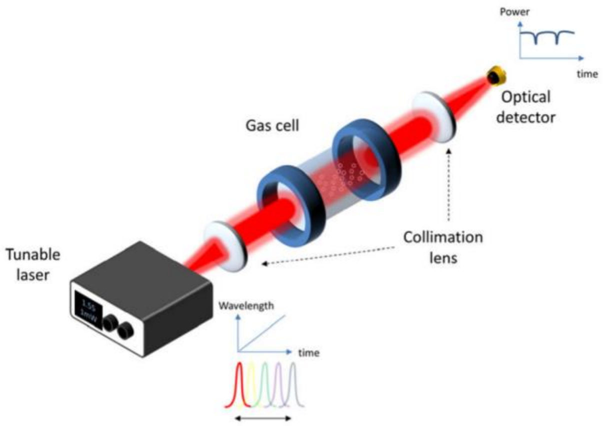

Figure 2.8 3D view of direct absorption spectroscopy using a tunable laser diode [10]

In the realm of gas analysis, DAS can be employed to identify and measure different gases in a sample by evaluating their unique absorption spectra. It's particularly effective in detecting trace gases, capable of identifying minute changes in the absorption spectra, signifying low concentrations of certain gases.

This absorption measurement is usually computed by comparing the optical powers of a reference light and a sensing light. A This setup serves to neutralize any effects caused by power fluctuations in the laser, frequently called intensity noise.

Depending on the requirements, external cavity diode lasers (ECDL), may be employed for DAS. In circumstances requiring smaller linewidths and/or broader tuning ranges, more sophisticated laser sources might be needed.

To ensure a lengthy light propagation path in the gas. Hence, different multi-pass gas cells (like White, or Herriott types[11]) have been designed. These cells permit a laser beam to pass through multiple times, allowing for longer propagation lengths even within compact optical setups.

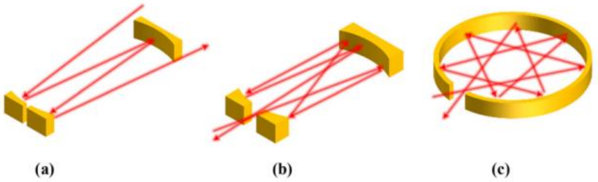

Figure 2.9 (a) White Cell (b) Herriot cell (c) Circular multipass cell [10]

2.2.2 Laser modulation techniques

Laser intensity noise is the fluctuations of output power over time. In the context of DAS, this intensity noise can affect the precision and accuracy of the measurements.

To understand why this is an issue, it's important to note that DAS operates by measuring the difference in optical power between a reference and sensing light. Therefore, any changes in the laser's output power — even those not related to the absorption of the sample — will cause a variation in the measured absorption.

In essence, DAS is trying to detect a small change (the absorption by the sample) in a relatively large signal (the overall laser power). If the laser's output power is varying due to intensity noise, it can be challenging to discern the small changes caused by the sample's absorption from the large fluctuations caused by the laser's intensity noise.

Modulation techniques, including wavelength, intensity, or frequency modulation, are often combined with DAS to enhance its performance. This combination can mitigate some of the inherent limitations of DAS, particularly its sensitivity to laser intensity noise and low signal-to-noise ratio (SNR) in certain conditions [12].

2.2.2.1 Intensity modulation technique

In certain applications, DAS is combined with intensity modulation (IM), a technique that involves varying the intensity at a specific frequency. This can help improve overall performance and reliability of DAS measurements.

The basic principle of intensity modulation in DAS is as follows: the intensity of is varied periodically over time at a chosen frequency. This modulation frequency is typically much higher than the frequencies of intensity noise and other low-frequency noise sources in the system.

The absorption signal from the sample is then measured synchronously with the modulation, i.e., the PD signal is sampled at the same specific frequency. This technique is commonly referred to as lock-in detection or synchronous detection.

The principle of DAS with intensity modulation can be expressed mathematically using the Beer-Lambert Law, which is the fundamental equation for absorption spectroscopy.

The Beer-Lambert Law is given as:

$$I = I_0 e^{(-\alpha LC)} \tag{2.16}$$

where:

- I is the transmitted light intensity

- I_0 is the incident light intensity

- α is the absorption coefficient

- L is the path length

- C is the concentration of the gas

In DAS with intensity modulation, the incident light intensity (I_0) is modulated as a function of time (t) at a frequency (v_m). Thus, I_0 can be written as:

$$I_0 = I_{DC} + I_m \, cos\left(2\pi v_m t\right) \tag{2.17}$$

where:

- I_m is the amplitude of modulation and I_{DC} is the DC component.

The transmitted light intensity (I) also varies with time due to the modulation of the incident light, so the Beer-Lambert Law becomes:

$$I(t) = I_m\ e^{(-\alpha LC)} cos(2\pi v_m t) + I_{DC}\ e^{(-\alpha LC)} \tag{2.18}$$

The detector output (D) is then synchronously demodulated at the modulation frequency, so the detected signal is:

$$D(t)\ =\ A_m\ \ cos\left(2\pi v_m t\ +\ \varphi\right) + A_{DC} \tag{2.19}$$

where:

- $A_m = \eta_{PD} I_m\ e^{(-\alpha LC)}; A_{DC} = \eta_{PD} I_{DC}\ e^{(-\alpha LC)}$ and A is the amplitude of the detected signal, which is related to the detected light intensity I and the PD coefficient η_{PD}.

- φ is the phase shift between the detected signal and the modulated light intensity

If we demodulate the signal at frequency v_m and consider the optical frequency (v) dependence. The output signal of lock-in amplifier (LIA) is:

$$X\left(v\right)\ =\ LPF\left\{D\left(v,\ t\right)\ \ cos\left(2\pi v_m t\right)\right\}\ =\ A_m\left(v\right)\ \ cos\left(\varphi\right) \tag{2.20}$$

LPF stands for the low-pass filter function, which removes the high-frequency component of the signal. In the case of weak absorption, where the product of the absorption coefficient $\alpha(v)$ and the path length L is much less than 1 (i.e., $\alpha LC << 1$), the exponential term in the Beer-Lambert law can be approximated using a first order Taylor series expansion $I = I_0(1-\alpha LC)$. And at specific T, L and C, the demodulated signal of IM $A_m(v) = \eta_{PD} I_m (1-\alpha(v)LC)$ is linearly proportional to the absorption $\alpha(v)$.

2.2.2.2 Wavelength modulation spectroscopy

Wavelength modulation spectroscopy (WMS) [12] is a variation of DAS that can provide enhanced SNR and improved sensitivity for the sensing of gases.

In WMS, instead of keeping the laser wavelength constant or sweeping it linearly across an absorption line as in DAS, the wavelength of the laser is modulated at a high frequency (typically in the kHz to MHz) around the absorption line of interest. This modulation is typically sinusoidal and is superimposed on a slower linear scan across the absorption line.

This technique results in a modulation of the transmitted intensity of the light, which can be detected and demodulated to yield an absorption signal. The advantage of WMS is that by demodulating at multiple harmonics of the modulation frequency, it is possible to extract an absorption signal that is largely free from low-frequency noise (such as 1/f noise) that can impact DAS measurements.

When modulating the optical frequency of the light in WMS, the absorption coefficient α also becomes a time-varying function due to the modulation of the optical frequency. Thus, we can write the absorption coefficient as a function of time:

$$\alpha(t) = \alpha\left[v(t)\right] = \alpha\left[v_i + \delta v \, \mathrm{e}^{j\omega t}\right] \tag{2.21}$$

Here, $\alpha(t)$ represents the time-varying absorption coefficient and $\alpha[v(t)]$ is the absorption coefficient as a function of optical frequency $v(t)$. δv is the modulation amplitude of WMS. $m = \delta v / \gamma$ is the modulation depth of optical frequency and γ is the HWHM linewidth of the absorption line. v_i is the mean optical frequency of the modulated light over a modulation period and $\omega = 2\pi v_m$ is the angular frequency of modulation. The use of $e^{j\omega t}$ in this context is primarily to simplify the calculations, but it's important to note that the real part of this complex number carries significant meaning.

If the absorption line shape function is represented by a Lorentzian function, which is often a good approximation for pressure-broadened absorption lines, the lineshape function is given in Equation (2.11).

When the optical frequency is modulated sinusoidally, the time-varying absorption coefficient $\alpha(t)$ becomes a function of the normalized Lorentzian line shape and show as:

$$\alpha(v) = \alpha_0 \frac{1}{1+[(v-v_0)/\gamma_l]^2} \tag{2.22}$$

where α_0 is the absorption coefficient at the center of an absorption line v_0. Expending it into harmonic series [13], we have

$$a(v_i) = a_0 \operatorname{Re}\{H_o + \sum_{n=1}^{\infty} H_n e^{-jn\omega t}\} \tag{2.23}$$

with

$$H_0(v_i) = \frac{1}{\pi}\int_0^{\pi} \frac{1}{1+[(v_i - v_0)/\gamma_l + m cos(\vartheta)]^2}\, d\vartheta \tag{2.24}$$

$$H_n(v_i) = \frac{2}{\pi}\int_o^{\pi} \frac{cos(n\vartheta)}{1+[(v_i - v_0)/\gamma_l + m cos(\vartheta)]^2}\, d\vartheta \ (n \geqslant 1) \tag{2.25}$$

The harmonic coefficients H_0 and H_n play an integral role in characterizing the harmonic waveforms. We leverage complex notation, as depicted in Equation (2.23), throughout the subsequent chapters for its utility in representing these waveforms. It is, however, important to note that the physical implications are captured solely by the real components. Henceforth, for the sake of brevity and lucidity, we will not explicitly mention the 'Re' function.

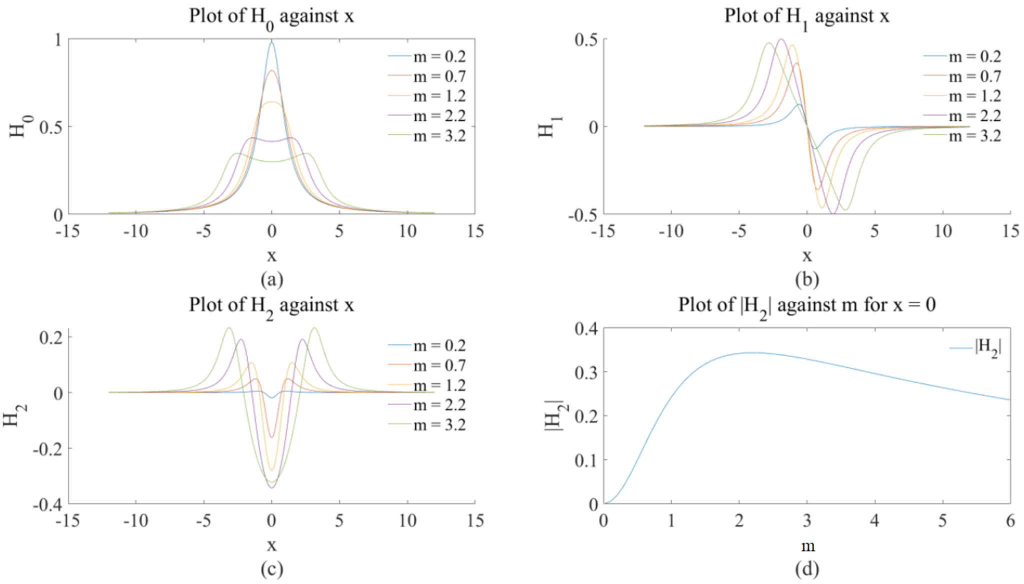

Figure 2.10 Plot of the Hormonic coefficients for different modulation depth *m*. $x = (v_i - v_0)/\gamma_l$ means the detuning from the absorption line center.

Fig. 2.10 provides a visual representation of calculated harmonic coefficients across various modulation depths, m. Notice that the even-ordered harmonic coefficients peak at the center of the absorption line. The second harmonic coefficient reaches its maximum at the line center with a modulation depth of $m \approx 2.2$, and then gradually diminishes as the modulation depth is further increased, as shown in Fig. 2.10(d).

2.2.2.3 Frequency modulation spectroscopy

Frequency modulation spectroscopy (FMS) is a powerful technique widely employed for trace gas detection. This advanced method leverages the principle of modulating the phase of light from a laser [14]. In FMS, it is important to avoid simplifying the properties of light to a characterization solely based on defined power or intensity. Rather, it must be conceptualized as comprising an electrical field vector, the phase of which undergoes sinusoidal modulation at a frequency symbolized by ν_m. The spectrum of the electromagnetic field can be expressed using a series of Bessel functions, $J_k(\beta)$ [15].

$$E(t) = E_0 e^{i[2\pi\nu_c t+\beta\sin(2\pi\nu_m t)]} = E_0 e^{i2\pi\nu_c t}\sum_{k=-\infty}^{\infty} J_k(\beta)e^{i2\pi k\nu_m t} \tag{2.26}$$

Considering scenarios where the modulation index of phase, β, are small ($i.e.$, $\beta \ll 1$), the light can be split into three components: a carrier centered at frequency ν_c, and two sidebands positioned at $\nu_c \pm \nu_m$. Here, the modulation depth of optical frequency is defined by $m_f = \nu_m / \gamma$. As this spectral triplet navigates through an absorption profile, the transmitted electrical field is modified to the following formula, where $T(\nu)$ symbolizes a complex transmission function for the electrical field. This function denotes the influence of the analyte and can be represented via an amplitude attenuation, $\delta(\nu)$, which in turn leads to an absorption signal, as well as an optical phase shift, $\phi(\nu)$, which results in a dispersion signal.

$$\begin{aligned} E_T(\nu_c,t) = E_0 e^{i2\pi\nu_c t}[&J_0(\beta)T(\nu_c) - J_1(\beta)T(\nu_c-\nu_m)e^{-i2\pi\nu_m} \\ &+ J_1(\beta)T(\nu_c+\nu_m)e^{i2\pi\nu_m t}], \end{aligned} \tag{2.27}$$

$$T(\nu) = e^{-\delta(\nu) - i\phi(\nu)} \tag{2.28}$$

From the identification with Beer's law, it is feasible to articulate the amplitude attenuation using some of the mentioned variables. $\delta(\nu)$ and $\phi(\nu)$ can be represented in the following Equations 2.29 and 2.30, where $\overline{x}^{disp}(\nu)$ stands for the dispersion line-shape function. This function is interconnected with the peak-normalized absorption profile, $\overline{x}^{abs}(\nu)$, via the Kramers-Kronig relations.

$$\delta(\nu) = \frac{\alpha_0}{2}\overline{x}^{abs}(\nu)CL \tag{2.29}$$

$$\phi(\nu) = \frac{\alpha_0}{2}\overline{x}^{disp}(\nu)CL \tag{2.30}$$

For conditions of weak absorption (i.e., $\alpha_0 CL << 1$) and small β, the time-dependent light intensity of the transmitted electrical field can be expressed as follows:

$$\begin{aligned} I(\nu_c, t) &= c\varepsilon_o <|E_T(\nu_c, t)|^2>= I_0\{1 + 2J_0(\beta)J_1(\beta) \\ &\times\left[\delta(\nu_c - \nu_m) - \delta(\nu_c + \nu_m)\right]cos(2\pi\nu_m t) + 2J_0(\beta)J_1(\beta) \\ &\times\left[\phi(\nu_c - \nu_m) - 2\phi(\nu_c) + \phi(\nu_c + \nu_m)\right]sin(2\pi\nu_m t)\} \\ &= I_o(1 + J_o(\beta)J_1(\beta)\alpha_0 LC\{[\overline{x}^{abs}(\nu_c - \nu_m) \\ &- \overline{x}^{abs}(\nu_c + \nu_m)]cos(2\pi\nu_m t) + [\overline{x}^{disp}(\nu_c - \nu_m) \\ &- 2\overline{x}^{disp}(\nu_c) + \overline{x}^{disp}(\nu_c + \nu_m)]sin(2\pi\nu_m t)\}) \end{aligned} \tag{2.31}$$

In the above context, c is the light speed in the vacuum and ε_0 is the vacuum permittivity. The term $\langle\ \rangle$ represents a time average of the rapid components (of the order of ν_c), whereas I_0 signifies the intensity of light in a scenario devoid of gases.

Following demodulation at frequency ν_m with an FM detection phase denoted by θ_{fm}, the FM signal S^{fm} can be formulated as follows. In equation 2.32, η_{fm} is a factor related to the instrumentation that includes the detector's responsivity and the gain inherent in the FM detection system. P_0 is the optical power and calculated by $P_0 = \int I_0 dA$, where A is the area of laser beam.

$$S^{fm}\left(v_c, v_m, \theta_{fm}\right) = \eta_{fm} J_0(\beta) J_1(\beta) P_o a_0 L \times \left\{ \begin{array}{l} \left[\overline{x}^{abs}\left(v_c - v_m\right) - \overline{x}^{abs}\left(v_c + v_m\right)\right] \cos\,\theta_{fm} \\ + \left[\overline{x}^{disp}\left(v_c - v_m\right) - 2\overline{x}^{disp}\left(v_c\right) + \overline{x}^{disp}\left(v_c + v_m\right)\right] \sin\,\theta_{fm} \end{array} \right\} C \tag{2.32}$$

By the relations[16]:

$$\overline{x}^{abs}(\nu) = \left(\frac{1}{R^2(\nu)+1}\right) \qquad \overline{x}^{disp}(\nu) = \left(\frac{R(\nu)}{R^2(\nu)+1}\right)$$
$$R(\nu) = \frac{\nu - \nu_0}{\gamma_l} \tag{2.33}$$

By combining Equations 2.32 and 2.33, we can derive the FMS signal for various modulation frequencies if we set other parameters (η_{fm}, P_o, a_0, L and C) to a unit value.

Fig. 2.11 provides a calculated output for a scenario where β is set at 0.2, and the θ_{fm} is zero. This set of conditions corresponds to the generation of an absorption signal. In this case, the output demonstrates how the absorption of the gas sample varies with modulation depth (m), thereby showing the unique absorption characteristics of the specific gas being analyzed.

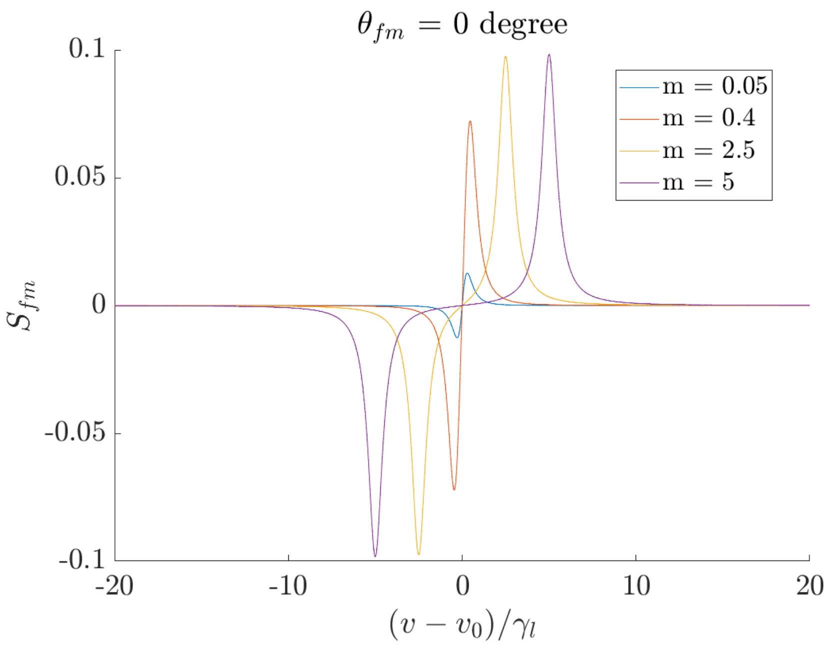

Figure 2.11 Absorption signal for different *m*.

On the other hand, Fig. 2.12 illustrates the dispersion signal that arises when β is set to 0.2 and the θ_{fm} is set to 90 degrees. In this instance, the signal represents the variation in the light's phase as it interacts with the gas sample. This dispersion signal can provide additional valuable information about the gas sample.

Together, these two figures present a comprehensive picture of the capabilities of FMS for trace gas detection, demonstrating how this technique can yield both absorption and dispersion signals under different operating conditions. The utilization of both types of signals can improve the overall accuracy and reliability of trace gas detection using FMS.

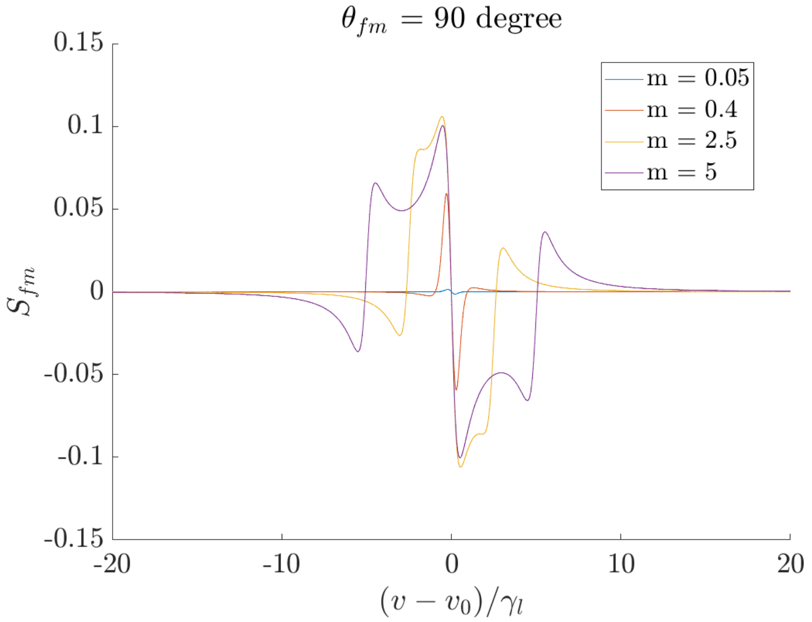

Figure 2.12 Dispersion signal for different m.

2.3 Photothermal spectroscopy

Photothermal spectroscopy (PTS) is a collection of sensitive techniques utilized for the analysis of a sample's optical absorption and thermal properties, based on photothermal effects—changes in a sample's thermal state due to light-induced heating. Classified as an indirect method of assessing optical absorption, PTS focuses on the impact that optical absorption, rather than light transmission, has on a sample. Yet, in some ways, it can be seen as more direct, as it measures a direct consequence of optical absorption, namely the heating of the sample. PTS provides accurate measurements of optical absorption in scattering solutions, solids, and at interfaces, lending itself to a variety of studies.[17]

2.3.1 Basic processes in PTS

Fig. 2.13 depicts the fundamental mechanisms involved in generating a photothermal spectroscopy (PTS) signal. The process begins with the excitation of a sample using optical radiation, typically emitted from a laser. The sample absorbs a portion of this radiation, leading to an increase in its internal energy. This excess energy is then dissipated through hydrodynamic relaxation, causing a temperature change within the sample or its surrounding material. Consequently, the density of the sample undergoes a corresponding variation.

If the photothermal-induced temperature fluctuation occurs rapidly compared to the expansion or contraction time of the sample, a pressure change can ensue. This pressure disturbance propagates as an acoustic wave. Once the pressure returns to equilibrium, a density change proportional to the temperature change persists.

In all cases, the absorption of optical energy induces a temperature change within the sample, which, in turn, causes a density change. These combined alterations in temperature and density affect various properties of the sample. PTS is centered around measuring these modified characteristics. Notably, the most sensitive photothermal methods rely on detecting changes in refractive index associated with changes in the sample's temperature and density.

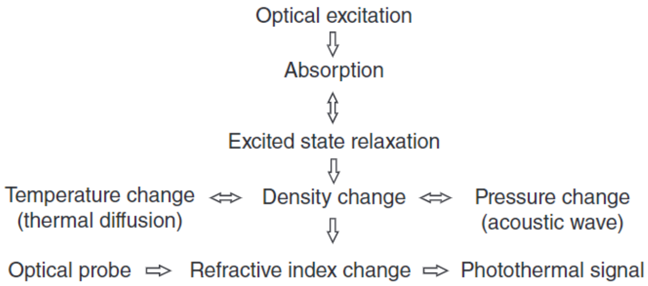

Figure 2.13 Photothermal spectroscopy involves a series of processes [18]

2.3.2 Vibrational relaxation time

When an absorber absorbs light, it transitions to an excited state, elevating its internal energy to match that of the absorbed photon. This excited state typically undergoes relaxation, resulting in sample heating corresponding to the absorbed photon energy. However, this relaxation process is not instantaneous and may generate heat at slow rates that do not contribute to observable photothermal signals, due to rapid hydrodynamic relaxation and thermal diffusion.

The relaxation of the excited state involves various mechanisms operating at different rates. The timescales can range from femtoseconds to seconds, depending on factors such as the nature of the excited state, intermediate energy levels, and the composition of the sample matrix.

The relaxation sequence of a vibrationally excited species can be anticipated by considering the progression of vibrational (V), rotational (R), and translational (T) relaxations. Figure 2.14 illustrates the relaxation process for such species. Laser sources can be employed to selectively excite specific rovibrational states, promoting them to higher vibrational levels and forming a single rovibrational excited state. This can create a gap in the canonical rotational state distribution of the ground state.

Following excitation, relaxation processes such as rotation to rotation (R-R), rotation to translation (R-T), and translation to translation (T-T) occur immediately. R-R relaxation of the excited state allows dispersion of the rovibrational states into a canonical distribution. The ground state undergoes rotational hole filling while rotational state dissipation takes place in the excited state. The collective R-R relaxations of the ground and excited states can either extract energy from the sample matrix or contribute energy to it.

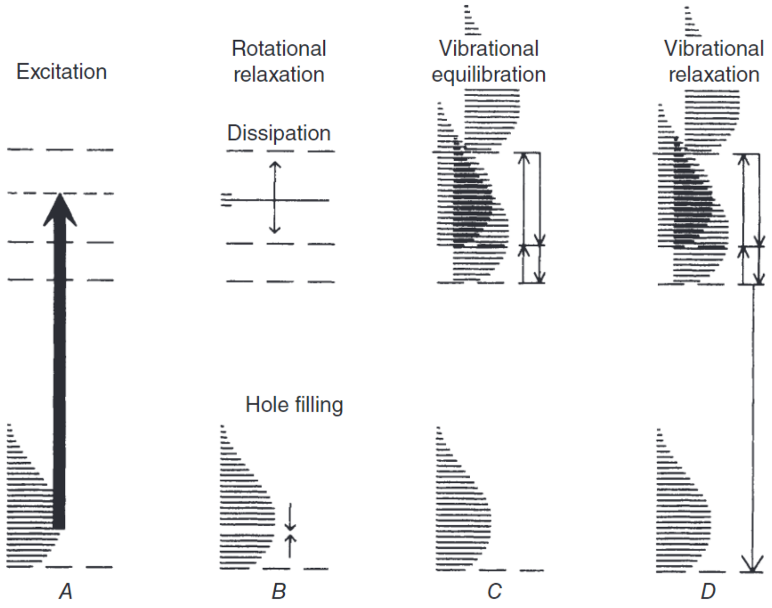

Figure 2.14 Energy-level diagram illustrating the relaxation processes for rovibrational excitation [17]

Following the faster relaxation stages of R-R/T and T-T, the vibration to vibration (V-V) relaxation takes place, establishing a quasi-equilibrium among the excited vibrational levels. The energy initially confined to a single rovibrational excited state becomes distributed among other rotational and excited vibrational states of the molecule. Since these states are typically not in resonance with the excitation source, further excitation becomes less likely. The populations of the excited vibrational levels may reach a canonical distribution before undergoing bottleneck relaxation to the ground state. Finally, these excited vibrational states decay to the ground state, primarily through the fastest vibration to rotation/translation (V-R/T) rate.

In general, each vibrationally excited state decays to the ground state at a rate approximately proportional to the exponential energy gap of the excited state. During the slower V-R/T step, the faster V-V relaxation steps maintain the populations of excited states in a canonical distribution. As a result, it is challenging to differentiate the V-R/T relaxation steps for individual levels. Instead, the excited vibrational levels decay at a constant rate determined by the sum of the individual rates multiplied by the canonical population of the level.

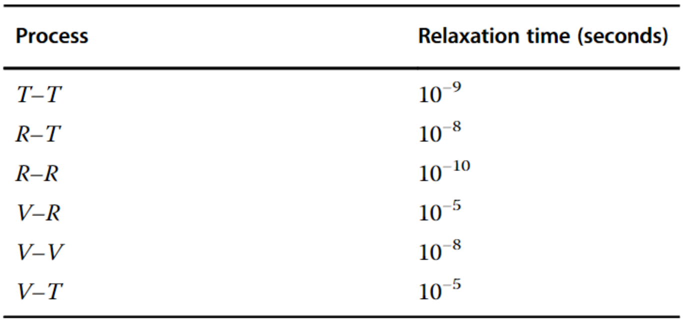

Process	**Relaxation time (seconds)**
T–T	10^{-9}
R–T	10^{-8}
R–R	10^{-10}
V–R	10^{-5}
V–V	10^{-8}
V–T	10^{-5}

Figure 2.15 Relaxation times for typical gas phase species at standard temperature and pressure [17]

It's important to highlight that the relaxation time of the V-R/T process can significantly differ among various gases or distinct gas mixtures. When considering gases at room temperature (296 K), the product of gas pressure (p) and vibrational relaxation time (VRT) (τ_V) can be treated as a constant.

The V-R/T process is instrumental in determining the rate of heat generation through non-radiative relaxation. Consequently, the VRT holds notable relevance for PTS. Although the relaxation of excited rovibrational states encompasses a complex process, it is a suitable approximation to view it as a two-level system with a time constant of τ_V. The efficiency (η_H) of heat generation corresponding to a specific angular frequency ω can be approximated as:

$$\begin{gathered} p\tau_v = const \\ \eta_H = \frac{1}{\sqrt{1+(\omega\tau_V)^2}} \end{gathered} \tag{2.34}$$

2.3.3 Photothermal induced phase modulation in a gas filled HCF

In an HCF, both light and gas samples are confined simultaneously within the core, creating an excellent platform for robust interactions between light and gas over long distances. In this section, we will explore the photothermal effects that occur within HCFs, encompassing heat generation, heat conduction, and the mechanisms behind optical phase modulation induced by changes in gas density.

To simplify our analysis, we make several approximations:

(a) We assume that gas absorption is minimal, allowing us to consider the pump power as constant along the propagation path.

(b) The dominant process for dissipating heat is thermal conduction.

(c) The HCF predominantly supports the propagation of the fundamental mode, which exhibits a Gaussian intensity profile with radial symmetry.

By employing these approximations, we can effectively examine the photothermal phenomena within HCFs while minimizing redundant information.[19]

First, we consider the heat source caused by absorption. The volume heat source is given by:

$$Q(r,t) = \eta_H \cdot \alpha \cdot C \cdot P_{pump} / (\pi w_{pump}^2) \cdot exp(-r^2 / w_{pump}^2) \cdot S(t) \tag{2.35}$$

where α is the absorption coefficient, C is the gas concentration. P_{pump} is the power and w_{pump} is the mode field radius of the pump beam in HCF. $S(t)$ is the time-varying function of modulation.

In such scenarios, the temperature increase can be determined by solving the equations governing heat transfer [19]:

$$\rho C_p \frac{\partial T}{\partial t} = \nabla \cdot (\kappa \nabla T) + Q(r,t) \tag{2.36}$$

Where κ is the gas thermal conductivity. ρ is the gas density. C_p is the specific heat capacity.

The HCF model we utilize comprises a silica outer cladding with an inner diameter of approximately 56 μm. Inside the HCF, there are seven capillary rings with diameters of roughly 14 μm and a thickness of about 370 nm. Consequently, an inscribed air core with a diameter of approximately 28 μm is formed.

With the COMSOL Multiphysics software, numerical simulation of temperature change ($\Delta T(r,t)=T(r,t)-T_{abs}$) is conducted. The core is filled with nitrogen-balanced 100 ppm acetylene. The P is equal to 1 bar, and the room temperature T_{abs} is 293.15 K. The α is 1.16 cm^{-1}, corresponding P(13) absorption line of acetylene at 1532.83 nm. The VRT of acetylene is 77 ns.

Fig 2.16 shows the temperature distribution in an HCF, and the Fig 2.17 shows the frequency response of the temperature change at the center of the air core. As discussed in ref. [20], at higher frequencies of pump modulation, the temperature change experiences a decrease primarily because of two factors. Firstly, the thermal relaxation time of gas molecules comes into play, reducing the efficiency of heating. Secondly, the slow thermal conduction within the gas further contributes to the limitation in temperature modulation. The sluggish thermal conduction prevents the temperature from adequately tracking the rapidly changing heat source, leading to a reduced temperature response. With in simulation, thermal conduction is the main limitation due to the short VRT of 77 ns.

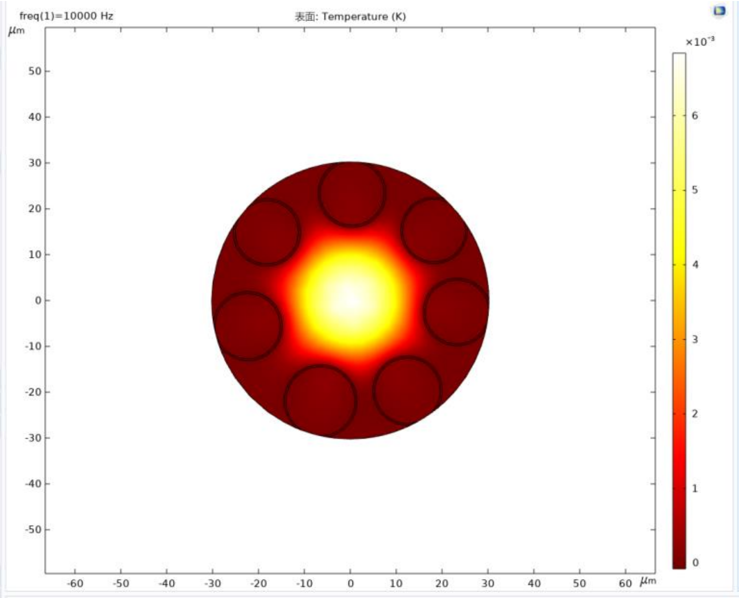

Figure 2.16 The temperature distribution in HCF and the modulation frequency is 10 kHz.

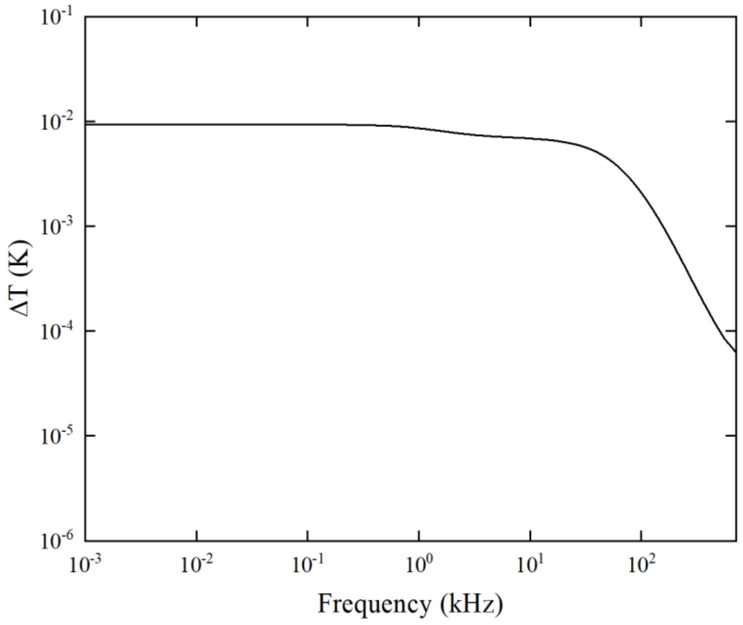

Figure 2.17 Frequency response of the temperature change at the center of HCF.

After the temperature change is determined, the temperature induced RI change in gas molecules may be obtained as [19]:

$$\begin{aligned}\Delta n &= -(n_0 - 1)\frac{\Delta T(r,t)}{T_{abs}} \\ &= \frac{\partial n}{\partial T}\Delta T(r,t)\end{aligned} \tag{2.37}$$

Where $\partial n/\partial T = -(n_0 - 1)/T_{abs}$ is the thermos-optic coefficient. If a probe light travel through the HCF, the PT induced phase change of the probe light may be expressed as:

$$\Delta\phi(t) = \frac{2\pi L}{\lambda_{probe}} \cdot \frac{\partial n}{\partial T}\int \Delta T(r,t)\frac{2exp(-2r^2 / w_{probe}^2)}{\pi w_{probe}^2} \cdot 2\pi r dr \tag{2.38}$$

Equation 2.38 can be used for numerically evaluate the phase change of the probe light, which can be simply expressed as [21]:

$$\Delta\phi = k^*\alpha(v_{pump})P_{pump}CL \tag{2.39}$$

Where k^* is the phase modulation coefficient, which is related to the structure of HCF, nature of gas sample and the modulation frequency.

2.4 Raman spectroscopy

Raman scattering [22] is a form of inelastic scattering where the frequency of the scattered light is altered by a specific frequency. This frequency shift corresponds to the difference between the initial and final states of the molecule involved in the scattering event.

In a classical context, when a molecule becomes excited, it oscillates around its equilibrium position, leading to changes in its polarizability. These changes are associated with Raman active vibrational modes. Typically, the fundamental modes exhibit stronger Raman activity, but combinations or overtones of these modes can also exhibit Raman scattering, albeit with weaker intensity.

This thesis specifically focuses on rovibrational Raman scattering within the ground electronic state. As shown in Figure 2.18, the incident pump light undergoes a scattering process called Stokes scattering, where it is scattered to a lower frequency. This process results in the excitation of the gas molecule to a rovibrational state. Simultaneously, the pump light can also undergo scattering to a higher frequency, known as anti-Stokes scattering, causing the gas molecule to de-excite from a rovibrational state to a lower energy state.

Under certain conditions, Raman scattering can become stimulated, meaning that the frequency and phase of the scattered light align with those of the incident light. This occurs when the pump power is sufficiently high or when additional incident Stokes or anti-Stokes light is present.

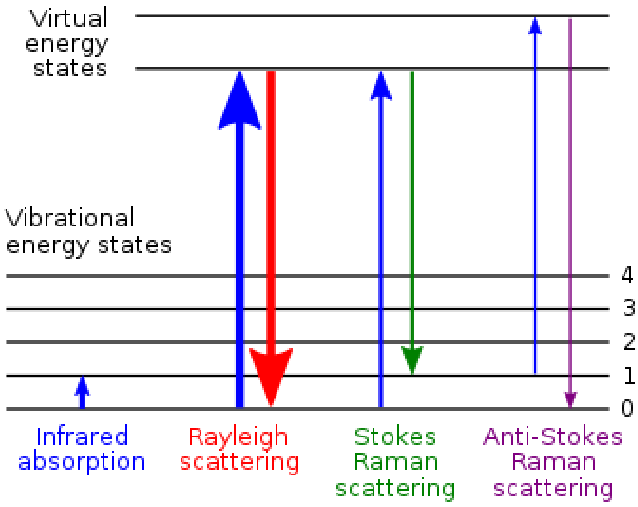

Figure 2.18 Energy-level diagram showing the states involved in Raman spectra [23]

For gas-phase media, the peak plane-wave steady-state Raman-gain coefficient g_R can be obtained from [22]:

$$g_R = \frac{2\lambda_s^2}{h\nu_s} \frac{\Delta N}{\pi \gamma_R} \frac{\partial \sigma}{\partial \Omega} \tag{2.40}$$

where h is the Planck constant, λ_s is the Stokes wavelength, ν_s is the optical frequency of the Stokes light. ΔN is the population difference between the two states given by $\Delta N = N(0,J) - (2J + 1/2J' + 1)N(V, J')$, and N is the number density in an individual vibrational-rotational state. γ_R is the full width at half-maximum Raman linewidth in hertz, and $\partial\sigma/\partial\Omega$ is the differential scattering cross section for the specific polarizations used in the experiment. The wavelength dependence of the Raman gain results from scattering cross section, whereas the temperature and density dependence results from changes in the Raman linewidth. The Raman scattering cross-section depends on the scattering angle (θ) and the polarizations of the Stokes and pump light. In the context of Raman scattering in HCFs, we focus on two scattering angles: 0 and π, which correspond to forward and backward Raman scattering, respectively. Table 2.1 provides a summary of the Stokes Raman cross-sections for the S-branch and Q-branch of diatomic molecules.[24]

Table 2.1 Polarization dependent Raman cross-section $\partial\sigma/\partial\Omega$

Branch	ΔV	ΔJ	$\partial\sigma/\partial\Omega(0;\|)$	$\partial\sigma/\partial\Omega(0;\perp)$
$S_0(J)$	0	+2	$\frac{4}{45}b_{J+2,J}\gamma_{00}^2$	$\frac{1}{15}b_{J+2,J}\gamma_{00}^2$
$S_1(J)$	+1	+2	$\frac{4}{45}b_{J+2,J}\gamma_{10}^2$	$\frac{1}{15}b_{J+2,J}\gamma_{10}^2$
$Q_1(J)$	+1	0	$a_{10}^2+\frac{4}{45}b_{J,J}\gamma_{10}^2$	$\frac{1}{15}b_{J,J}\gamma_{10}^2$

The factor $(2\pi v_s / c_0)^4$ in each cross-section has been omitted in the table; $\|$ and $\perp$ refer to that the polarization of pump light is parallel or perpendicular to the Stokes light;

The Placzek-Teller b factor are $b_{J,J}=\frac{J(J+1)}{(2J-1)(2J+3)}$ *and* $b_{J+2,J}=\frac{3(J+1)(J+2)}{2(2J+1)(2J+3)}$; a_{FI} and γ_{FI} are isotropic polarizability and the anisotropic polarizability for the initial state *I* and final state *F*. ΔV is the change in vibrational state and ΔJ is the change in rotational state.

We take hydrogen as an example. The polarizability $\gamma_{00}, \gamma_{10}, a_{10}$ are weakly dependent on the pump wavelength and are approximated to be $3.0 \times 10^{-25} cm^3$, $0.87 \times 10^{-25} cm^3$ *and* $1.0 \times 10^{-25} cm^3$ for pump wavelength in the near IR (the relative change of polarizability is less than 4% for wavelengths from 800 nm to 2000 nm) [25]

The linewidth of Raman scattering in hydrogen molecules is influenced by pressure. When the pressure is low, the linewidth is primarily determined by Doppler broadening. As the pressure increases, the combined effects of Dicke narrowing [26] and collisional broadening lead to a minimum linewidth before it starts to expand again. However, for the sake of simplicity, the linewidth is commonly represented using an empirical formula. This change in linewidth is a crucial factor to consider when analyzing Raman spectra under different pressure conditions. The formula is [22]:

$$\gamma_R = \frac{A}{\rho} + B\rho \tag{2.41}$$

where ρ is the density in amagat and the coefficients A and B are given in Table 2.2

Table 2.2 Coefficients A and B at room temperature (298 K) for hydrogen

Transition	A (MHz amagat)	B(MHz/amagat)
$S_0(0)$	1.87	77
$S_0(1)$	6.15	114
$Q_1(0)$	257	76.6
$Q_1(1)$	309	52.2

We calculated the linewidth for different hydrogen Raman transition at different pressure using the Equation 2.41 and the Table 2.2 and results are shown in Fig. 2.19.

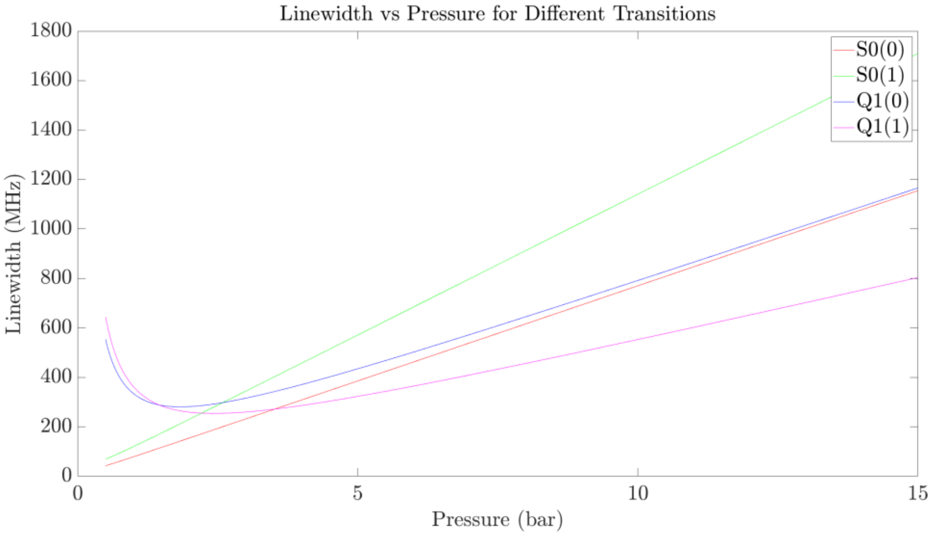

Figure 2.19 Simulated linewidth for different hydrogen Raman transition at different pressure.

The population difference ΔN between the initial state and the final state is:

$$\Delta N = N(V_i R_i) - \frac{2J+1}{2J+5} N(V_f R_f) \tag{2.42}$$

For Raman transition $S_0(J)$, the initial state i is $V_i = 0, R_i = J$ and the final state f is $V_f = 0, R_f = J+2$. $N(VR)$ means the population density in VR, Considering the spin degeneracy of hydrogen, the population density can be given by the Boltzmann distribution:

$$N(VR) = \frac{(2J+1) g_{nuc} e^{-\frac{E(VR)}{k_B T}}}{\sum_J (2J+1) e^{-\frac{E(VR)}{k_B T}}} N_{tot} \tag{2.43}$$

$E(VR)$ represents the energy of the energy level VR, while $N_{tot} = p / k_B T$ is the total molecular number density where p is pressure, k_B is the Boltzmann constant, and T is temperature. g_{nuc} represents the nuclear spin degeneracy. At room temperature, g_{nuc} is typically taken as 3 for ortho-H_2 (hydrogen molecules in odd J rotational energy levels) or 1 for para-H_2 (hydrogen molecules in even J rotational energy levels).

For the pure rotational transitions $S_0(0)$ and $S_0(1)$, the changes in number density ΔN are approximately $0.11N_{tot}$ and $0.62N_{tot}$, respectively. However, for the vibrational transitions, considering that the energy of a vibrational transition vastly exceeds $k_B T$, the number density at the vibrational energy level $N(V_f R_f)$ can be neglected. Therefore, for the vibrational transitions $Q_1(0)$ and $Q_1(1)$, ΔN is roughly $0.13N_{tot}$ and $0.658N_{tot}$, respectively.

With these data, we can calculate the Raman gain coefficient at different pressure for different hydrogen Raman transition when wavelength of the Stokes light is 1550 nm and the results are shown in Fig. 2.20. The $Q_1(1)$ transition of hydrogen shows the largest Raman gain coefficient, which is about 5 times of that of $S_0(1)$ and is about 10 times of $S_0(0)$ for pressures higher than 10 bar.

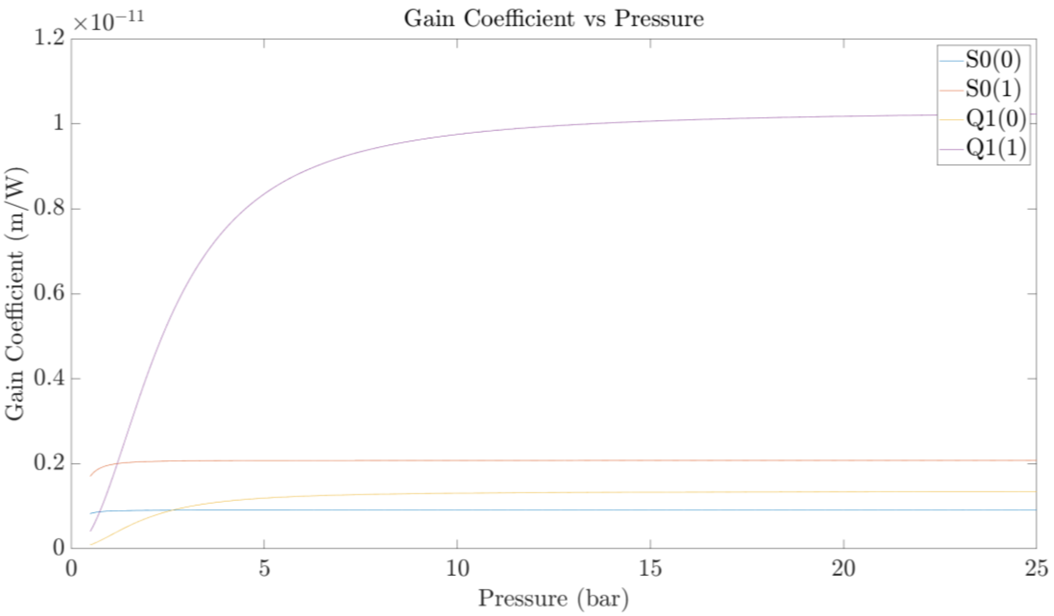

Figure 2.20 Simulated gain coefficient for different hydrogen Raman transition at different pressure.

Fig. 2.21 shows the calculated Raman gain coefficients for *$Q_1(1)$* transition when the polarization of pump is parallel/perpendicular to the Stokes and the stokes wavelength is 1550 nm. For vibrational Raman transitions, the Raman gain coefficient reaches the maximum with parallel linear polarizations of pump and Stokes. Below 10 bar, the difference increases with the increase of pressure, and above 10 bar, the difference is basically unchanged.

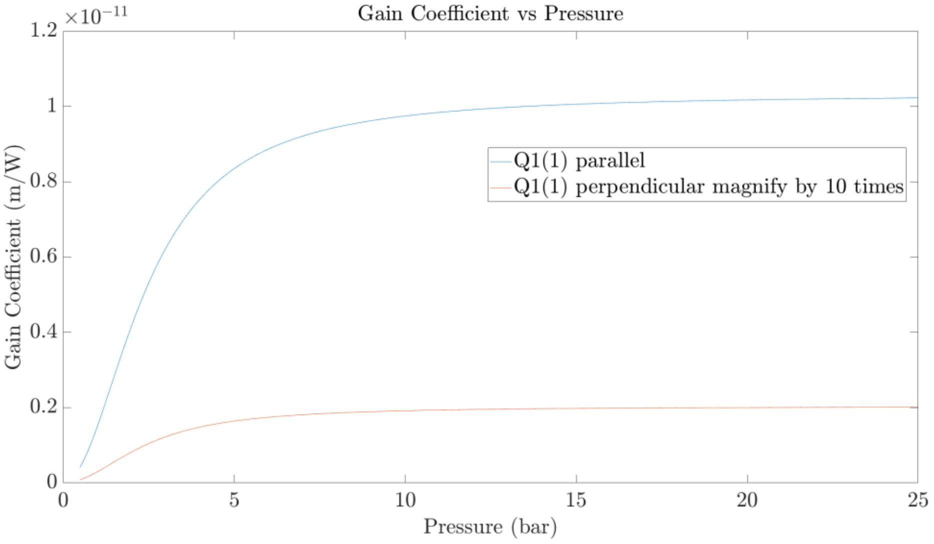

Figure 2.21 Simulated gain coefficient as a function of pressure when the polarization of pump is parallel/perpendicular to the Stokes.

2.5 Reference

1. G. Stewart, *Laser and Fiber Optic Gas Absorption Spectroscopy* (Cambridge University Press, 2021).
2. W. Demtröder, *Laser spectroscopy* (Springer, 2008).
3. A. M. Fox, *Quantum optics: an introduction* (Oxford University Press, USA, 2006).
4. B. H. Stuart, *Infrared spectroscopy: fundamentals and applications* (John Wiley & Sons, 2004).
5. D. Williams, "4.1. Infrared Region," in *Methods in Experimental Physics*, D. Williams, ed. (Academic Press, 1976), pp. 1-49.
6. W. Voigt, "Über das Gesetz der Intensitätsverteilung innerhalb der Linien eines Gasspektrums," (1912).
7. C. N. Banwell, and E. M. McCash, *Fundamentals of molecular spectroscopy* (Indian Edition, 2017).
8. "Evaluating Entropy and Entropy Changes," https://chem.libretexts.org/Bookshelves/General_Chemistry/Map%3A_General_Chemistry_%28Petrucci_et_al.%29/19%3A_Spontaneous_Change%3A_Entropy_and_Gibbs_Energy/19.3%3A_Evaluating_Entropy_and_Entropy_Changes.
9. Z. Du, S. Zhang, J. Li, N. Gao, and K. Tong, "Mid-infrared tunable laser-based broadband fingerprint absorption spectroscopy for trace gas sensing: a review," Applied sciences **9**, 338 (2019).
10. A. Fathy, Y. M. Sabry, I. W. Hunter, D. Khalil, and T. Bourouina, "Direct absorption and photoacoustic spectroscopy for gas sensing and analysis: A critical review," Laser & Photonics Reviews **16**, 2100556 (2022).
11. Y. Liu, and Y. Ma, "Advances in multipass cell for absorption spectroscopy-based trace gas sensing technology," Chinese Optics Letters **21**, 033001 (2023).
12. S. Schilt, L. Thevenaz, and P. Robert, "Wavelength modulation spectroscopy: combined frequency and intensity laser modulation," Appl. Opt. **42**, 6728-6738 (2003).
13. R. Arndt, "Analytical line shapes for Lorentzian signals broadened by modulation," Journal of Applied Physics **36**, 2522-2524 (1965).
14. G. Gagliardi, and H.-P. Loock, *Cavity-enhanced spectroscopy and sensing* (Springer, 2014).
15. A. Foltynowicz, F. M. Schmidt, W. Ma, and O. Axner, "Noise-immune cavity-enhanced optical heterodyne molecular spectroscopy: Current status and future potential," Applied Physics B **92**, 313 (2008).
16. G. C. Bjorklund, M. Levenson, W. Lenth, and C. Ortiz, "Frequency modulation (FM) spectroscopy: theory of lineshapes and signal-to-noise analysis," Applied Physics B **32**, 145-152 (1983).
17. S. E. Bialkowski, N. G. Astrath, and M. A. Proskurnin, *Photothermal spectroscopy methods* (John Wiley & Sons, 2019).
18. S. E. Bialkowski, *Photothermal spectroscopy methods for chemical analysis* (John Wiley & Sons, 1996).
19. Y. Lin, W. Jin, F. Yang, J. Ma, C. Wang, H. L. Ho, and Y. Liu, "Pulsed photothermal interferometry for spectroscopic gas detection with hollow-core optical fibre," Scientific reports **6**, 39410 (2016).
20. H. Bao, Y. Hong, W. Jin, H. L. Ho, C. Wang, S. Gao, Y. Wang, and P. Wang, "Modeling and performance evaluation of in-line Fabry-Perot photothermal gas sensors with hollow-core optical fibers," Optics express **28**, 5423-5435 (2020).
21. W. Jin, Y. Cao, F. Yang, and H. L. Ho, "Ultra-sensitive all-fibre photothermal spectroscopy with large dynamic range," Nature Communications (2015).

22. W. K. Bischel, and M. J. Dyer, "Wavelength dependence of the absolute Raman gain coefficient for the Q (1) transition in H 2," JOSA B **3**, 677-682 (1986).

23. W. contributors, "Raman spectroscopy," https://en.wikipedia.org/w/index.php?title=Raman_spectroscopy&oldid=1153819516.

24. D. A. Long, "Raman spectroscopy," New York **1** (1977).

25. L. Wolniewicz, "Polarizability of the hydrogen molecule," The Journal of Chemical Physics **46**, 1426-1432 (1967).

26. R. Dicke, "The effect of collisions upon the Doppler width of spectral lines," Physical Review **89**, 472 (1953).

Chapter 3

3 PTS with MIR pump and NIR probe using a HCF FPI

3.1 Introduction

In recent years, Researchers have demonstrated gas detection with PTS using HCF gas cells in the NIR [1-3], a method that is insensitive to mode mixing noise. In the NIR, mature telecom fiber-optic components provide many advantages, and various fiber-optic phase-detection configurations have been investigated for detecting photothermal phase modulation. This approach has enabled us to achieve detection lower to the ppb levels for molecules having strong NIR absorption [4].

However, gases like ethane lack strong NIR absorption. To detect ethane sensitively with PTI, a MIR pump is used to generate signal and the NIR probe interferometer could be used to detect the signal [5].

Here, we report a PTS ethane sensor with a MIR pump and a NIR all-fiber FPI to probe photothermal phase modulation with high sensitivity. Among all the previously reported MIR HCF gas sensors, this sensor exhibits excellent stability and the lowest NEA normalized by length.

3.2 Ethane absorption lines at 3.3 µm

Ethane, being a key constituent in natural gas, has notable importance in atmospheric chemistry, climate research, and oil and gas prospecting [6, 7]. Moreover, it's been found that exhaled ethane levels can indicate lipid peroxidation, showing potential for identifying conditions like schizophrenia or lung cancers [8, 9]. Given these applications, there's a need for detection on the ppb level or lower.

Fig. 3.1(a) shows the calculated absorption coefficients of ethane and water from 2970 to 3000 cm^{-1}. We choose to work at the strongest line at 2986.72 cm^{-1}, and the calculated absorption coefficient and spectral linewidth at 296 K and 1 atm are respectively 5.5×10^{-4} cm^{-1} and 0.144 cm^{-1} for 10 ppm ethane. Fig 3.1(b) shows the measured absorption spectrum of 1% ethane balanced with N_2, by using direct absorption and a

14-cm-long HCF gas cell (black squares) in the lab environment. Lorentzian curve fitting shows the absorption linewidth is about 0.151 cm^{-1}.

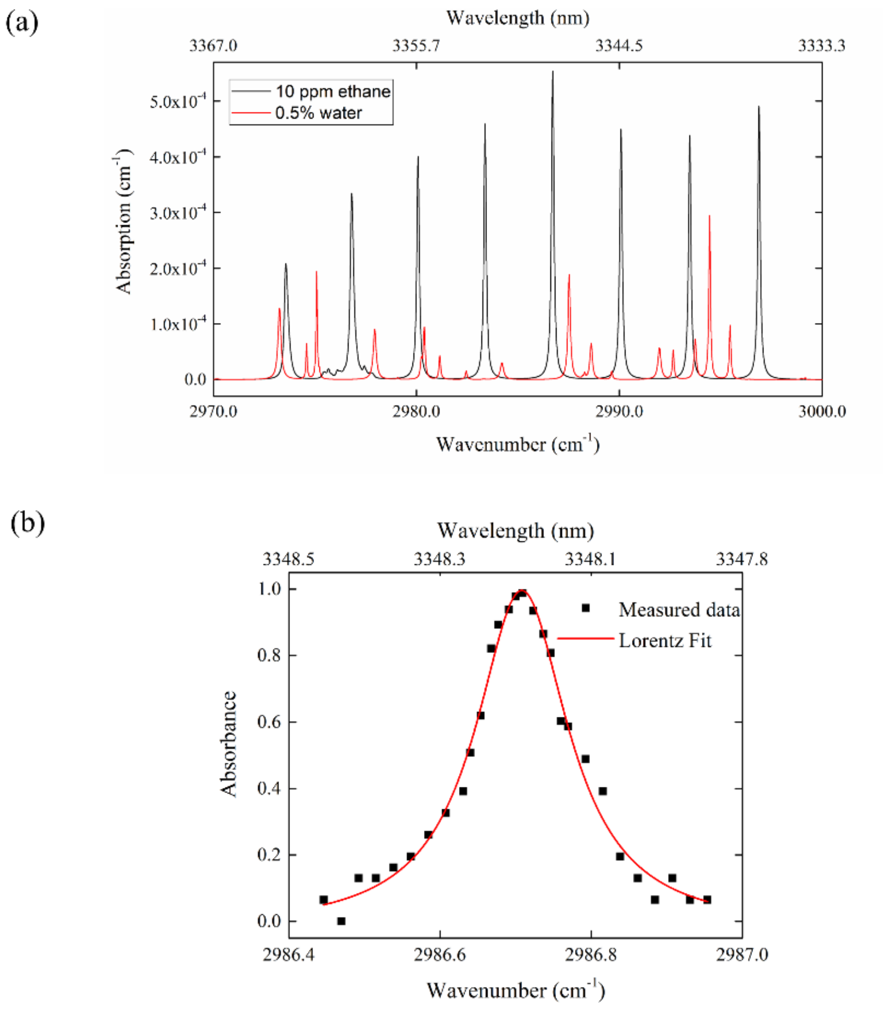

Figure 3.1. (a) HITRAN-based absorption spectrum of 10 ppm ethane and 0.5% water from 2970 cm^{-1} to 3000 cm^{-1}. (b) Measured absorption spectrum around 2986.7 cm^{-1}.

3.3 Design of gas cell

Fig. 3.2 shows the structure of the HCF gas chamber, which is built by mechanically splicing, using ceramic ferrules and sleeves, a 14-cm-long sensing AR-HCF (orange color) to two solid optical fibers (blue and red). Small gaps of ~ 10 micrometers are kept between the HCF and the solid fibers. The AR-HCF has a core of 65 μm in diameter [10, 11], and the Scanning Electron Microscope (SEM) cross-sectional image is in Figure 3.2(b). This HCF has multiple transmission bands, as measured in Figure 3.2(c) and the attenuations at 1.55 μm (pump) and 3.34 μm (probe) are ~ 0.4 dB/m and ~ 0.15 dB/m, respectively [11].

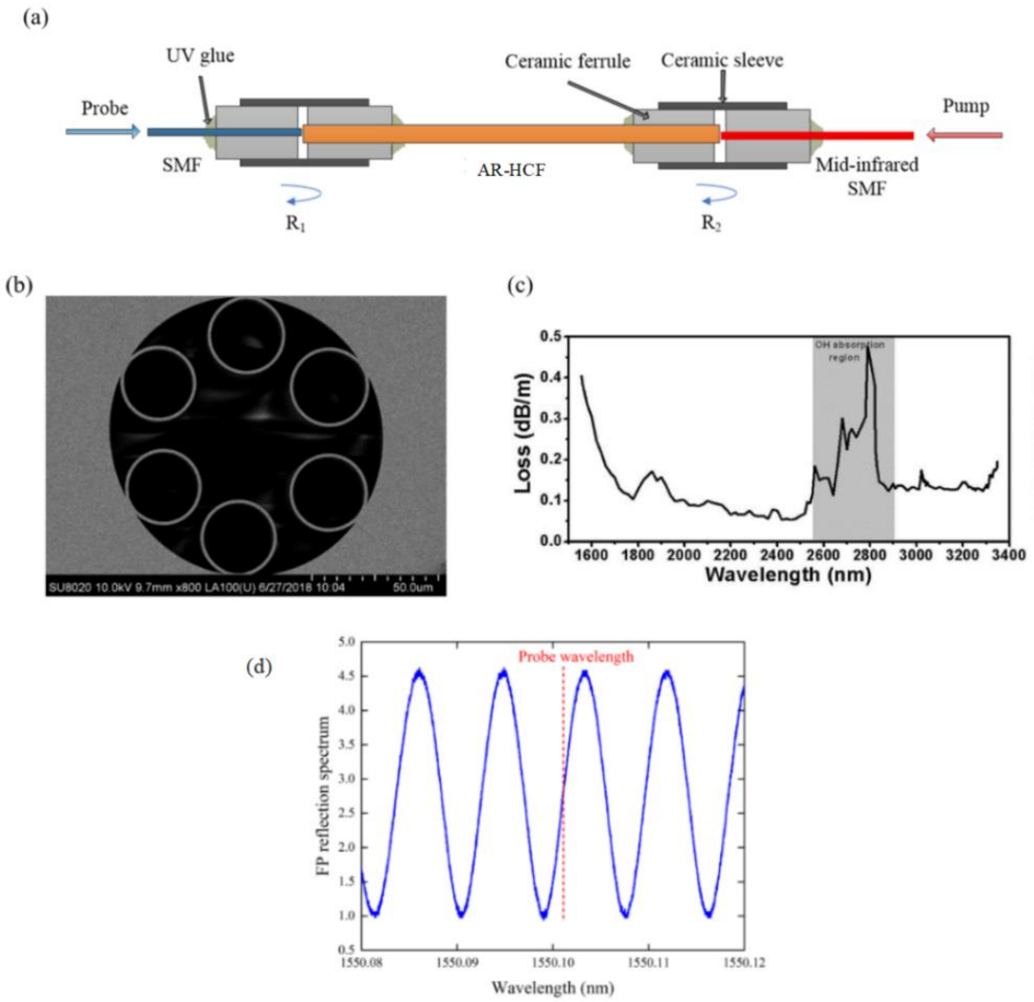

Figure 3.2. (a) Schematic of the AR-HCF gas chamber showing pump input from MIR fiber and probe input to and reflections from the FPI. (b) Cross-section of the AR-HCF. (c) Attenuation spectrum [11]. (d) The reflected spectrum.

The red fiber is an MIR InF_3-based SMF at the pump wavelength. It couples the pump beam into the HCF from one end to produce PT phase modulation.

The MFDs of the MIR SMF and AR-HCF at the pump wavelength are respectively 10.2 μm and 52 μm, and the joint loss for light transmission from the MIR fiber to the AR-HCF is about 3 dB.

The blue fiber is the standard SMF28 fiber and it delivers the probe beam into gas cell from another end of the AR-HCF and receives the reflected probe beams from the gas chamber. As can be seen in Fig. 3.2(a), the pump and probe beams are launched into the AR-HCF from opposite ends, which enables complete separation of the pump and probe optics, allowing the use of extremely simple MIR optics to deliver pump power into the HCF for the generation of PT phase modulation and cost-effective NIR components to form all-fiber probe interferometer circuity to detect the phase modulation with high sensitivity. The two natural reflections (~4%) at the SMF28/AR-HCF and AR-HCF/MIR-SMF joints form a low-finesse FPI for the probe beam. The reflected spectrum around 1550 nm was measured with a tunable narrow-linewidth laser in combination with an oscilloscope and is shown in Fig. 3.2(d). The FSR is 8.6 pm, agreeing very well with the calculated value by using $\delta\lambda=\lambda^2/2L$. The MFDs of the SMF28 and AR-HCF at the probe wavelength are respectively 10.4 μm and 49 μm. The measured joint loss is about 3 dB for light transmission from the SMF28 to the AR-HCF and 6 dB from the AR-HCF to SMF. The total coupling loss (η_C) for the probe beam reflected from the AR-HCF/MIR-SMF joint is about 9 dB. Considering the similar RIs of the SMF28 (1.47) and the MIR-SMF (1.50), we may regard the reflectivity at the two interfaces as approximately the same, i.e., $R_1 \approx R_2 = R(R << 1)$. Neglecting the transmission loss of the AR-HCF, the reflected light intensity from the FPI may be approximated by [3]

$$I_R \approx I_o R\left[1+{\eta_C}^2+2\eta_C\cdot\cos\varphi\right] \tag{3.1}$$

With

$$\varphi=\frac{4\pi n_{eff}L}{\lambda_{probe}}+\varphi_0 \tag{3.2}$$

where I_0 and I_R are respectively the incident and reflected light intensities, φ is the phase difference between the two reflected beams, n_{eff} is the effective RI for the probe, L is the cavity length of FPI, λ_{probe} is the probe wavelength, and φ_0 is a constant.

The fringe contrast [12] in the unit of dB may be expressed as

$$10\log_{10}\frac{I_{R,\max}+I_{R,\min}}{I_{R,\max}-I_{R,\min}}=10\log_{10}\frac{1+{\eta_C}^2+2\eta_C}{1+{\eta_C}^2-2\eta_C} \tag{3.3}$$

For η_C = 9 dB, the fringe contrast is calculated to be 6.4 dB, corresponding well with the measured value of ~ 6.5 dB, as shown in Fig. 3.2(d). There is room for further improvement by reducing the joint loss η_C .

For gas detection experiments, a narrow linewidth laser (see next section) is used as the probe source and the probe wavelength is locked to the quadrature point of the interference fringe, as indicated in Fig. 3.2(d), so that the PT phase modulation is efficiently and linearly converted into intensity modulation at the reflected FPI output. The temperature change will influence the stability of active loop.

3.4 Experimental set-up

The experimental set-up is shown in Fig. 3.3. A 3.4 μm ICL with emission power up to 6 mW is used as the pump source and the collimated beam is coupled into the MIR SMF through an FC/APC connector by using a lens. The coupling efficiency into the MIR fiber is ~ 50%, corresponding to a pump power level of ~ 1.5 mW coupled into the AR-HCF. A 2*f*-WMS detection technique is employed in the experiment to improve the SNR. The ICL is sinusoidally modulated at 7 kHz via a current controller. The wavelength modulation results in periodic absorption and heating of the gas sample, which modulates the phase of the probe beam. At the same time, the wavelength of the ICL is scanned via a temperature controller at 3 mHz.

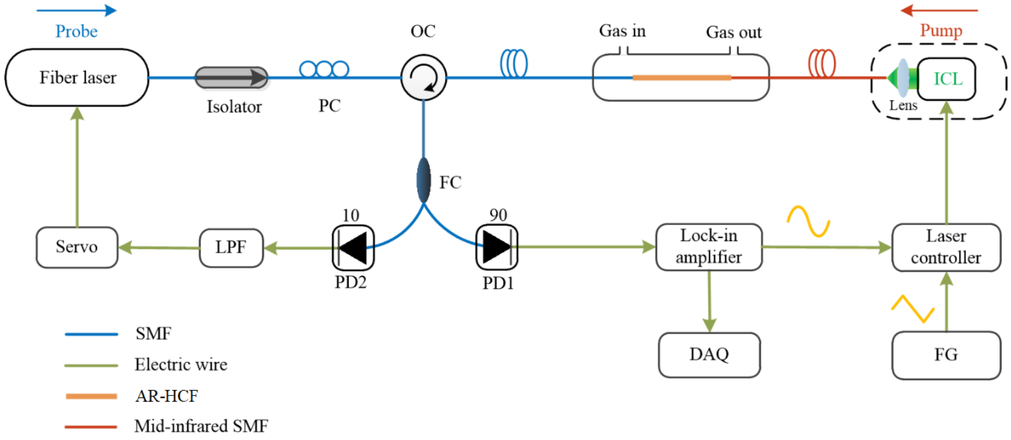

Figure 3.3. Experiment set-up for ethane detection with 14-cm-long AR-HCF. DAQ, data acquisition; FC, fiber coupler; FG, function generator; ICL, interband cascade laser; LPF, low-pass-filter; OC, optical circulator; PC, polarization controller; PD, photodetector.

We use a single frequency fiber laser as the probe source and a polarization controller to maximize the fringe contrast of FPI. The fiber laser is equipped with a piezoelectric wavelength tuning mechanism and the probe wavelength can be servo-controlled so that the FPI is always operating at quadrature. From Fig. 3.2(d), the quadrature point corresponds to a voltage of V_{offset}=2.7 V, and we use the difference between the DC output of PD2 and this reference voltage, i.e. $V_{error}=V_{DC}-V_{offset}$, as the error signal. The error signal is sent into the servo controller, which generates the control signal to change the probe wavelength. The stabilization mechanism by using DC output and servo-loop ensures high sensitivity and long-term stability of the system. Servo-control of the probe wavelength instead of the cavity length [13] of the FPI enables completely passive all-fiber gas cells without electric connections. The FPI output is demodulated by a lock-in amplifier at the second harmonic of the modulation frequency.

3.4.1 Test and result

3.4.1.1 Performance of the servo-loop

Fig. 3.4(a) shows the DC output detected by PD2 with and without servo-control. The output fluctuates considerably around the quadrature point without servo-control and reaches an approximately constant level immediately after the servo stabilization is applied. The performance of the FPI stabilization in terms of phase fluctuation from the quadrature point is calculated by comparing the output fluctuation with the interference fringe contrast in Fig. 3.2(d) and is shown in Fig. 3.4(b). The standard deviation (s.d.) of phase fluctuation is 0.054°, about an order of magnitude better than that of a stabilized MZI [2].

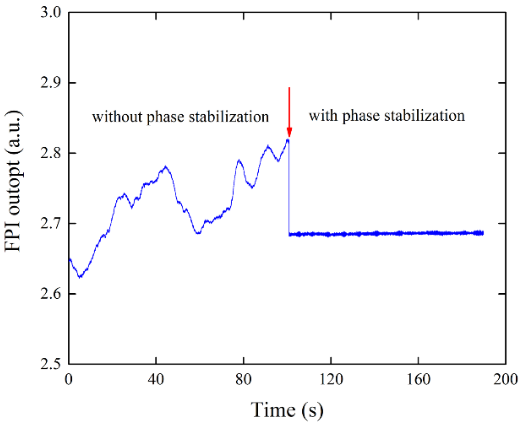

(a)

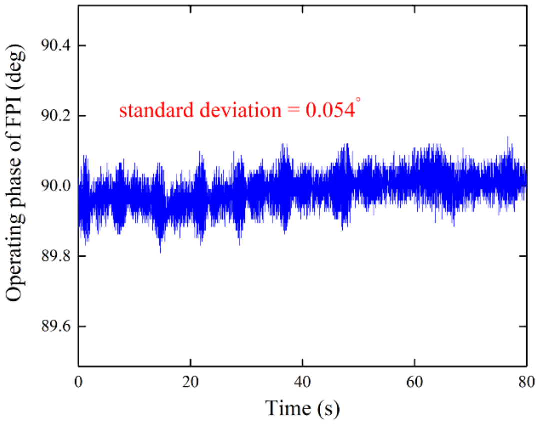

(b)

Figure 3.4. FPI phase stabilization. (a) DC output of the FPI with and without phase stabilization. (b) Performance of FPI stabilization in terms of phase fluctuation around the quadrature point. The sampling frequency is 40 samples per second.

3.4.1.2 Optimal modulation frequency and depth

Fig. 3.5(a) shows the measured second harmonic (2*f*) output signal of the FPI for varying modulation voltage when the HCF gas cell is filled with 1000 ppm ethane balanced with nitrogen. The experiments were conducted at room conditions. The pump laser is centered at 3348.15 nm and the modulation frequency is 7 kHz. The optimal modulation voltage is 45 mV, which coincides well with an optimal modulation depth of 2.2 times the absorption linewidth considering the conversion coefficient of the current controller and the ICL.

Fig. 3.5(b) shows the dependence of 2*f* output signal and noise level on the modulation frequency with the modulation voltage fixed at 45 mV. The 2*f* signal decreases with the increasing modulation frequency and the -3dB roll-off frequency is about 20 kHz, which is determined mainly by the thermal conduction process in the HCF and the ns-level relaxation time of ethane can be ignored [14]. The noise was measured by filling the HCF with pure nitrogen at room condition. The best SNR is achieved around 7 kHz, as shown in the inset of the figure.

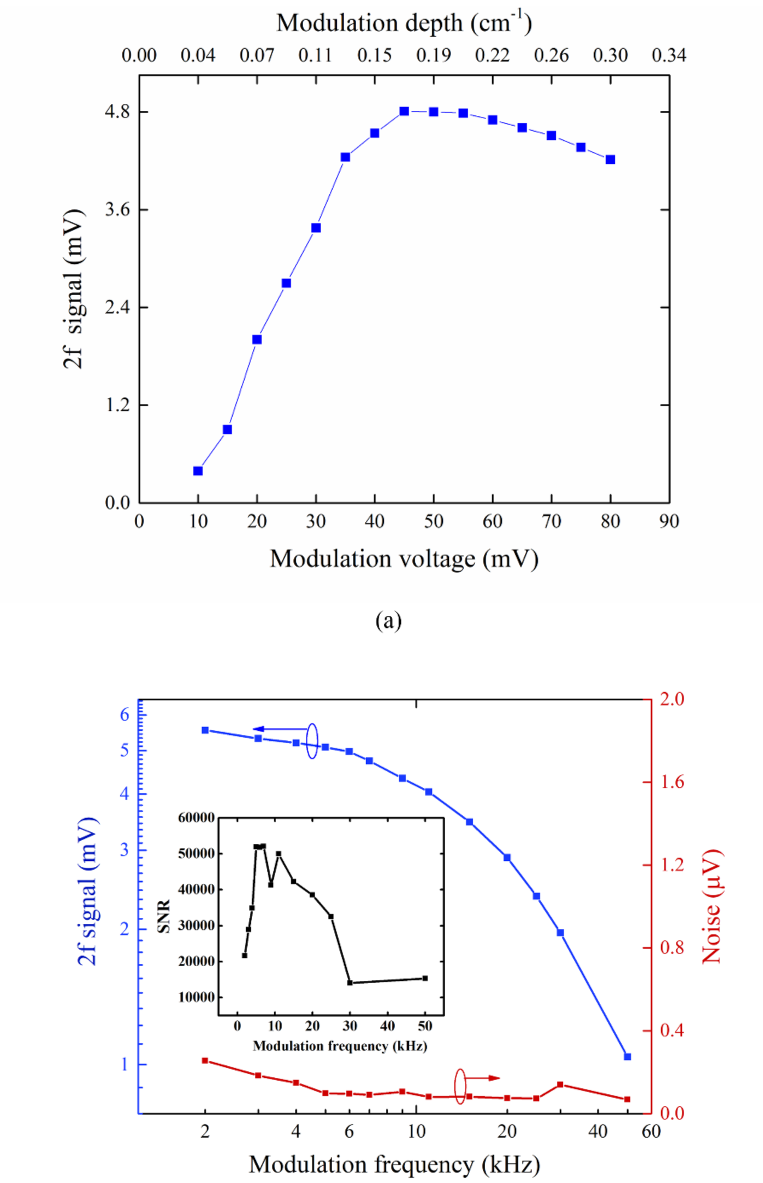

(a)

(b)

Figure 3.5. (a) 2*f* output signal at the absorption line center as a function of modulation voltage. (b) 2*f* signal and the s.d. of the noise as functions of modulation frequency. The inset shows the SNR as a function of modulation frequency.

3.4.1.3 Ethane detection with high sensitivity and stability

Ethane detection experiments were conducted by filling different concentrations of ethane balanced with N_2 into the gas cell. The HCF gas cell was placed inside a gas chamber with a volume of about 1.8 L and the gas chamber was filled with gas sample through a flowmeter, whose outlet pressure is slightly higher than 1 atm. It took about

300 s for the signal to reach 90% of the maximum value with a flow rate of 500 standard cubic centimeter per minute (SCCM). The slow response is not limited by the HCF gas cell but by the size of the chamber, and can be significantly shortened with a smaller chamber and/or by introducing microchannels along the HCF[15]. Fig. 3.6(a) shows the 2*f* lock-in output with 1 ppm ethane filled into the AR-HCF and when the pump is tuned across the absorption line at 3348.15 nm. Fig. 3.6(b) shows the 2*f* lock-in output over a period of 2 minutes when the gas cell was filled with pure N_2. The s.d. of noise is 0.095 μV, giving an SNR of ~ 80 and a LOD of 13 ppb, corresponds to NEA of 7.7×10^{-7} cm^{-1}, for an SNR of unity and 1 s lock-in time constant with filter slope of 18 dB/Oct, corresponding to a detection bandwidth of 0.094 Hz. This LOD is just 2 times higher than the shot-noise-limited NEA, which is calculated to be 3.8×10^{-7} cm^{-1}[2].

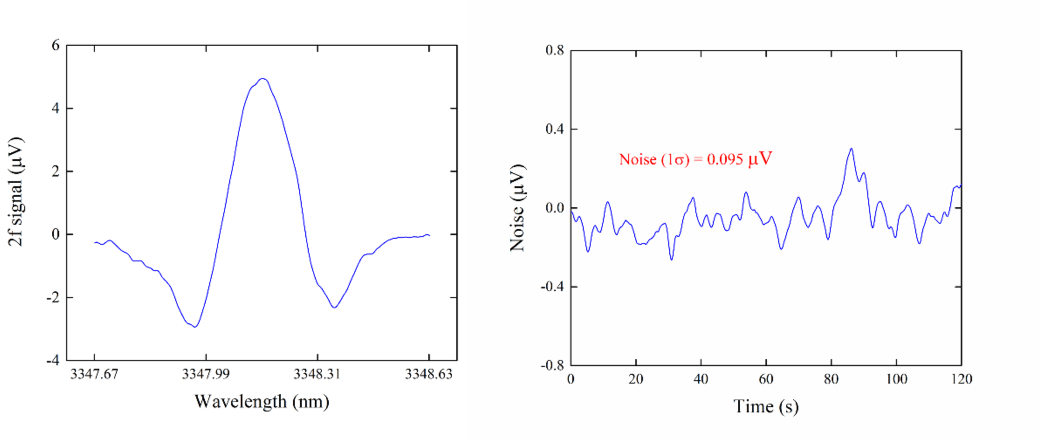

(a) (b)

Figure 3.6. (a) 2*f* lock-in output signal as a function of pump wavelength for 1 ppm ethane in nitrogen. (b) 2*f* signal when the gas cell was filled with pure nitrogen and the pump laser was fixed at 3348.15 nm.

Allan deviation analysis was conducted with the noise data over a period of 4 hours, and the results are shown in Fig. 3.7. The optimal averaging time τ is determined to be 410 s, at which the s.d. of noise is 0.019 μV, corresponding to a noise equivalent concentration (NEC) of 2.6 ppb ethane and a calculated NEA of 1.5×10^{-7} cm^{-1}.

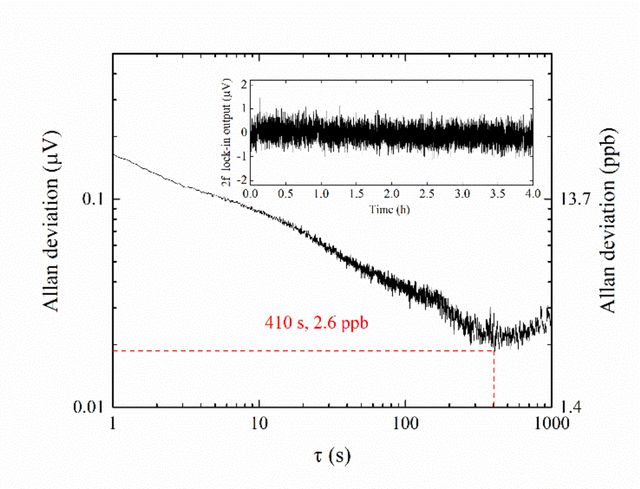

Figure 3.7. Allan deviation analysis of the baseline noise over a period of 4 hours. The inset is the time trace. The time constant of the lock-in amplifier is 100 ms.

The peak-to-peak values of the 2*f* signal at different ethane concentrations are shown in Fig. 3.8. The 2*f* signal amplitude increases approximately linearly with the gas concentration with an R-square value of 0.9993.

The system stability was tested by repeatedly scanning the pump wavelength across the absorption line of ethane at 3348.15 nm and the results for 1000 ppm ethane balanced with nitrogen with a pump power of ~1.5 mW are shown in Fig. 3.9. During the stability experiment, the gas cell keeps being filled with ethane slowly (5 SCCM) to maintain constant gas concentration. The peak-to-peak value of the 2f signal varies ~ 2.2% over a period of 8 hours. This instability is believed to due mainly to pump power fluctuation in the HCF since the weak reflections of the pump at the HCF/SMF joints would interfere with the main pump beam and cause pump power fluctuation within the FPI cavity.

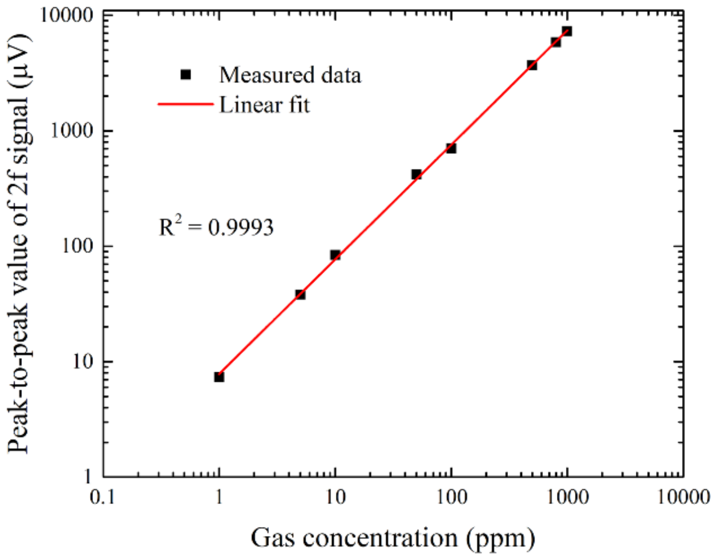

Figure 3.8. The peak-to-peak value of the 2f signal as a function of ethane concentration.

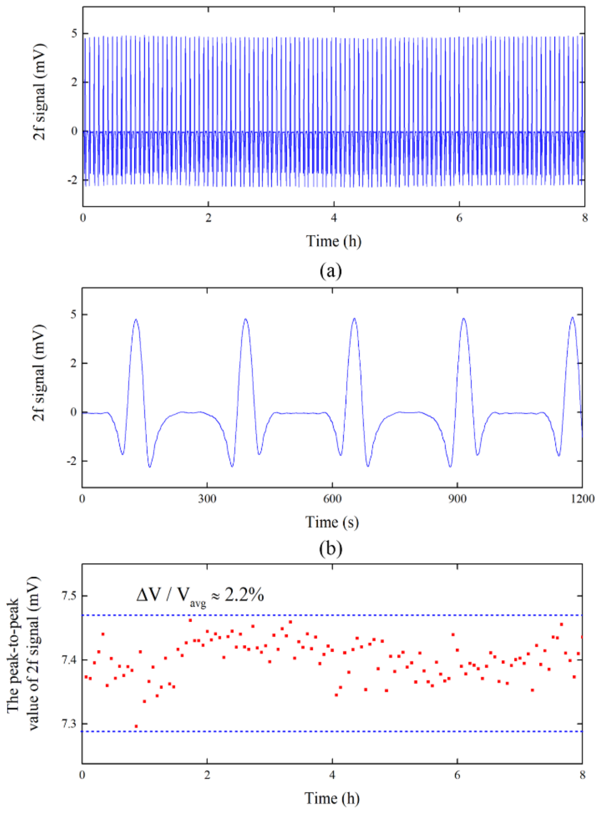

(a)

(b)

(c)

Figure 3.9. Results of long-term stability test. (a) 2f lock-in output signal over a period of 8 hours. (b) 2f signal over a period of 1200 seconds. (c) The variation of the peak-to-peak value of the 2f signal over 8 hours.

Table 3.1 summarizes the performance of MIR gas sensors with HCF gas cells. The NEA·L is given here for a fair comparison, which is independent of gas type and absorption strength. The last three rows are the results of this work for different integration time. The current work achieves the smallest NEA·L (for 410 s), which is about one order of magnitude better than the state-of-the-art MIR HCF gas sensors [26]. Our system is simple, compact and has good long-term stability, which is essential for practical applications.

Table 3.1 Performance of MIR HCF gas sensors

Gas	Gas cell	Wavelength	Technique	Length (L)	NEA·L	Integration time
N_2O [16]	HC-NCF	3.60 μm	DAS	120 cm	3.0×10^{-5}	40s
Methane [17]	Kagome HCF	3.33 μm	TDLAS	130 cm	4.6×10^{-4}	Not stated
Methane [18]	Kagome HCF	3.33 μm	CLaDS	130 cm	4.0×10^{-4}	1s
N_2O [19]	Revolver HCF	4.53 μm	TDLAS	320 cm	1.2×10^{-4}	1s
N_2O [5]	Capillary Fiber	4.46 μm	PTI-MZI	25.0 cm	5.1×10^{-4}	150s
Formaldehyde [20]	HC-NCF	3.60 μm	PTI-MZI	120 cm	9.2×10^{-5}	Not stated
Ethane (this work)	HC-NCF	3.34 μm	PTI-FPI	14.0 cm	1.0×10^{-5}	1s
					3.5×10^{-6}	100s
					2.0×10^{-6}	410s

CLaDS: chirped laser dispersion spectroscopy.

3.4.1.4 Conclusion of ethane detection

In summary, we have demonstrated a stable, compact, and highly sensitive ethane sensor with an AR-HCF gas cell that transmits both MIR and NIR signals with low loss. By launching the MIR pump and the NIR probe into the gas cell simultaneously from the opposite ends of the HCF, the separation of the MIR pump optics and the NIR probe circuit is achieved. Such a design of gas cell allows the use of a MIR pump to access the strongest absorption lines to generate larger PT phase modulation and a cost-effective NIR probe interferometer to detect the phase modulation with high sensitivity. With a 14-cm-long AR-HCF gas cell, a 3348.15 nm pump laser, and a 1550 nm probe FPI stabilized at quadrature, we demonstrated ethane detection with NEC of 13 ppb for 1 s TC. The NEC goes down to 2.6 ppb for 410 s averaging time, corresponds to NEA·L of 2.0×10^{-6}, the smallest among all the MIR HCF gas sensors reported so far, to the best of our knowledge. The system instability is about 2.2% over a period of 8 hours. The high sensitivity, high stability, and simple structure of the detection system are promising for field applications. The sensitivity and stability could be further improved by optimizing the gas cell design to enhance the fringe contrast for probe FPI and to reduce the interference effect due to residual pump reflections. Similar sensing systems may be implemented for many other gases that have strong absorption in the MIR.

3.5 Noise analysis of FPI PTS

Furthermore, a noise analysis was conducted to identify the sources of noise in the FPI.

For low finesse FPI, the reflected intensity used in Equation 3.2 is based on $R_1 = R_2 = R$, if we consider the two reflected surfaces separately, it can be regard as:

$$I_R = R_1 I_0 + \eta R_2 I_0 + 2\sqrt{\eta R_1 R_2} I_0 \cos(\varphi_0 + \Delta\varphi) \tag{3.4}$$

R_1 and R_2 respectively denote the reflectivity of the front and rear surfaces, I_0 is the incident light intensity, and η represents the overall coupling efficiency of light from the single-mode fiber into the hollow-core fiber and back into the single-mode fiber. φ_0 represents the inherent phase difference of the Fabry-Perot interferometer, and when the interferometer operates at the orthogonal point, φ_0 is $\pi/2$. $\Delta\varphi$ is the phase change induced by the photothermal effect, and under the weak absorption approximation.

The system noise mainly comprises electrical noise and optical noise, where the latter can be further divided into shot noise, intensity noise, and phase noise. Therefore, the standard deviation of the system noise can be expressed as:

$$\sigma = \sqrt{\sigma_E^2 + \sigma_S^2 + \sigma_I^2 + \sigma_P^2} \tag{3.5}$$

where $\sigma_E, \sigma_S, \sigma_I$ *and* σ_P denote the standard deviations of the electrical noise, shot noise, intensity noise, and phase noise, respectively. Firstly, the noise standard deviation was measured with the PD receiving no light power, and it was found to be approximately 0.07 μV, which is significantly higher than the noise floor of the lock-in amplifier. Hence, the PD noise is the primary source of the electrical noise in the system. Next, the detected laser output was directly injected into the PD through a variable attenuator, and the noise level was measured at different received power levels, as shown in Fig. 3.10(a), where the black bars indicate the measured noise standard deviation, and the red circles denote the calculated optical noise standard deviation after removing the electrical noise. When the received power exceeds 100 μW, the noise is almost linearly proportional to the received power, indicating that the noise is primarily dominated by the relative intensity noise of the light source, and the effect of shot noise can be neglected. At a received power of 620 μW, the corresponding intensity noise was approximately 0.73 μV.

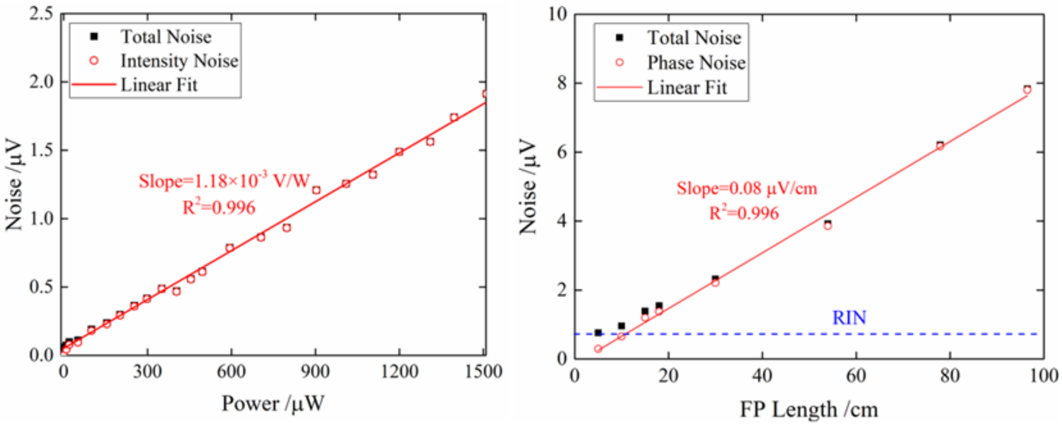

(a) (b)

Figure 3.10 The relationship between the noise and received power in 15-cm-long HCF gas cell; (b) The relationship between the noise and the length of HCF FPI with received power of 620 μW

Moreover, samples with similar interference contrast but different lengths of HCF were prepared, and their noise standard deviations were measured, as shown by the black bars in Fig. 3.10(b). The phase noise was then calculated after considering the intensity noise of 0.73 μV, as shown by the red circles. The phase noise increased linearly with the HCF length, with a slope of approximately 0.08 μV/cm, and the phase noise of the 15-cm sample was approximately 1.2 μV. The phase noise of the narrow linewidth fiber laser used in the experiment was approximately $0.28\mu rad{\bullet}Hz^{-1/2}{\bullet}m^{-1}$ at 20 kHz. The PD amplification coefficient was 100 times, corresponding to a voltage-phase coefficient of 42 V/rad, and the detection bandwidth of the lock-in amplifier was 0.094 Hz. Using these parameters, the phase noise of the laser for a 15-cm- long HCF was calculated to be approximately 1.1 μV, which is consistent with the experimental result.

According to Equations 3.5, when the laser noise is the primary source of noise, the SNR of phase detection can be expressed as:

$$R_{\mathrm{SN}} = \frac{2\sqrt{\eta R_1 R_2} I_0 k^* \alpha C L P_{\mathrm{pump}}}{\sqrt{\left[(R_1+\eta R_2) I_0 \delta_I\right]^2 + \left[2\sqrt{\eta R_1 R_2} I_0 \delta_P L\right]^2}} \tag{3.6}$$

where δ_I and δ_P represent the normalized intensity noise and phase noise, respectively. If a high-performance narrow linewidth laser and a shorter sample length are used, the phase noise is smaller while the intensity noise is dominant. By optimizing the reflectivity of the end face or compensating for the power loss due to fiber coupling, such that $R_1 = \eta R_2$, the optimal SNR can be achieved. However, when a long probe or a wide linewidth light source is used, the phase noise is dominant, as shown by Equation 3.6. In this case, the signal and noise are both proportional to the FPI length, and the SNR of phase detection is only related to the photothermal efficiency, and increasing the FPI length or optimizing the coating parameters cannot improve the SNR.

Based on the above analysis, in the experimental system used in this study, the main sources of system noise are the laser's phase noise and intensity noise. Although intensity noise can be suppressed by balanced detection, even if it is eliminated, the overall noise level can only be reduced by about 12% due to the high level of phase noise. In addition, while increasing the length of the gas cell can increase the amplitude of the photothermal signal, it also increases the phase noise, which leads to phase noise dominance. In this case, further increasing the length cannot improve the SNR. Therefore, the F-P structure is more suitable for using a shorter gas cell length. Its characteristics of small size, no electromagnetic interference, single-ended detection, and the ability for multi-point deployment make this structure a good candidate for practical applications.

3.6 Discussion

Through noise analysis, we have learned that the main source of noise in FPI is the phase noise of the laser. Therefore, for the FPI structure, increasing the length of the sensing HCF beyond a certain point does not result in a corresponding increase in SNR. In practical applications, the linewidth of different types of lasers can vary from kilohertz to megahertz. So, what are the length limitations for the FPI configuration with different lasers? We obtain the results through simulations.

The root-mean-square (RMS) of the FPI output fluctuation induced by the laser phase noise may be expressed as:

$$\sigma_P = R_{PD} P \frac{2}{\sqrt{\tau_c}} |\tau_d| e^{|\tau_d|/\tau_c} \sqrt{\Delta f} \tag{3.7}$$

Where τ_c is the coherence time of the laser and can be expressed as $\tau_c = 1/\pi\Delta\nu$, $\Delta\nu$ is the linewidth of the probe laser. $\tau_d = 2nL/c$ is the time delay between the two reflected beams. R_{PD} (A/W) is the responsivity factor of the PD, P is the optical power received by the PD, and Δf is the detection bandwidth.

The noise due to the laser intensity fluctuations can be expressed as:

$$\sigma_I = R_{PD} P \sqrt{RIN \cdot \Delta f} \tag{3.8}$$

where RIN is the relative intensity noise of the probe laser.

Shot noise is a quantum limited noise, which could be simply expressed as:

$$\sigma_S = \sqrt{2qR_{PD}P\Delta f} \tag{3.9}$$

where q is electron charge.

We neglected electrical noise as it is significantly smaller than optical noise. The received optical power at the PD was set at 400 μW, and we assumed that the intensity noise of the lasers was consistent, and RIN is equal to 140 dBc/ Hz. The detection bandwidth is set to 1 Hz and R_{PD} is set to 1 A/W for calculation convenience. We calculated the total noise for lasers with different linewidths using Equation 3.5.

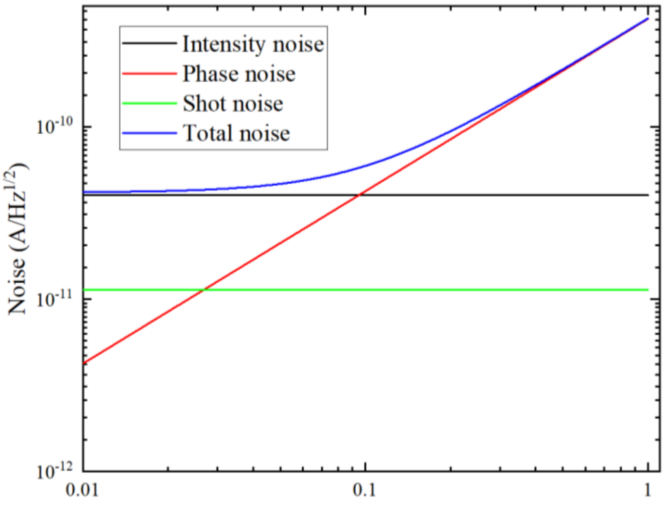

(a) Length (m)

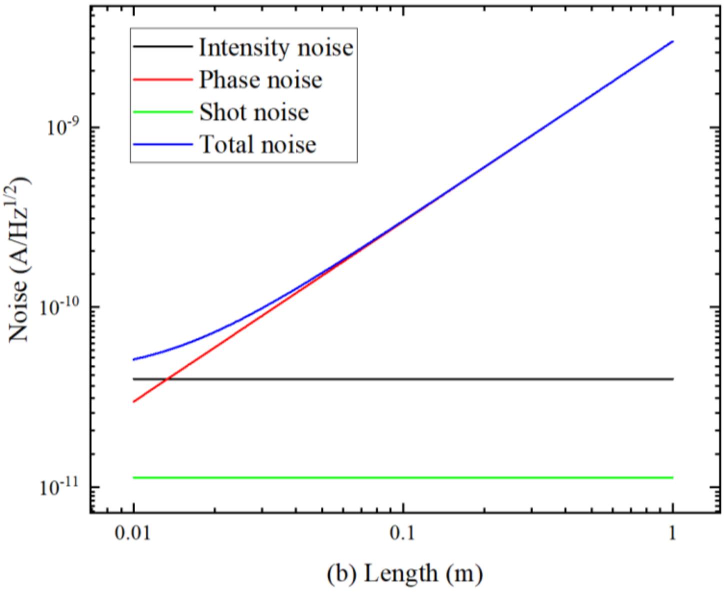

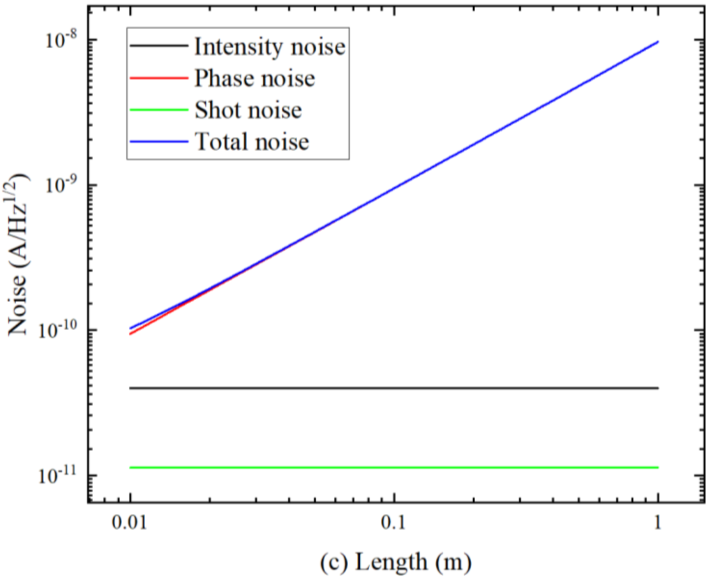

Figure 3.11 The relationship between noise and FPI length for a probe laser with linewidth (a) 2 kHz. (b) 100 kHz, and (c) 1 MHz.

Based on the simulation results in Fig. 3.11(a), it can be observed that when using a high-performance laser with a narrow linewidth, such as the fiber laser used in our experiment with a linewidth of 2 kHz, the dominant sources of noise are phase noise and intensity noise when the FP length is less than 30 cm. However, beyond 30 cm, the noise is primarily composed of phase noise. In other words, even with a high-performance laser with a narrow linewidth like the fiber laser, the FP length can only be up to 30 cm and increasing it further will not improve the SNR.

Regarding the laser with a linewidth of 100 kHz used in Fig. 3.11 (b), phase noise already dominates when the FP length exceeds 5 cm. As shown in Fig. 3.11 (c), for most DFB lasers with linewidths in the MHz range, their phase noise is significantly higher than other optical noise sources even when the FP length is only 1 cm. Therefore, for FP structures, due to their inherent optical path difference, they have higher requirements for the linewidth of the light source. This indicates that FPI structures are more suitable for compact sensors with a shorter HCF length.

3.7 Summary

In this chapter, we have demonstrated the capability of a MIR HCF PTS system employing a FPI, for sensitive detection of individual gases, like ethane. With a 14-cm-long AR-HCF gas cell, a 3348.15 nm pump laser, and a 1550 nm probe FPI stabilized at quadrature, we demonstrated ethane detection with NEC of 13 ppb for 1 s TC. The NEC goes down to 2.6 ppb for 410 s averaging time. Furthermore, we conducted noise analysis of the FPI and found that the primary noise source is the phase noise of the probe laser. Additionally, we investigated the relationship between the FPI noise and its length when different linewidth lasers were used as probes. We discovered that even with a high-performance fiber laser of 2 kHz linewidth, the FP length limitation is approximately 30 cm. Beyond this length, the SNR does not improve any longer.

3.8 Reference

1. F. Yang, W. Jin, Y. Cao, H. L. Ho, and Y. Wang, "Towards high sensitivity gas detection with hollow-core photonic bandgap fibers," Optics express **22**, 24894-24907 (2014).
2. W. Jin, Y. Cao, F. Yang, and H. L. Ho, "Ultra-sensitive all-fibre photothermal spectroscopy with large dynamic range," Nature Communications (2015).
3. F. Yang, Y. Tan, W. Jin, Y. Lin, Y. Qi, and H. L. Ho, "Hollow-core fiber Fabry–Perot photothermal gas sensor," Optics Letters **41**, 3025 (2016).
4. P. Zhao, Y. Zhao, H. Bao, H. L. Ho, W. Jin, S. Fan, S. Gao, Y. Wang, and P. Wang, "Mode-phase-difference photothermal spectroscopy for gas detection with an anti-resonant hollow-core optical fiber," Nature communications **11**, 1-8 (2020).
5. Z. Li, Z. Wang, F. Yang, W. Jin, and W. Ren, "Mid-infrared fiber-optic photothermal interferometry," Optics letters **42**, 3718-3721 (2017).
6. I. J. Simpson, F. S. Rowland, S. Meinardi, and D. R. Blake, "Influence of biomass burning during recent fluctuations in the slow growth of global tropospheric methane," Geophysical Research Letters **33** (2006).
7. Y. Xiao, J. A. Logan, D. J. Jacob, R. C. Hudman, R. Yantosca, and D. R. Blake, "Global budget of ethane and regional constraints on US sources," Journal of Geophysical Research: Atmospheres **113** (2008).

8. P. Paredi, S. A. Kharitonov, and P. J. Barnes, "Elevation of exhaled ethane concentration in asthma," American journal of respiratory and critical care medicine **162**, 1450-1454 (2000).
9. C. S. Patterson, L. C. McMillan, C. Longbottom, G. M. Gibson, M. J. Padgett, and K. D. Skeldon, "Portable optical spectroscopy for accurate analysis of ethane in exhaled breath," Measurement Science and Technology **18**, 1459 (2007).
10. S.-f. Gao, Y.-y. Wang, W. Ding, D.-l. Jiang, S. Gu, X. Zhang, and P. Wang, "Hollow-core conjoined-tube negative-curvature fibre with ultralow loss," Nature communications **9**, 1-6 (2018).
11. S. Gao, Y. Wang, and P. Wang, "Silica-based modeless hollow-core fiber for broadband mid-IR guidance," in *2017 Conference on Lasers and Electro-Optics Pacific Rim (CLEO-PR)*(IEEE2017), pp. 1-2.
12. S. E. Bialkowski, *Photothermal spectroscopy methods for chemical analysis* (John Wiley & Sons, 1996).
13. H. Bao, Y. Hong, W. Jin, H. L. Ho, C. Wang, S. Gao, Y. Wang, and P. Wang, "Modeling and performance evaluation of in-line Fabry-Perot photothermal gas sensors with hollow-core optical fibers," Optics express **28**, 5423-5435 (2020).
14. R. Holmes, G. Jones, and N. Pusat, "Vibrational relaxation in propane, propylene, and ethane," The Journal of Chemical Physics **41**, 2512-2516 (1964).
15. Y. L. Hoo, S. Liu, H. L. Ho, and W. Jin, "Fast Response Microstructured Optical Fiber Methane Sensor With Multiple Side-Openings," IEEE Photonics Technology Letters **22**, 296-298 (2010).
16. C. Yao, S. Gao, Y. Wang, P. Wang, W. Jin, and W. Ren, "Silica hollow-core negative curvature fibers enable ultrasensitive mid-infrared absorption spectroscopy," Journal of Lightwave Technology **38**, 2067-2072 (2019).
17. M. Nikodem, K. Krzempek, G. Dudzik, and K. Abramski, "Hollow core fiber-assisted absorption spectroscopy of methane at 3.4 µm," Optics express **26**, 21843-21848 (2018).
18. K. Krzempek, K. Abramski, and M. Nikodem, "Kagome hollow core fiber-based mid-infrared dispersion spectroscopy of methane at sub-ppm levels," Sensors **19**, 3352 (2019).
19. M. Nikodem, G. Gomółka, M. Klimczak, D. Pysz, and R. Buczyński, "Demonstration of mid-infrared gas sensing using an anti-resonant hollow core fiber and a quantum cascade laser," Optics Express **27**, 36350-36357 (2019).
20. C. Yao, S. Gao, Y. Wang, P. Wang, W. Jin, and W. Ren, "MIR-pump NIR-probe fiber-optic photothermal spectroscopy with background-free first harmonic detection," IEEE Sensors Journal (2020).

Chapter 4

4 HCF FPI-PTS using hybrid MIR/NIR pumps for multi-gas detection with FDM

4.1 Introduction

Multicomponent gas sensing is crucial for a variety of applications, including climate and air quality monitoring, biomedical functions, manufacturing, food, and electronics industry [1-4]. Past systems have employed DAS, TDLAS, and PAS, utilizing various configurations of light sources, detectors, and filters to detect different gases. However, these systems often involve complex optical setups and the detection limits are at the ppm level, due to weak absorption or short optical paths [5-8].

In this chapter, we demonstrate the simultaneous detection of multiple gases with HCF-PTS by use of a single HCF gas cell with broadband transmission from NIR to MIR. Three pump lasers with wavelengths of 1.39 μm, 2.00 μm, and 4.60 μm, corresponding respectively to the absorption lines of H_2O, CO_2, and CO, are frequency-division multiplexed (FDM) to generate photothermal phase modulations simultaneously at different frequencies and a common probe FPI operating at 1.55 μm is used to detect the phase modulations. This simple system can combine multiple pump beams from NIR to MIR for the most efficient interaction among the gas sample, the pump beams, and the probe beam in the same gas cell, which provides freedom for selecting pump wavelengths by comprehensively considering the requirements of gas absorption line strength, component performance, and cost, to meet the practical application needs. The probe interferometer operates in the telecom band where cost-effective high-performance fiber-optic components are readily available, minimizing the usage of expensive MIR components such as photodetectors and beam combiners/splitters.

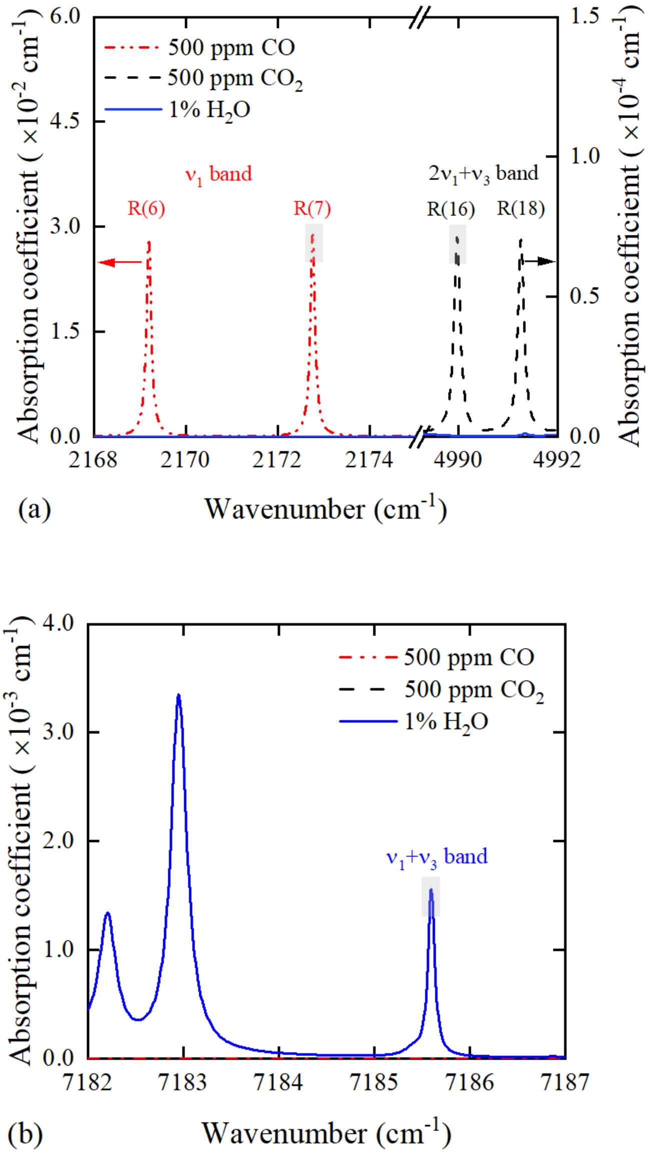

Figure 4.1 Calculated absorption spectrums of CO, CO_2, and H_2O at 296 K and 1 atm.

4.2 Design and fabrication of the gas cell

Selection of absorption lines. According to the HITRAN2016 database, H_2O and CO_2 show strong absorption in the NIR band with line strength higher than 1×10^{-21} $cm^{-1}/(molec\cdot cm^{-2})$. For sensitive detection of CO, the absorption line in the MIR band with line strength higher than 4×10^{-19} $cm^{-1}/(molec\cdot cm^{-2})$ is chosen. Figure 4.1 shows the calculated absorption coefficient of H_2O, CO_2, and CO at 296 K and 1 atm. The absorption coefficient of 1% H_2O at 7185.6 cm^{-1} (1392 nm), 500 ppm CO_2 at 4990.0 cm^{-1} (2003 nm), and 500 ppm CO at 2172.8 cm^{-1} (4602 nm) are 1.56×10^{-3} cm^{-1}, 7.14×10^{-5} $cm^{-1}$and 2.91×10^{-2} cm^{-1}, respectively

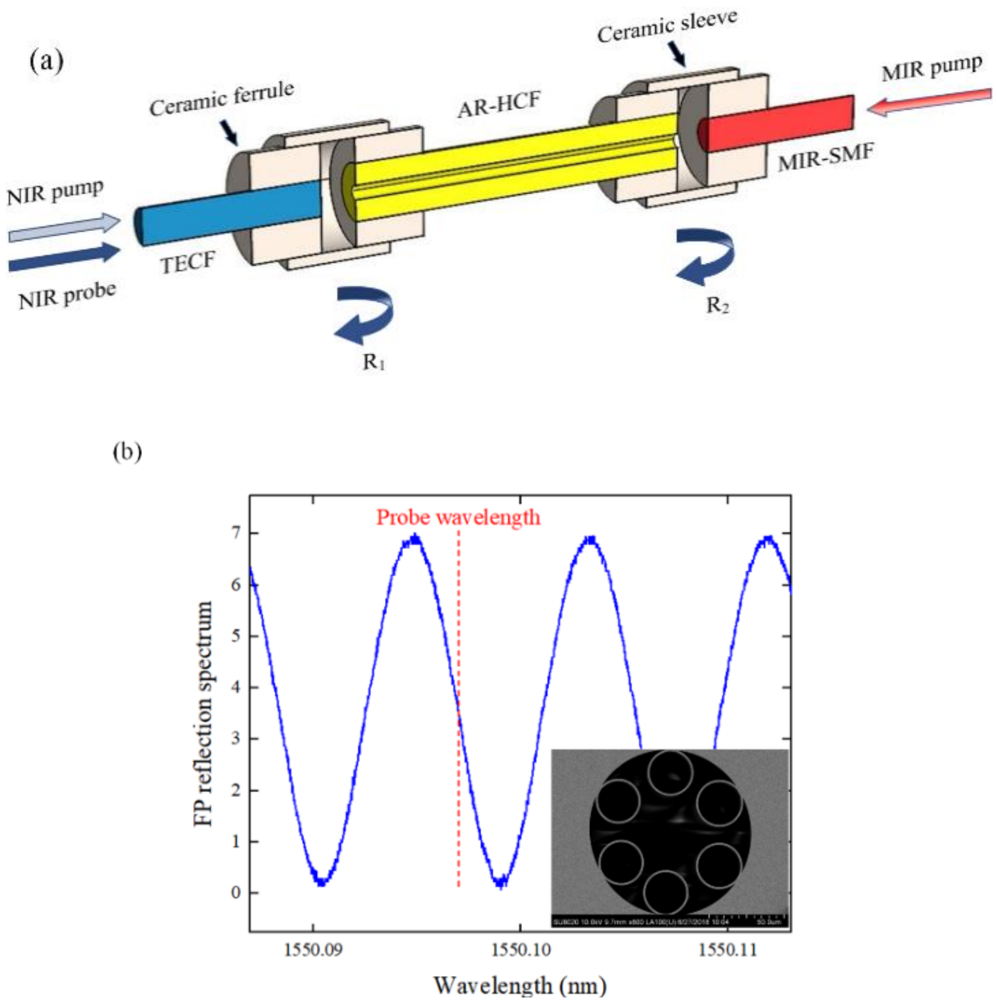

Figure 4.2. (a) Schematic of the AR-HCF gas cell. (b) The reflected spectrum of FPI. The inset is the cross-section of AR-HCF.

Fig. 4.2(a) illustrates the structure of the gas cell. A 13-cm-long AR-HCF serves as the sensing fiber, and its cross-section is shown in the inset of Fig. 4.2(b)[9]. A thermally-expanded-core fiber (TECF) and a solid InF_3-based MIR single-mode fiber (SMF) are used for NIR and MIR transmission, respectively. Different fibers are connected using ceramic ferrules and sleeves. The NIR and MIR light beams are launched into the gas cell from the opposite ends of the HCF, avoiding the use of a dichroic mirror to combine them. The fiber ends are not coated and the natural reflection (~4%) at the TECF/HCF and HCF/MIR-SMF joints form a low-finesse FPI to detect the photothermal phase modulation resulting from pump absorption of gas molecules. The reflected spectrum around 1550 nm, measured with a tunable narrow-linewidth laser in combination with a photodetector and an oscilloscope, is shown in Fig. 4.2(b). The entire sensing unit is placed and sealed in a glass tube with a volume of 90 mL.

4.3 Setup for gas detection

As shown in Fig. 4.3, the experimental system can be divided into four parts: a NIR pump module, a MIR pump module, a NIR probe module, and a data processing module. The NIR pump module comprises two DFB lasers, with wavelengths of 1392 nm and 2003 nm, respectively, and a thulium-doped fiber amplifier (TDFA). In the MIR pump module, light from a 4602 nm QCL is coupled into the HCF through a MIR-SMF by a coated silica lens with overall coupling efficiency of 25 %.

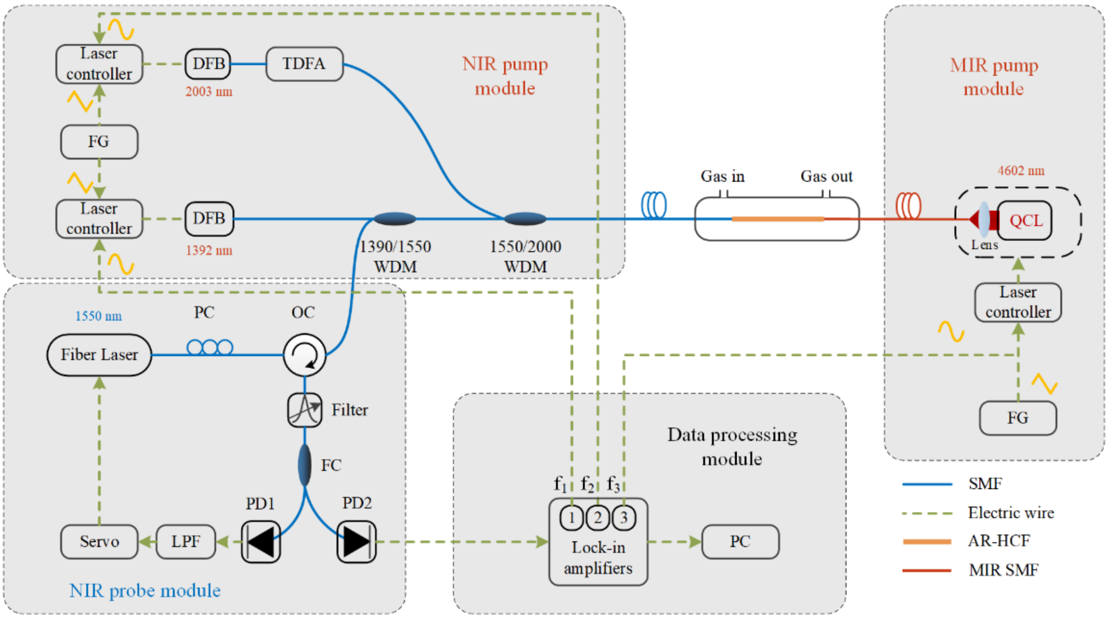

Figure 4.3 Experimental set-up for multi-component gas detection with 13-cm-long AR-HCF gas cell. FC, fiber coupler; FG, function generator; LPF, low-pass filter; OC, optical circulator; PC, personal computer; PD, photodetector; TDFA, Thulium- Doped Fiber Amplifier; WDM, wavelength division multiplexer.

The effective pump power delivered into the HCF is estimated to be 2 mW at 1392 nm, 200 mW at 2003 nm, and 5 mW at 4602 nm. The wavelengths of these pump lasers are modulated sinusoidally at different frequencies (f_1, f_2, and f_3) and scanned slowly across the gas absorption lines by applying triangular waves to the laser controllers. The probe laser at 1550 nm is servo-controlled by use of the DC component of the reflected signal, detected by photodetector 1 (PD1), to work at the quadrature point of the FPI. The reflected signal is also detected by PD2, which is further demultiplexed and demodulated by three LIA modules at the second harmonic of the modulation frequencies (i.e., $2f_1$, $2f_2$, and $2f_3$). The use of FDM allows the detection of multiple gases simultaneously instead of sequentially one by one as in the TDM scheme [8].

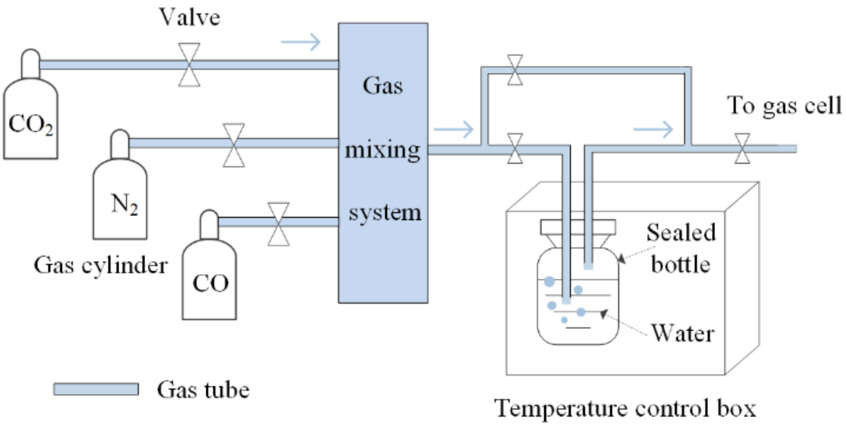

Figure 4.4 Gas mixing system for gas sample preparation.

Figure 4.4 shows the gas mixing system (GMS) system to prepare gas samples. Pure N_2, 1000 ppm CO_2 and 1000 ppm CO are flow-controlled separately and mixed by a three-in-one flow meter to obtain gas samples of different compositions and concentrations. The mixed gas sample goes through a water bath in a sealed bottle. By controlling the water temperature, different water vapor concentrations, determined by the saturated humidity, can be obtained in the mixed gas sample. For example, at 5 and 22 degrees Celsius, the water saturation pressure is 0.873 kPa and 2.645 kPa, which corresponds to estimated water vapor concentrations of 0.86 % and 2.61 % at 1 atm [10], respectively. It should be noted that the water temperature is controlled to be lower than the ambient temperature to avoid liquefaction in the gas tube and gas cell. With this GMS, we can change the concentrations of H_2O, CO, and CO_2 in the mixed gas conveniently.

4.4 Experimental results

Optimal modulation depth and frequency response. We investigated the relationship between the normalized 2f signals and the modulation depth. The three pump lasers are tuned to the absorption line centers of H_2O, CO, and CO_2 and at the same time modulated at 7.5 kHz, 8.0 kHz, and 8.5 kHz, respectively. The results are shown in Figure 4.5. The optimal modulation depths, corresponding maxima of the 2f signals, for H_2O, CO, and CO_2 measurements are 0.16 cm^{-1}, 0.26 $cm^{-1,}$ and 0.33 cm^{-1}, respectively, agreeing well with the theoretical value of 2.2 times the absorption linewidth.

Fig. 4.6 shows the dependence of the normalized 2f signal on the modulation frequency. The frequency response is mainly influenced by two factors [11]: thermal relaxation time and thermal conduction process. For gas with a short relaxation time, such as H_2O, the frequency response is dominated by the thermal conduction process in the hollow core and a smooth response curve with a 3-dB frequency of about 20 kHz is observed. For gas with a long relaxation time, such as CO_2 and CO, the H_2O molecule works as the relaxation promoter [12-14], which leads to the obvious difference in frequency response for different H_2O concentrations. The frequency response of CO at low humidity shows a two-step declining trend, which is dominated by the relaxation time and thermal conduction time, respectively. With higher H_2O concentration, the relaxation time reduces significantly, and the frequency response becomes a one-step declining function dominated by the thermal conduction process. For CO_2, the 2f signal declines a little faster with increasing modulation frequency for low humidity than for high humidity. So, the water vapor can promote the thermal relaxation process of CO.

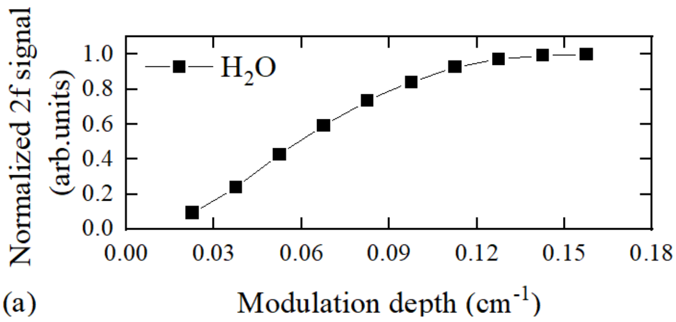

(a)

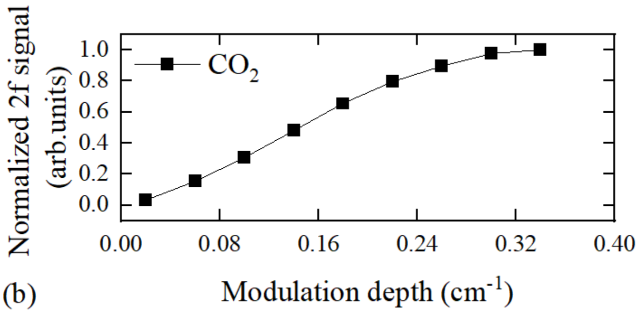

(b)

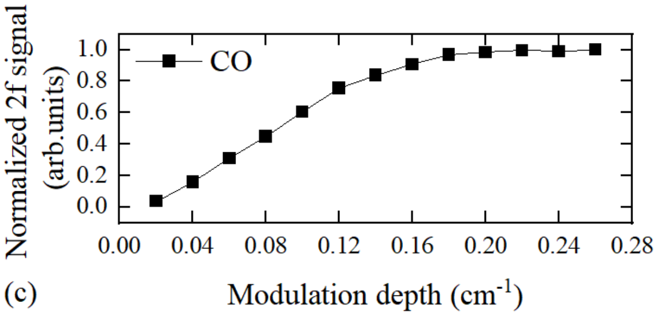

Figure 4.5. Normalized 2f signal at the absorption line center as a function of modulation depth for (a) H_2O, (b) CO_2, and (c) CO.

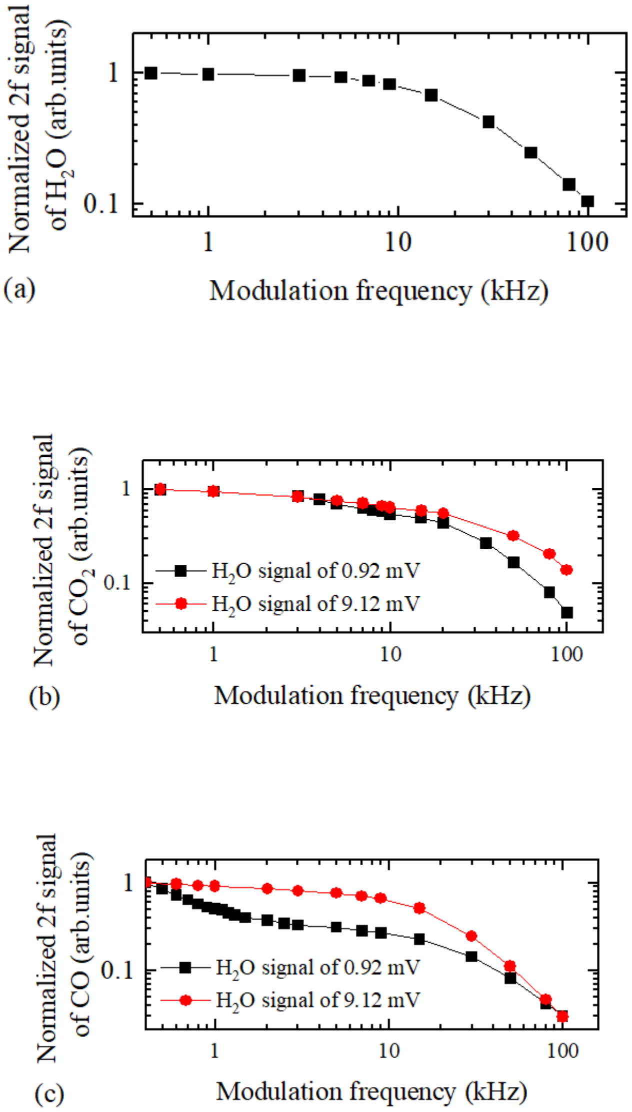

Figure 4.6 Normalized 2f signal at the absorption line center as a function of modulation frequency for (a) H_2O, (b) CO_2, and (c) CO.

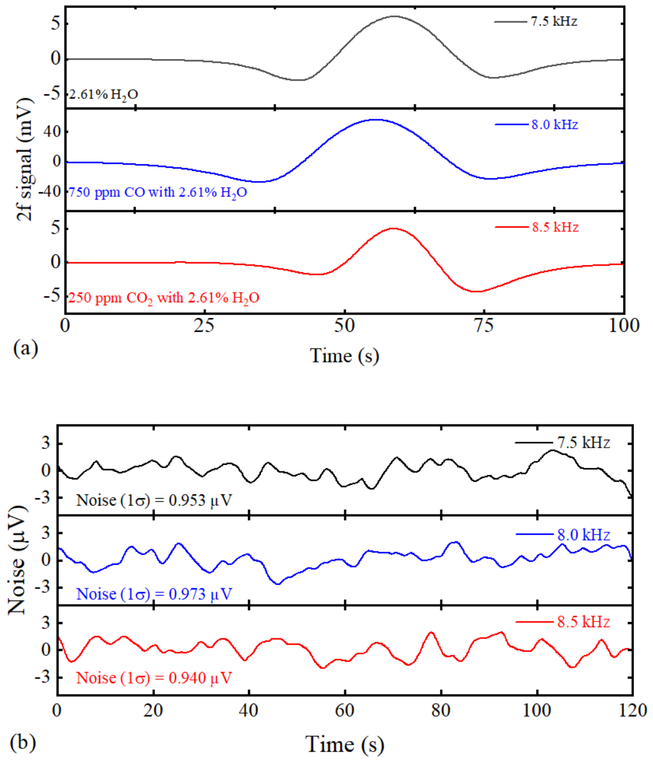

Figure 4.7 2f lock-in outputs as a function of time at different demodulation frequencies. (a) Signals obtained with the pump lasers tuned across respective absorption lines when the gas cell is filled with a mixture of 2.61% H_2O, 750 ppm CO and 250 ppm CO_2. (b) Noise when the gas cell is filled with pure N_2 and all pump lasers are tuned away from the absorption lines.

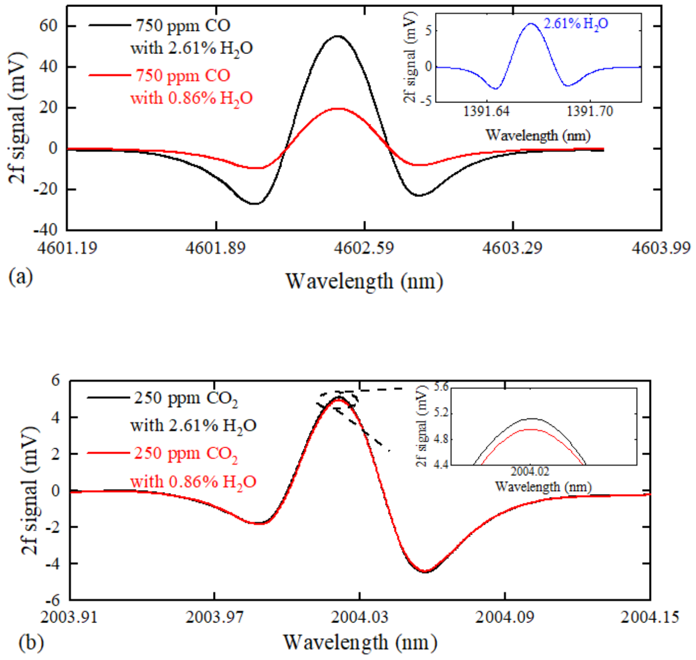

Figure 4.8 2f lock-in output signal as a function of pump wavelength for H_2O, CO, and CO_2.

Simultaneous detection of multiple gases. Multi-gas detection experiment was conducted with gas samples prepared using the GMS with a flow rate of 100 SCCM. The modulation frequencies selected for H_2O, CO, and CO_2 detections are 7.5 kHz, 8 kHz, and 8.5 kHz, respectively, and at these frequencies, no crosstalk was observed among the detected gas signals. The 2f gas signals demodulated at the three different frequencies when the pump wavelengths were simultaneously tuned across the gas absorption lines are shown in Fig. 4.7 (a). The system noise, shown in Fig. 4.7 (b), was evaluated by filling the gas cell with pure N_2 with the pump wavelengths tuned away from the gas absorption lines. The time constant of LIA is 1 s with a filter slope of 18 dB/Oct, corresponding to a detection bandwidth of 0.094 Hz. Fig. 4.8 (a) shows the 2f signals for 750 ppm CO with two different levels of H_2O concentrations.

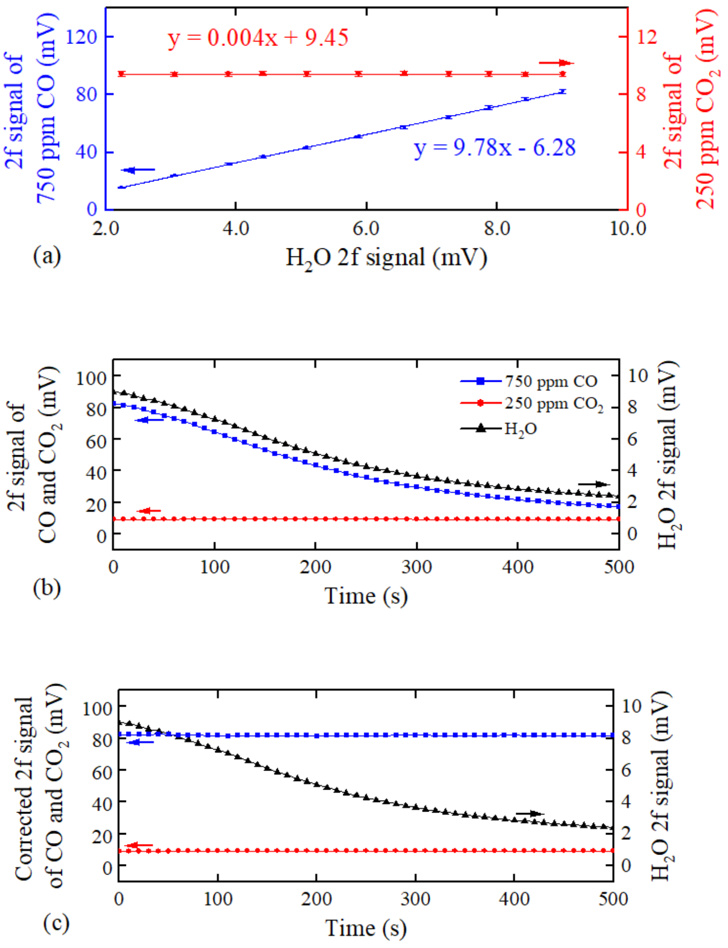

Figure 4.9 (a) The CO and CO_2 signals as a function of the H_2O signal. Error bars show the standard deviation from five measurements. (b) Simultaneous detection over a period of 500 s

when the gas cell is kept filling with the dry gas sample (c) The corrected CO and CO_2 signals by using a linear fit to compensate the effect of varying H_2O concentration.

The signal decreases by almost 3 times when H_2O concentration varies from 2.61 % to 0.86%. The signal for 250 ppm CO_2 only changes slightly with the variation of humidity, as shown in Fig. 4.8(b). The H_2O concentration is monitored simultaneously, as shown in the inset of Fig. 4.8(a), and can be used to compensate for the effect of water vapor on the detection of CO and CO_2, as will be described in the later sections. With 2.61 % H_2O as a thermal relaxation promoter, the LODs for CO, CO_2, and H_2O were estimated, by comparing the signals with the noises, and are 9 ppb, 25 ppb, and 2.7 ppm, respectively, for a SNR of unity (i.e., 1σ).

Fig. 4.9 (a) shows the signals of 750 ppm CO and 250 ppm CO_2 as functions of the H_2O signal. The H_2O concentration was controlled by varying the temperature of the water bottle within the GMS from 1 to 22 degrees Celsius, corresponding to a change of H_2O concentration from 0.65% to 2.61%. It shows that the photothermal signal of CO increases linearly with the water concentration while the signal of CO_2 only changes slightly within the measurement range. Error bars show the standard deviation from five measurements. Fig. 4.9 (b) shows the results of simultaneously detected signals of CO, CO_2, and H_2O over a period of 500 s. The dry mixed gas sample (750 ppm CO and 250 ppm CO_2) is continuously filled into the gas chamber which was originally in a balanced state with a wet gas sample (750 ppm CO, 250 ppm CO_2 and 2.61% H_2O). Therefore, the concentration of CO and CO_2 may be regarded as unchanging while the H_2O concentration keeps dropping. This experiment shows the influence of H_2O concentration on the photothermal signal of CO and CO_2. Based on the linear fit in Fig. 4.9 (a) and using the result of 2.61% H_2O concentration as a reference, we corrected the CO and CO_2 signals, and the results are shown in Fig. 4.9 (c).

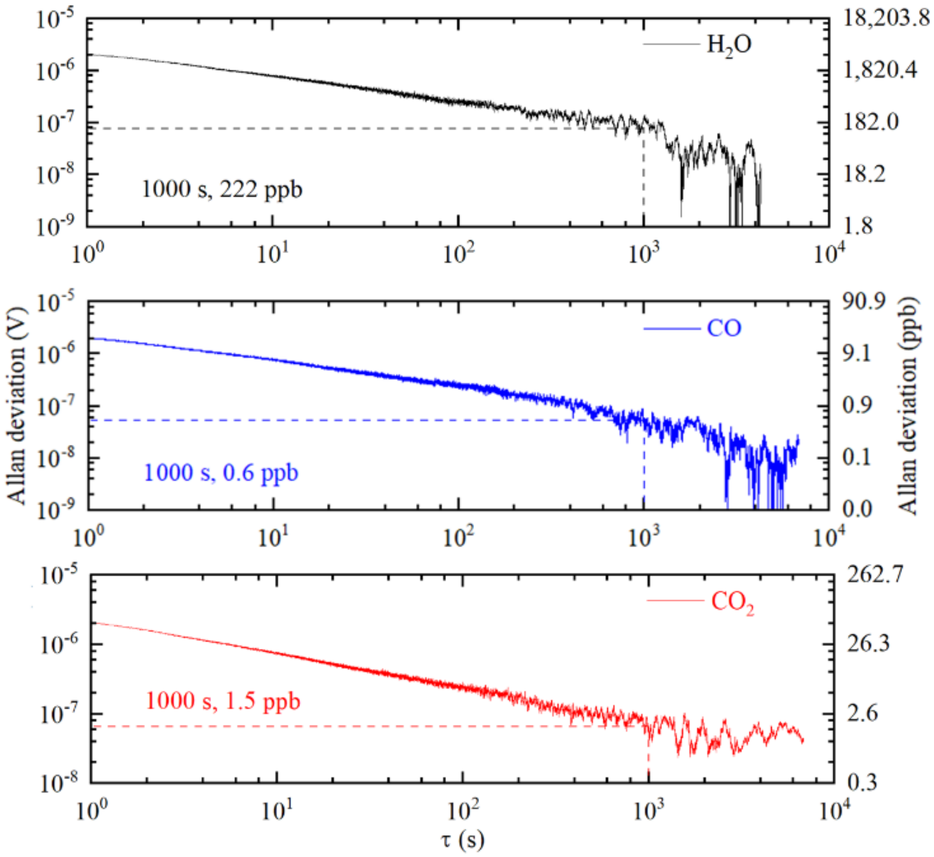

Figure 4.10 Allan deviation analysis of the baseline noise over 2 hours for three gases.

Allan deviation analysis was conducted based on the noise data measured with 100 ms LIA time constant over two hours at the second harmonic frequencies of 7.5 kHz, 8.0 kHz, and 8.5 kHz, simultaneously. The gas cell is filled with pure N_2 and three pump lasers were tuned away from the gas absorption lines. The results for CO, CO_2, and H_2O are shown in Fig. 4.10. With the averaging time τ of 1000 s, the LODs for CO, CO_2, and H_2O go down to 0.6 ppb, 1.5 ppb, and 222 ppb, respectively.

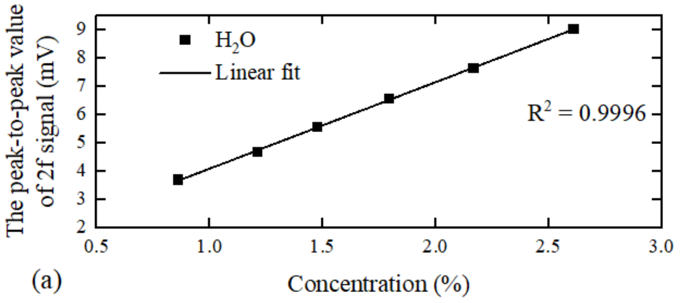

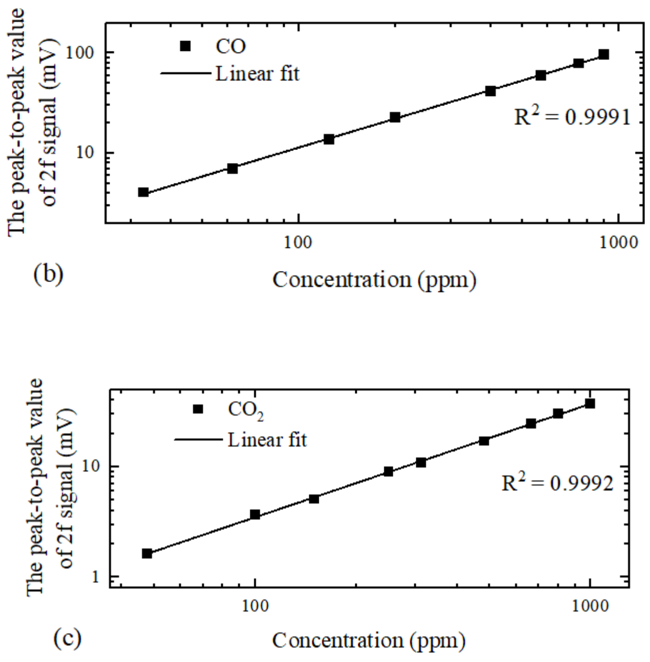

Figure 4.11 The peak-to-peak value of the 2f signal as a function of gas concentration for (a) H_2O, (b) CO and (c) CO_2.

The peak-to-peak values of the 2f signal at different concentrations for CO, CO_2, and H_2O are shown in Fig. 4.11. The 2f signal amplitude increases approximately linearly with gas concentration with R-square value of 0.9991, 0.9992, and 0.9996 for CO, CO_2, and H_2O, respectively. The LIA time constant for signal measurement is 1 s.

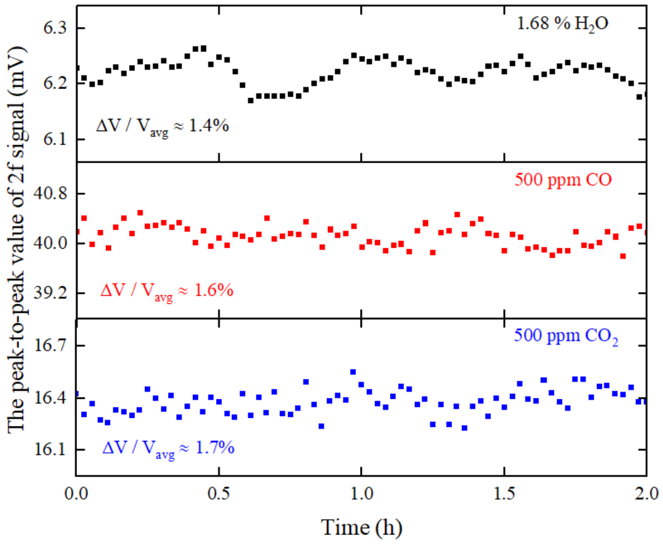

Figure 4.12 The variation of the peak-to-peak value of the 2f signals over 2 hours for simultaneous detection of three gases.

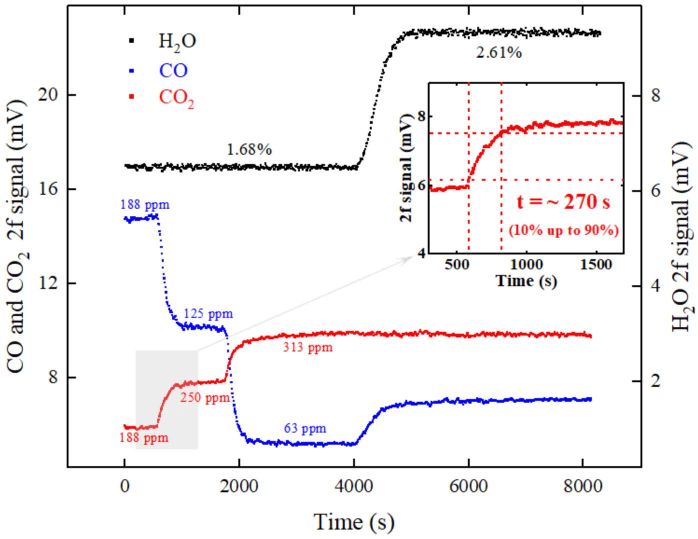

Figure 4.13 The dynamic performance of simultaneous multi-gas detection.

The system stability was also tested by repeatedly scanning the pump wavelengths across the absorption lines of the gases with a 1s LIA time constant and the results are shown in Fig. 4.12. During the stability experiment, the mixed gas samples keep flowing through the gas chamber at 10 SCCM to maintain a constant gas concentration. The peak-to-peak values of the 2f signals over a period of 2 hours vary 1.4%, 1.6%, and 1.7% for H_2O, CO, and CO_2, respectively. Since signal fluctuations for different gases seem uncorrelated, they are believed to be due to power fluctuations of the pump sources.

The dynamic performance of the multi-component gas sensor was tested by scanning the pump wavelengths across the respective gas absorption lines with a 100 ms LIA time constant. Firstly, we set the temperature of the sealed bottle in our GMS at 15 degrees Celsius under which the saturated humidity is 1.68 % at 1 atm[10]. After that, the concentration of CO varies from 188 ppm to 125 ppm, and then to 63 ppm. In the meanwhile, the CO_2 concentration varies from 188 ppm to 250 ppm, and then to 313 ppm. At 4000 s, the water temperature is set to be 22 degrees Celsius and the water concentration changed to 2.61% while the CO and CO_2 concentrations keep unchanged. The peak-to-peak values of the 2f signal are shown in Fig. 4.13. The t_{90} (signal raise from 10% to 90%) time is about 270 s, which is mainly limited by the gas diffusion process into HCF. The response time could be further shortened by introducing microchannels along the HCF [15].

Table 4.1 summarizes the characteristics of some multi-component gas sensors based on laser spectroscopy. NEA and normalized NEA (NNEA) are used here for a fair comparison among different types of sensors. Apart from the high sensitivity, the current work achieves simultaneous detection of multiple gases with absorptions from NIR to MIR by use of a single NIR photodetector. The system is simple, compact, and has good long-term stability, which is essential for practical applications.

Table 4.1 Comparison of multi-component gas sensors based on laser spectroscopy.

Technique	Gases	Wavelength band	Number of Photo/Acoustic detector	NEA (cm^{-1})	NNEA ($cm^{-1}\cdot W\cdot Hz^{-1/2}$)	Multiplexing technique
DAS-WMS (MPGC)[16]	CH_4 N_2O	MIR	1	2.50×10^{-8}		TDM
TDLAS (MPGC)[17]	CH_4 CO N_2O	NIR/MIR	2	6.73×10^{-9}		TDM
HCF-PTS FPI[8]	CH_4 C_2H_2 NH_3	NIR	1	7.43×10^{-9}		TDM
PAS [18]	CO H_2S	NIR	1		8.40×10^{-8}	TDM
QEPAS [19]	NH_3 H_2S	NIR	1		7.80×10^{-9}	FDM
HCF-PTS FPI (this work)	H_2O CO_2 CO	NIR/MIR	1	3.57×10^{-9}	2.33×10^{-9}	FDM

4.5 Discussion

FDM is a useful technique for addressing the simultaneous detection of multiple gases. However, when selecting the frequencies of pump modulation, it is important to avoid signal cross-interference. There are two considerations when choosing the frequencies.

Firstly, we need to consider the detection bandwidth of the LIA, such as the one used in our experiment. For example, with a time constant (TC) of one second, the detection bandwidth of the LIA we used is 0.094 Hz. Therefore, the frequency intervals chosen for FDM should be larger than 0.094 Hz. The specific spacing may need to be calculated based on the parameters of the LIA when using different TC values or LIA models.

Secondly, we need to avoid the impact of modulation-generated harmonics. As shown in the Fig. 4.14, we perform a Fourier transform on the signal from the PD to obtain its frequency spectrum. In addition to the second harmonic (2f) signal we are detecting, there are also first, third, and higher-order harmonic signals present. These primarily result from the nonlinear modulation of the DFB laser. Therefore, the multiple frequencies we select should adhere to the following formula:

$$\begin{aligned} f_m - f_n &> \Delta f \\ f_m &\neq K \cdot f_n \end{aligned} \tag{4.1}$$

where $m \neq n$ and they are integers. f_m and f_n represent the multiple modulation frequencies we choose to use for different lasers. $K = 1, 2, 3, ...$ and Δf is the detection bandwidth.

By carefully considering these factors and selecting appropriate frequencies, we can mitigate interference and optimize the performance of our FDM-based gas detection system.

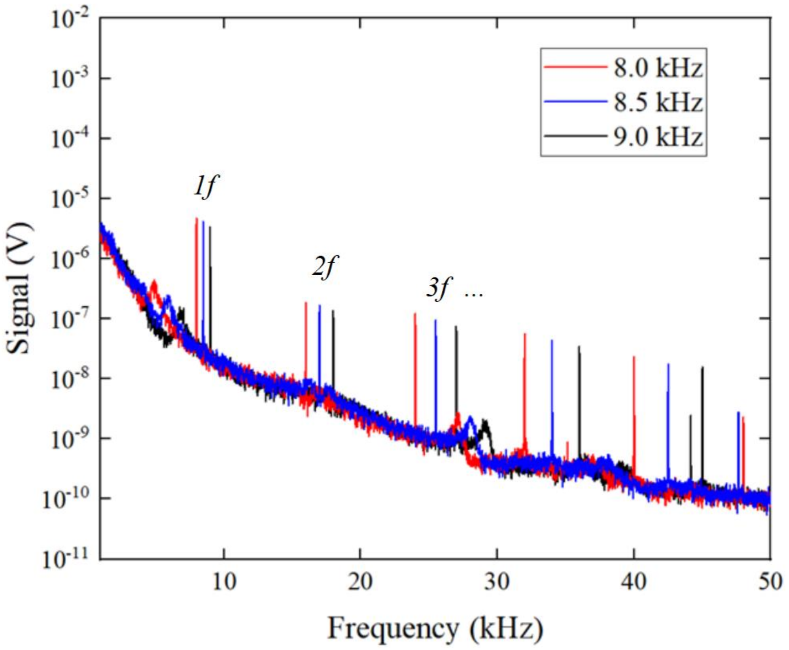

Figure 4.14 The frequency spectrum of PD signal for different modulation frequency.

4.6 Conclusion of multi-gas detection

In summary, we have reported a multi-component gas sensor based on the HCF PTS with FDM. The HCF supports broadband low-loss transmission, which enables simultaneous detection of multiple gases by using multiple pumps with wavelengths corresponding to the gas absorptions from NIR to MIR. A single HCF gas cell is used for light-gas interaction and a common telecom-band fiber-optic probe interferometer is used for phase detection, which enables a simple and compact system for practical field applications. With a 13-cm-long HCF gas cell, three pump lasers with wavelengths of 1392 nm, 2003 nm, and 4600 nm, and a probe interferometer operating at 1550 nm, we demonstrate simultaneous detection of CO, CO_2, and H_2O with LODs of 9 ppb, 25 ppb, and 2.7 ppm, respectively, with 1 s TC. The LODs go down to 0.6 ppb, 1.5 ppb, and 222 ppb with 1000 s averaging time. The system instability is better than 1.7% for the three gases over a period of 2 hours. The same system configuration may be employed for simultaneous detection of many other gases with absorption from ultra-violet to MIR, by simply using a HCF with suitable transmission bands, avoiding using multiple photodetectors.

4.7 Reference

1. G. A. WATCH, "WMO Global Atmosphere Watch (GAW) Strategic Plan: 2008–2015," (2011).
2. L. Menzel, A. Kosterev, R. Curl, F. Tittel, C. Gmachl, F. Capasso, D. Sivco, J. Baillargeon, A. Hutchinson, and A. Cho, "Spectroscopic detection of biological NO with a quantum cascade laser," Applied Physics B **72**, 859-863 (2001).
3. D. B. Malpass, *Introduction to industrial polyethylene: properties, catalysts, and processes* (John Wiley & Sons, 2010).
4. S.-Q. Wu, J.-i. Morishita, H. Masusaki, and T. Kimishima, "Quantitative analysis of trace moisture in N2 and NH3 gases with dual-cell near-infrared diode laser absorption spectroscopy," Analytical chemistry **70**, 3315-3321 (1998).
5. M. Dong, C. Zheng, S. Miao, Y. Zhang, Q. Du, Y. Wang, and F. K. Tittel, "Development and Measurements of a Mid-Infrared Multi-Gas Sensor System for CO, CO(2) and CH(4) Detection," Sensors (Basel) **17** (2017).
6. J. Jiang, Z. Wang, X. Han, C. Zhang, G. Ma, C. Li, and Y. Luo, "Multi-gas detection in power transformer oil based on tunable diode laser absorption spectrum," IEEE Transactions on Dielectrics and Electrical Insulation **26**, 153-161 (2019).
7. K. Chen, S. Liu, B. Zhang, Z. Gong, Y. Chen, M. Zhang, H. Deng, M. Guo, F. Ma, and F. Zhu, "Highly sensitive photoacoustic multi-gas analyzer combined with mid-infrared broadband source and near-infrared laser," Optics and Lasers in Engineering **124**, 105844 (2020).
8. F. Liu, H. Bao, H. L. Ho, W. Jin, S. Gao, and Y. Wang, "Multicomponent trace gas detection with hollow-core fiber photothermal interferometry and time-division multiplexing," Optics Express **29**, 43445-43453 (2021).
9. F. Chen, S. Jiang, W. Jin, H. Bao, H. L. Ho, C. Wang, and S. Gao, "Ethane detection with mid-infrared hollow-core fiber photothermal spectroscopy," Optics Express **28**, 38115-38126 (2020).
10. D. R. Lide, *CRC handbook of chemistry and physics* (CRC press, 2004).
11. H. Bao, Y. Hong, W. Jin, H. L. Ho, C. Wang, S. Gao, Y. Wang, and P. Wang, "Modeling and performance evaluation of in-line Fabry-Perot photothermal gas sensors with hollow-core optical fibers," Optics express **28**, 5423-5435 (2020).
12. W. J. Hooker, and R. C. Millikan, "Shock-Tube Study of Vibrational Relaxation in Carbon Monoxide for the Fundamental and First Overtone," The Journal of Chemical Physics **38**, 214-220 (1963).
13. J. w. L. Lewis, and K. P. Lee, "Vibrational Relaxation in Carbon Dioxide/Water-Vapor Mixtures," The Journal of the Acoustical Society of America **38**, 813-816 (1965).
14. C. Yao, Q. Wang, Y. Lin, W. Jin, L. Xiao, S. Gao, Y. Wang, P. Wang, and W. Ren, "Photothermal CO detection in a hollow-core negative curvature fiber," Optics letters **44**, 4048-4051 (2019).
15. Y. L. Hoo, S. Liu, H. L. Ho, and W. Jin, "Fast Response Microstructured Optical Fiber Methane Sensor With Multiple Side-Openings," IEEE Photonics Technology Letters **22**, 296-298 (2010).
16. W. Ren, W. Jiang, and F. K. Tittel, "Single-QCL-based absorption sensor for simultaneous trace-gas detection of CH4 and N2O," Applied Physics B **117**, 245-251 (2014).
17. N. Liu, L. Xu, S. Zhou, L. Zhang, and J. Li, "Simultaneous detection of multiple atmospheric components using an NIR and MIR laser hybrid gas sensing system," ACS sensors **5**, 3607-3616 (2020).
18. X. Yin, M. Gao, R. Miao, L. Zhang, X. Zhang, L. Liu, X. Shao, and F. K. Tittel, "Near-infrared laser photoacoustic gas sensor for simultaneous detection of CO and H2S," Optics Express **29**, 34258-34268 (2021).

19. X. Chen, H. Liu, M. Hu, Z. Xu, H. Deng, X. Fan, and R. Kan, "QEPAS sensor for simultaneously sensitive detection of NH3 and H2S based on frequency-division multiplexing," in *Eighth Symposium on Novel Photoelectronic Detection Technology and Applications*(SPIE2022), pp. 1888-1895.

Chapter 5

5 PTS with MIR pump and NIR probe using a reflective HCF DMI

In our quest to enhance detection sensitivity, one strategy is to diminish the noise. In this chapter, we demonstrate novel configuration, namely a reflective dual-mode interferometer (DMI), to detect the variation of the mode phase difference (MPD) between two guided modes in a gas-filled HCF. The unique advantage of this configuration is that the MPD is quite sensitive to gas absorption in the hollow-core, but impressively resilience to external disturbances. This symbiosis significantly boosts the SNR. The reflective configuration makes it possible delivery pump and probe beams from opposite ends of the HCF, allowing the use of a MIR pump to access the strong absorption lines and a NIR probe to detect the photothermal phase modulation with high sensitivity and cost effectiveness. Importantly, the DMI also exhibits insensitivity to laser phase noise due to small optical path difference, which allows us to leverage longer optical fibers to elevate system detection sensitivity. When compared with a FPI of the same length, the DMI has lower optical noise and is more stable.

5.1 Basics of DMI

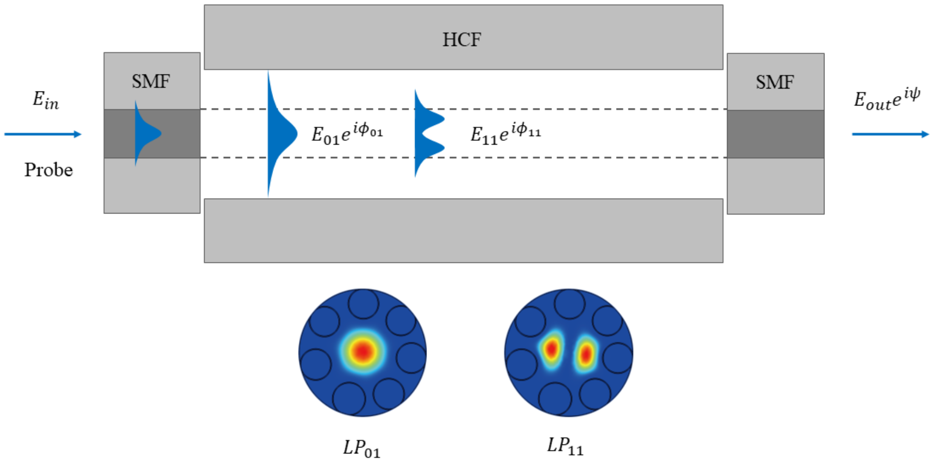

Figure 5.1 Diagram of the excited LP$_{01}$ and LP$_{11}$ modes within the dual-mode HCF

The principle of the DMI may be explained through Fig. 5.1. The DMI consists of two sections of SMFs and one dual-mode HCF which excites LP_{01}-like and LP_{11} modes simultaneously within the hollow core. The two modes combine at the output SMF and the combined electric field and the output intensity may be expressed as:

$$E_{out}exp(\omega t - j\psi) = E_{01}exp(\omega t - j\phi_{01}) + E_{11}exp(\omega t - j\phi_{11}) \tag{5.1}$$

$$\begin{aligned} I_{out} &= c\varepsilon_0 \left\langle \left|E_{out}(t)\right|^2 \right\rangle = I_{01} + I_{11} + 2\sqrt{I_{01}I_{11}}cos(\phi_{01} - \phi_{11}) \\ &= I_{01} + I_{11} + 2\sqrt{I_{01}I_{11}}cos(\Delta\phi_L + \Delta\phi_S) \end{aligned} \tag{5.2}$$

where E_{out} and ψ are the amplitude and phase of the combined optical field, E_{01} and E_{11} are the amplitudes while ϕ_{01} and ϕ_{11} are the phases of the LP_{01} and LP_{11} modes, respectively, and ω is the angular optical frequency. $\Delta\phi_L = 2\pi \cdot \Delta nL / \lambda_{probe}$ is the intrinsic MPD and the $\Delta n = n_{01} - n_{11}$ is the RI difference. $\Delta\phi_S$ is the MPD resulting from photothermal effect due to gas absorption, which may be expressed as [1]:

$$\Delta\phi_S = \phi_{S,01} - \phi_{S,11} = k^*(\eta_m, f)\alpha(\lambda_{pump})CLP_{pump} \tag{5.3}$$

where $\phi_{S,\mathrm{i}}$ (i = 01 or 11) represents PT phase modulation for LP_{01} or LP_{11} mode of the probe, η_m the fractional pump power in the LP_{01} mode and f the pump modulation frequency. The differential phase modulation coefficient $k*$ is a function of η_m and f.

5.2 Methane detection with DMI

Sensitive and accurate methane detection is crucial for environmental surveillance, breath analysis, and industrial processes [2, 3]. HCF laser spectroscopy, due to its superior light-gas interaction capability, has been demonstrated as an effective method for trace gas detection. With this approach, methane detection at levels as low as tens of ppb has been achieved in the MIR band.

Methane's absorption coefficient in the MIR band is significantly higher than in the NIR. Consequently, a system using a MIR pump and a NIR probe has demonstrated high sensitivity in gas detection with HCF PTS. Despite this, the sensitivity is restricted by the probe laser's phase noise due to the inherent optical path difference (OPD) of the FPI structure. Hybrid fiber and free-space MZI have been explored for PTS gas detection, but their implementation is more complex and expensive, and the usage of bulky free-space components compromises long-term system stability.[4, 5]

Here we take methane detection as an example to demonstrate the effectiveness of the reflective HCF DMI. The reflective MPD interferometry suppresses common-mode noise effectively and the light-gas interaction length is twice that of a single-pass gas cell. The reflective configuration enables the NIR probe to get into and out of the HCF gas cell at the same end and hence enables the usage of a simple and cost-effective all-fiber phase detection system at 1.55 μm without the use of a NIR/MIR combiner. The MIR pump at 3.27 μm is delivered into the HCF from the opposite end through a wedged window.

5.3 Design of the reflective gas cell

Fig. 5.2 shows the calculated absorption coefficient of 0.1% water vapor and 2 ppm methane using the HITRAN database at 1 atm and 296 K. At 3058 cm^{-1} (3270 nm), the absorption coefficient and linewidth of 2 ppm methane is 9.8×10^{-5} cm^{-1} and 0.161 cm^{-1}, respectively. In our experiment, the dry standard methane sample balanced by nitrogen is used to avoid the influence of the water vapor.

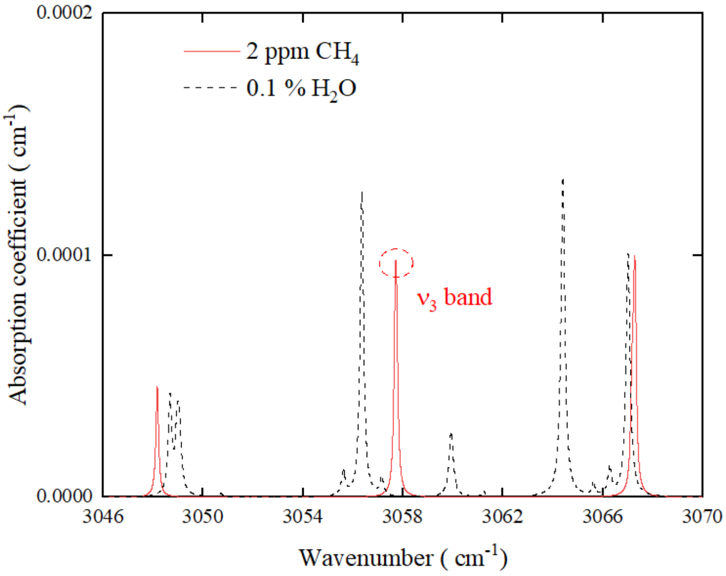

Figure 5.2 HITRAN-based absorption coefficient of 0.1% H_2O and 2 ppm CH_4 from 3046 cm^{-1} to 3070 cm^{-1}.

The schematic of the HCF gas cell is shown in Fig. 5.3(a). It is constructed with a thermally expanded core fiber (TECF), a coated wedge window and a 1.8-m-long AR-HCF. This HCF consists of six untouched silica tubes encircling an air core with a diameter of 65 μm [6]. It supports two low-loss core modes (LP_{01} and LP_{11}) with broadband transmission from 1.4 µm to 4.7 µm. On the pump side, the collimated beam at 3.27 µm is coupled into the HCF by a single lens with a focal length of 20 mm through the window. The transmissions for both window and lens are about 90% at 3.27 µm. On the probe side, the TECF made from standard single mode fiber (SMF) is 8° angle cleaved to avoid reflection and the expanded core can reduce the coupling loss at the SMF/HCF joint. The relative position of the AR-HCF and the TECF is adjusted by a 5-axis stage to excite the LP_{01} and LP_{11} modes simultaneously. Both modes propagate through the HCF and are then reflected by the coated window with reflectivity of about 60% at 1.53 µm. The relative position of the HCF and the window should also be carefully adjusted to avoid coupling between different modes at the reflecting surface. Then, the reflected light is coupled back into the TECF at the SMF/HCF joint. This forms an in-fiber reflective DMI for phase detection. The reflected spectrum, measured with a broadband light source and an optical spectrum analyzer, is shown in Fig. 5.3(b). The calculated effective RI difference between the LP_{01} and LP_{11} modes is 4×10^{-4}. And the calculated OPD between two modes for double-passing the 1.8-m-long AR-HCF is about 1.44 mm, corresponding to a free spectral range (FSR) of 1.61 nm, which is closed to the measured FSR of 1.44 nm.

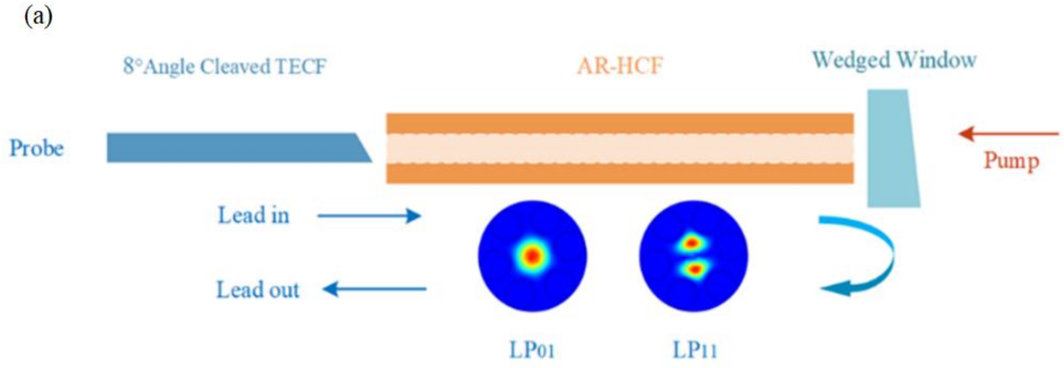

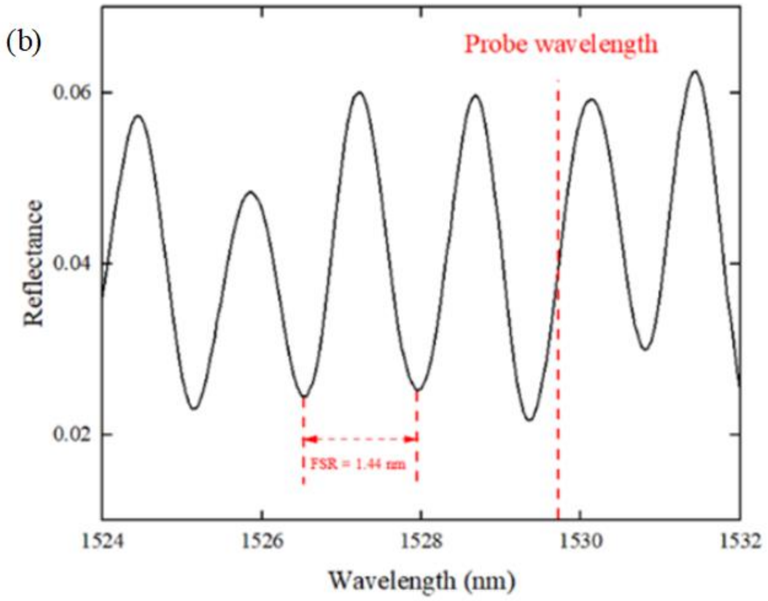

Figure 5.3(a) Schematic of the AR-HCF gas cell showing the dual-mode interferometer for the probe. (b) The measured reflected dual-mode interference fringe from 1524 nm to 1532 nm.

5.4 Setup for methane detection

The experimental set-up is shown in Fig. 5.4. An inter-band cascade laser (ICL) at 3270 nm is used as the pump source and the effective pump power is measured at the output end of the AR-HCF with a thermopile power meter and is about 2.7 mW. The ICL is sinusoidally modulated at 7 kHz via a current controller with a modulation depth of 0.37 cm^{-1}, which coincides well with 2.2 times the linewidth. At the same time, the wavelength of the ICL is scanned via a temperature controller at 10 mHz.

We use an external-cavity diode laser (ECDL) as the probe source and its wavelength is tuned to the quadrature point of the dual-mode interferometer around 1530 nm as indicated in Fig. 5.3(b). The reflected optical power is about 400 μW and a balanced detector (BPD) is used to suppress intensity noise. The signal is demodulated by a lock-in amplifier.

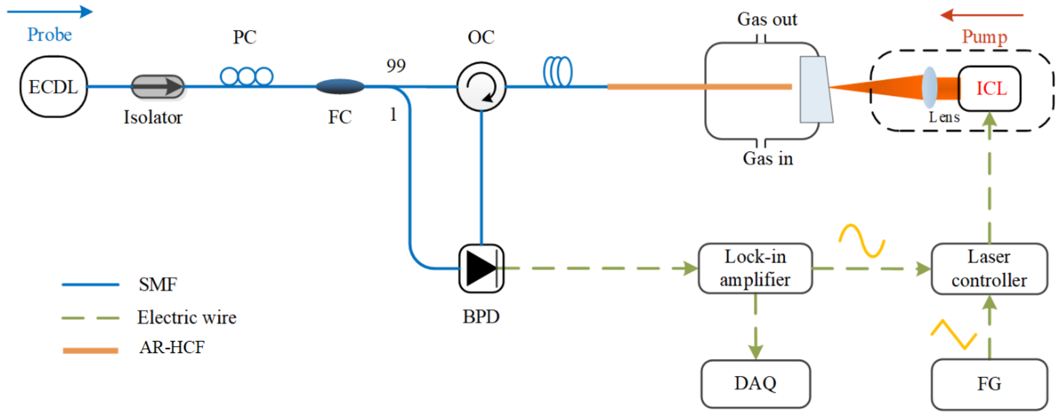

Figure 5.4 Experiment set-up. DAQ, data acquisition; ECDL, external-cavity diode laser; FC, fiber coupler; FG, function generator; ICL, inter-band cascade laser; OC, optical circulator; PC, polarization controller; BPD, balanced photodetector.

5.4.1 Experiment results

Methane detection experiment is conducted by pressuring gas into the 1.8-m-long AR-HCF with pressure level of ~2 bar at the pump input side of the gas cell while the probe side is open to atmospheric pressure. After completing the gas filling, the pressure in the gas cell is released to 1 bar at room temperature and then sealed. Fig. 5.5(a) shows the 2f signal with 2 ppm methane when the pump is scanned across the absorption line at 3270.42 nm. The inset in Fig. 5.5(a) shows the noise for two minutes when the gas cell is filled with pure N_2 and the pump laser is tuned away from the absorption line to avoid the influence of residual methane. The standard deviation (s. d.) of the noise is 0.58 μV, giving a SNR of ~ 4880. The calculated LOD is 410 ppt for an SNR of unity, with 1 s lock-in time constant. Allan deviation analysis was conducted with the baseline noise recorded over a period of 40 minutes with the lock-in constant of 100 ms, the result is shown in Fig. 5.5(b). The LOD goes down to 129 ppt with 100 s averaging time and 44 ppt with 800 s averaging time.

The system stability was tested by repeatedly scanning the pump wavelength across the absorption line of methane when pressuring 2 ppm methane into the HCF with pressure level of 1.2 bar for 1 hour. The peak-to-peak value of the 2f signal varies ~ 1.8 % for 1 hour as shown in Fig 5.5(c).

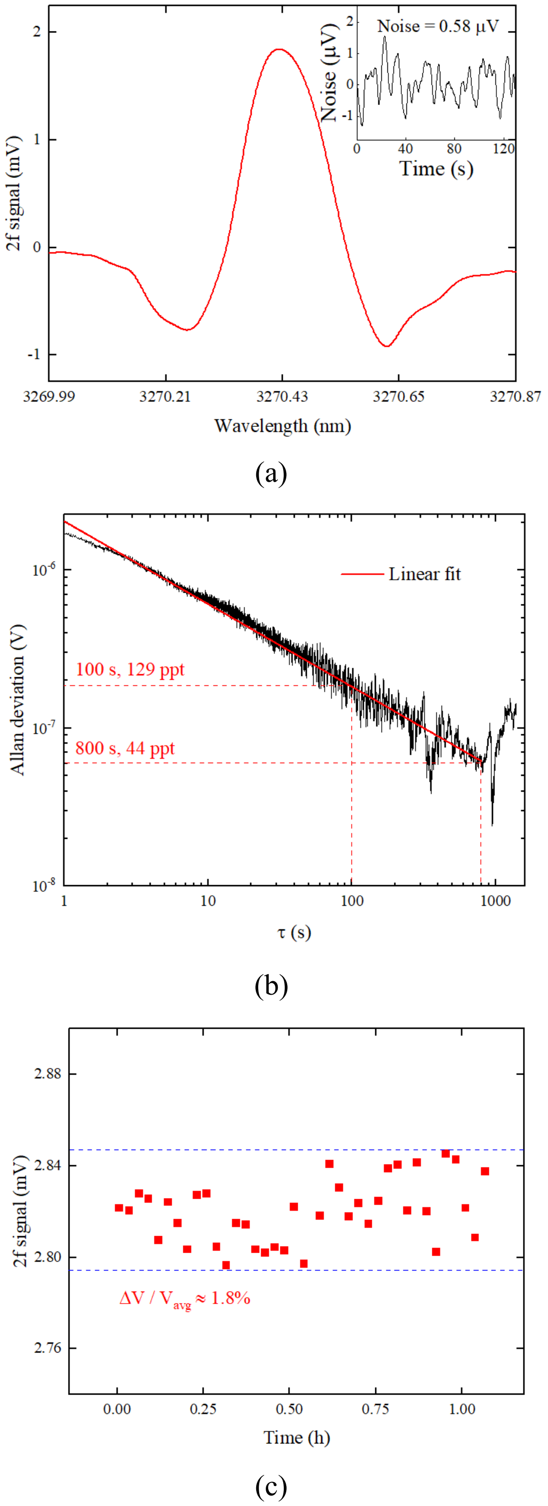

Figure 5.5 (a) 2f lock-in output signal as a function of pump wavelength for 2 ppm methane in nitrogen. The inset is the 2f signal when the gas cell was filled with pure nitrogen and the pump laser was tuned away from 3270.42 nm. The lock-in time constant used is 1 s, which corresponds to a detection bandwidth of 0.094 Hz. (b) Allan deviation analysis of the baseline noise over a period of 40 minutes. The lock-in time constant used is 100 ms. (c) Variation of the peak-to-peak value of the 2f signal over 1 hour.

Table 5.1 summarizes the performances of the recently reported MIR HCF-based gas sensors. The NEA is given here for a fair comparison, which is independent of gas type and absorption strength. The current work achieves a NEA of 2.16×10^{-9} cm^{-1} for 800 s integration time, which is about one order of magnitude better than the state-of-the-art MIR HCF gas sensor [7].

Compared with FPI PTS[8], the improved sensitivity is mainly due to the longer length of sensing HCF but shorter OPD between the two modes, which minimizes the phase noise effectively. And the reflective structure of our sensor enables NIR probe to be launched into and collected from one end of the HCF while the MIR pump delivered into the HCF from the other end. This structure enables the usage of a simple and cost-effective all-fiber probe system, instead of using the complex NIR/MIR free-space optics. Besides, the DMI contributes to better system stability due to the insensitivity to external perturbations [1].

Table 5.1 Performances of recently reported MIR HCF-based gas sensors.

Technique	Wavelength (nm)	Pump power (mW)	HCF Length (m)	NEA (cm^{-1})	Integration time (s)
PTI-MZI heterodyne [9]	3.60	1.40	1.20	7.00×10^{-7}	Not stated
TDLAS [10]	3.60	N/A	1.20	2.50×10^{-7}	40s
PTI-FPI [8]	3.34	1.50	0.14	1.43×10^{-7}	410s
PTI-MZI heterodyne[11]	5.26	82.0	0.25	2.81×10^{-8}	100s
DAS-WMS [7]	3.34	N/A	30.0	1.50×10^{-8}	14 s
PTI-MPD (This work)	3.27	2.70	1.80	2.01×10^{-8} 2.16×10^{-9}	1s 800s

N/A: not applicable.

5.5 Discussion

5.5.1 Noise analysis

In chapter 2, we have conducted the noise analysis for FPI PTS. And the same for the reflective DMI, the system noise mainly comprises electrical noise and optical noise, where the latter can be further divided into shot noise, intensity noise, and phase noise. We stimulate these noises for lasers with different linewidth and different HCF length. In our stimulation, the received power in PD is 400 µW, which is the data used in our experiments. The RIN is 140 dBc/Hz for the common lasers. The RI difference is 4×10^{-4}. According to Equation 3.5 to 3.9, The noise level is shown in following figures.

For high-performance lasers with a relatively narrow linewidth, such as a 2 kHz linewidth fiber laser, the system's phase noise is significantly lower compared to intensity noise and shot noise. Therefore, as depicted in Fig. 5.6, increasing the length of the HCF does not increase the overall noise level of the system. This aligns with the current state of our system. Thus, we can further increase the HCF length to improve the SNR. Additionally, using a BPD can reduce intensity noise and bring our system closer to the shot-noise limit.

Furthermore, we simulated the noise characteristics of commonly used DFB lasers with a linewidth of ~10 MHz. As shown in Fig. 5.7, phase noise becomes the primary source of system noise for HCF length of longer than 3 m. This indicates that with a regular DFB laser, the limitation of the DMI length is around 3 m.

In our experiment, we utilized a sensing HCF with a length of 1.8 m. We simulated the impact of lasers with different linewidth on the system noise. As shown in Fig. 5.8, even when a kHz-level linewidth probe laser is replaced by a 10 MHz linewidth laser, the overall system noise only increases slightly. Therefore, for practical application, we can save costs on the probe laser without a significant impact on the system's sensing ability.

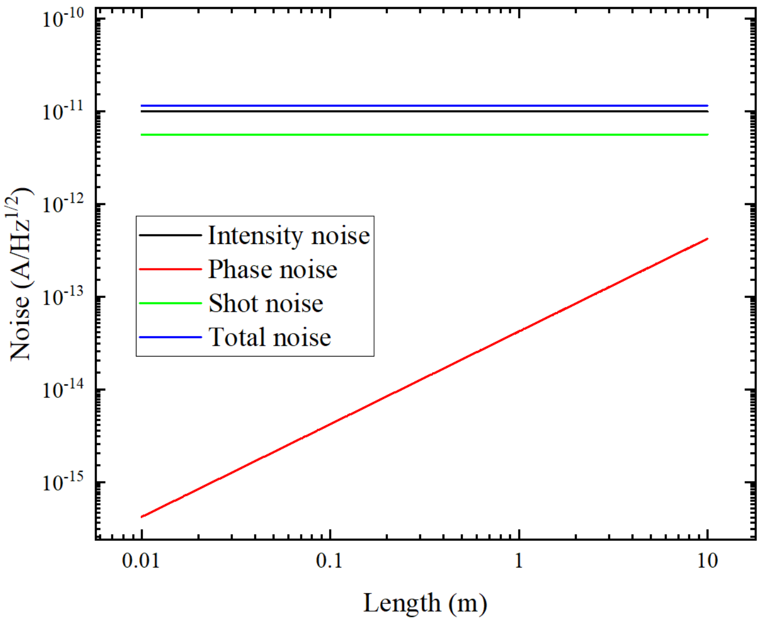

Figure 5.6 The relationship between noise and DMI length for a laser with 2 kHz linewidth

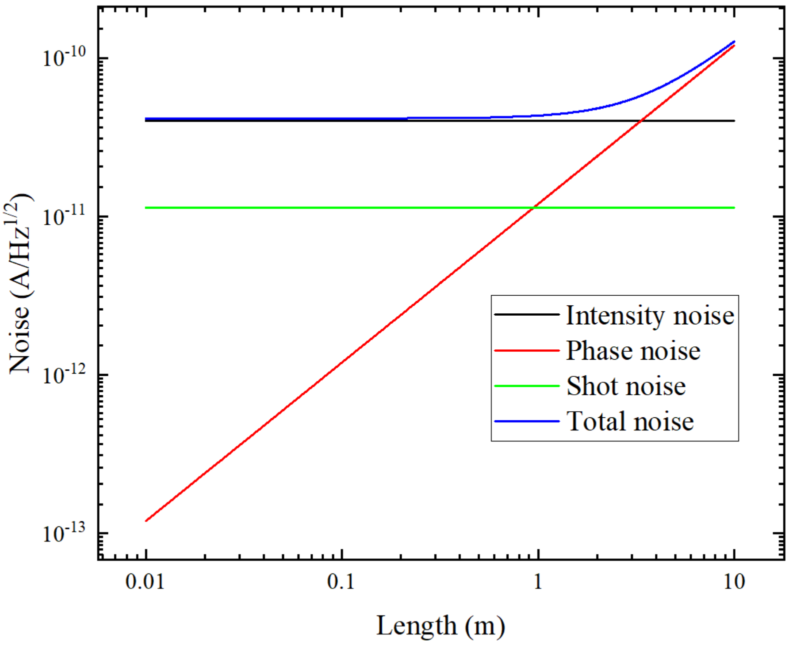

Figure 5.7 The relationship between noise and DMI length for a laser with 10 MHz linewidth

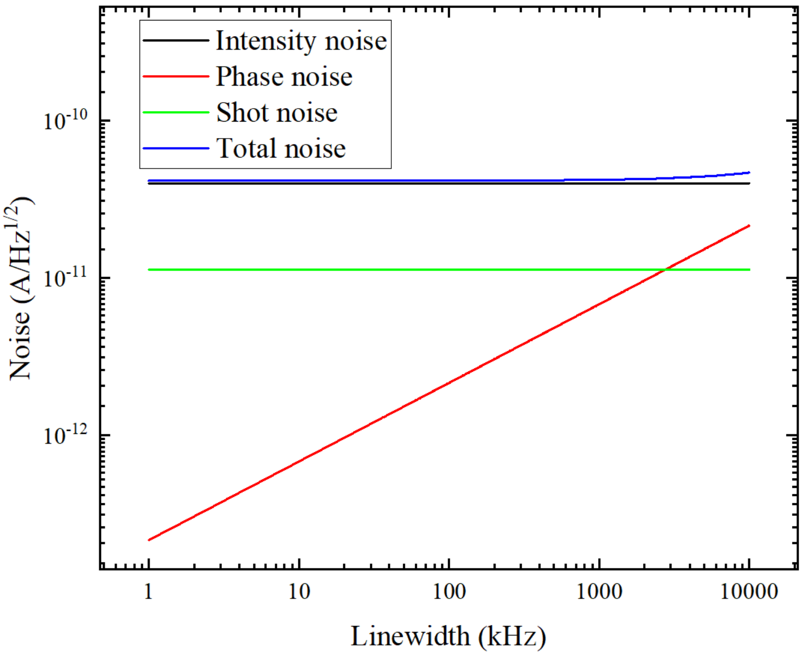

Figure 5.8 The relationship between noise and laser linewidth for 1.8 m HCF

5.5.2 The stability analysis

The DMI utilizes two modes for sensing when the other common interferometers, e.g., FPI, mainly utilize the fundamental mode. First, we consider sensitivity to temperature perturbation.

To accurately simulate this, it is necessary to consider two effects while disregarding the elastic-optic effect caused by thermal expansion [12]. The first effect pertains to changes in the material's refractive index (RI) resulting from temperature fluctuations, known as the thermo-optic effect. The second effect involves the longitudinal and transverse thermal expansion. To illustrate, we can take the example of the LP01 mode's phase sensitivity to temperature [13]:

$$S_{01,X} = \frac{\Delta\phi_{01}}{\Delta X} = \frac{2\pi n_{01} L}{\lambda_{probe}} \left(\frac{1}{n_{01}} \frac{\partial n_{01}}{\partial X} + \frac{1}{L} \frac{\partial L}{\partial X} \right) \tag{5.4}$$

where X refers to T (or P which will be discussed later). The right-hand side (RHS) of the equation includes two terms that explain the effects mentioned earlier. The first term considers the change in the effective RI caused by transverse thermal expansion and the thermo-optic effect. The second term on the RHS accounts for the longitudinal expansion of the fiber.

The external pressure applied to the fiber causes compression, leading to longitudinal elongation and transverse deformation. To calculate the phase sensitivity to external pressure *P*, Eq. (5.4) was employed, with the variable "X" representing pressure. The first and second terms on the RHS are referred to as the changes in the effective RI induced by transverse deformation and longitudinal elongation, respectively. The Equation 5.4 is also applied to determine the sensitivity of the MPD to external perturbations [1]:

$$S_{MPD,X} = \frac{\Delta\phi_{01} - \Delta\phi_{11}}{\Delta X} = \frac{2\pi\Delta n L}{\lambda_{probe}}\left(\frac{1}{\Delta n}\frac{\partial \Delta n}{\partial X} + \frac{1}{L}\frac{\partial L}{\partial X}\right) \tag{5.5}$$

The sensitivity ratio $\varsigma = S_{01,X} / S_{MPD,X}$ is on the order of $n_{01} / \Delta n$, indicating that the MPD is much less sensitive to external perturbation than the fundamental mode phase. In the ref. [1], the LP_{01} mode phase is ~ 280 times and ~170 times more sensitive to the external *T* and *P* disturbances than the MPD, respectively.

5.6 Conclusion of reflective MPD MIR PTS

In summary, we have demonstrated a highly sensitive MIR methane sensor based on the reflective MPD PTS in an HCF. With a double-pass 1.8-m-long AR-HCF gas cell and a 3270 nm ICL pump laser, we demonstrated methane detection of 44 ppt with 800 s integration time, corresponding to a NEA of 2.16×10^{-9} cm^{-1}. And this is the smallest NEA among the MIR HCF-based gas sensors reported so far to our knowledge. The stability over 1 hour is about 1.8 %. The high sensitivity and good stability of this methane sensor are promising for field applications.

5.7 Reference

1. P. Zhao, Y. Zhao, H. Bao, H. L. Ho, W. Jin, S. Fan, S. Gao, Y. Wang, and P. Wang, "Mode-phase-difference photothermal spectroscopy for gas detection with an anti-resonant hollow-core optical fiber," Nature communications **11**, 1-8 (2020).
2. B. de Lacy Costello, M. Ledochowski, and N. M. Ratcliffe, "The importance of methane breath testing: a review," Journal of breath research **7**, 024001 (2013).

3. S.-Y. Lee, and G. D. Holder, "Methane hydrates potential as a future energy source," Fuel processing technology **71**, 181-186 (2001).
4. P. Jaworski, P. Kozioł, K. Krzempek, D. Wu, F. Yu, P. Bojęś, G. Dudzik, M. Liao, K. Abramski, and J. Knight, "Antiresonant Hollow-Core Fiber-Based Dual Gas Sensor for Detection of Methane and Carbon Dioxide in the Near- and Mid-Infrared Regions," Sensors **20**, 3813 (2020).
5. S.-H. Huang, Y.-J. Huang, and H.-C. Chui, "Trace methane sensor using mid-infrared light emitting diode in hollow-core fiber," Sensors and Actuators B: Chemical **282**, 599-602 (2019).
6. S. Gao, Y. Wang, and P. Wang, "Silica-based modeless hollow-core fiber for broadband mid-IR guidance," in *2017 Conference on Lasers and Electro-Optics Pacific Rim (CLEO-PR)*(IEEE2017), pp. 1-2.
7. P. Jaworski, K. Krzempek, P. Kozioł, D. Wu, F. Yu, P. Bojęś, G. Dudzik, M. Liao, J. Knight, and K. Abramski, "Sub parts-per-billion detection of ethane in a 30-meters long mid-IR Antiresonant Hollow-Core Fiber," Optics & Laser Technology **147**, 107638 (2022).
8. F. Chen, S. Jiang, W. Jin, H. Bao, H. L. Ho, C. Wang, and S. Gao, "Ethane detection with mid-infrared hollow-core fiber photothermal spectroscopy," Optics Express **28**, 38115-38126 (2020).
9. C. Yao, S. Gao, Y. Wang, W. Jin, and W. Ren, "Heterodyne interferometric photothermal spectroscopy for gas detection in a hollow-core fiber," Sensors and Actuators B: Chemical **346**, 130528 (2021).
10. C. Yao, S. Gao, Y. Wang, P. Wang, W. Jin, and W. Ren, "Silica hollow-core negative curvature fibers enable ultrasensitive mid-infrared absorption spectroscopy," Journal of Lightwave Technology **38**, 2067-2072 (2019).
11. K. Krzempek, "Part-per-billion level photothermal nitric oxide detection at 5.26 µm using antiresonant hollow-core fiber-based heterodyne interferometry," Optics Express **29**, 32568-32579 (2021).
12. E. N. Fokoua, M. N. Petrovich, T. Bradley, F. Poletti, D. J. Richardson, and R. Slavík, "How to make the propagation time through an optical fiber fully insensitive to temperature variations," Optica **4**, 659-668 (2017).
13. V. Dangui, H. K. Kim, M. J. Digonnet, and G. S. Kino, "Phase sensitivity to temperature of the fundamental mode in air-guiding photonic-bandgap fibers," Optics Express **13**, 6669-6684 (2005).

Chapter 6

6 Cavity-enhanced stimulated Raman gain spectroscopy in HCFs

Stimulated Raman gain (SRG) spectroscopy stands out as an efficacious branch of coherent Raman spectroscopy. One of its distinguishing features is that the Raman gain signal detected correlates directly to the concentration of the gas, making it an expedient tool for a broad spectrum of measurements.

When utilizing a continuous wave (CW) pump source, SRG measurements have been able to effectuate a considerable suppression of background signals. Remarkably, this results in detection limits that rival or even outperform those achieved through Coherent Anti-Stokes Raman Spectroscopy (CARS) [1].

In recent times, the integration of HC-PBFs has been shown to escalate the sensitivity of gas detection systems by two to three orders of magnitude. This significant improvement holds for both spontaneous and stimulated Raman scattering [2]. And hydrogen detection is very import and benefits from the HCF-enhanced SRG.

HC-PBFs, varying from 1 to 4.5 meters in length, have successfully accomplished detection limits of 10^2-10^3 parts per million (ppm) for gases like hydrogen, nitrogen, oxygen, and carbon dioxide under standard conditions [3, 4]. More impressively, under high-pressure conditions (for instance, 20 bar), a detection limit down to several ppm has been achieved. This feat was accomplished using a meter-long HC-PBF in conjunction with a 2W pump laser at 532 nm and a Roper Scientific spectrometer furnished with a liquid-nitrogen-cooled CCD [5]. Nonetheless, these techniques necessitate high-power lasers and complex detectors, which, unfortunately, makes them unsuitable for practical applications.

Our group recently conducted a study on a hydrogen detection system based on all-fiber technology, utilizing a HC-PBF. The experimental setup, depicted in Fig. 6.1, involved the use of two lasers: a pump laser operating around 1532 nm and a probe (Stokes) laser operating around 1620 nm. By coupling approximately 40 mW of pump laser power into a 15-meter-long HC-PBF and assuming a 1 s TC, we achieved a LOD of approximately 140 ppm for hydrogen detection.[6].

The performance of this system is mainly influenced by two factors: fluctuations in laser intensity and residual mode interference in the HC-PBF. These limitations arise due to the inherent nature of HC-PBFs, which, despite being advanced, still support a few high-order modes and cannot be considered purely single-mode fibers.[6].

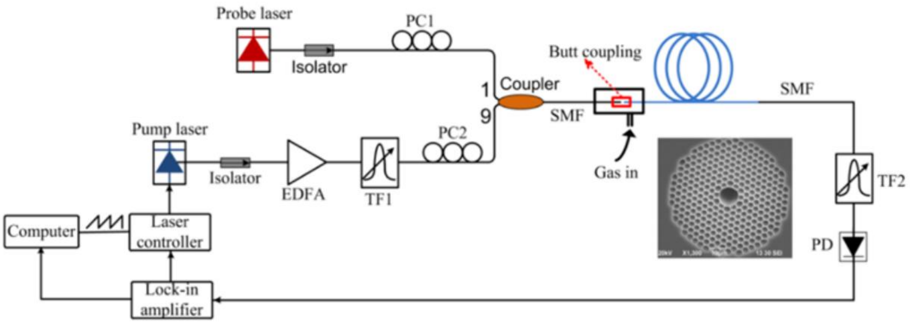

Figure 6.1 The experimental setup for all-fiber hydrogen detection based on SRG.[6]

6.1 Principle of stimulated Raman gain spectroscopy

Stimulated Raman scattering is a complex process which involves the interaction between a pump photon, a Stokes photon that's downshifted in frequency, and a specific vibrational or rotational state of molecules. This can be initiated by propagating two beams, referred to as the pump and the probe, through a specific medium, such that the difference in their frequencies matches the transition frequency of a vibrational or rotational movement of the molecules in the medium. When this occurs, the probe beam's intensity shows an increase - this is known as SRG, and the pump beam's intensity shows a decrease - referred to as stimulated Raman loss (SRL). This technique of detection, involving both a pump and a probe, is commonly known as 'seeded SRS.' Typically, the SRL of the pump beam is so minor that it can be disregarded. Thus, we often refer to the steady-state Raman gain equation. This is predicated on the assumption that the SRG is significantly smaller than 1 (ΔI_S is much smaller than I_S) [7]:

$$\Delta I_s / I_s = g_R I_P L \tag{6.1}$$

SRG of Stokes light can be employed to calculate SRG coefficient, and consequently, it can be used to estimate the concentration of gas sample. Special emphasis should be given to the Raman gain factor (g_R), which is inversely proportional to the Raman linewidth. This factor can be represented as a function of the concentration of gas sample, the Raman linewidth (γ), and two types of linewidth broadening: air-broadening (γ_{air}) and self-broadening (γ_{self}).

$$\begin{gathered} g_R \propto C/\gamma \\ \gamma = \gamma_{air}(1-C) + \gamma_{self} C \end{gathered} \tag{6.2}$$

In the context of gas tracing applications, when the concentration C is significantly small compared to 1 (C << 1), the Equation 6.2 can be simplified to 6.3.

$$g_R \propto C/\gamma_{air} \tag{6.3}$$

Take the $Q_1(1)$ transition of hydrogen as an example. As calculated in chapter 2, when the Stokes light is at 1550 nm, its Raman gain, for the case that the pump light and the Stokes light are linearly polarized and have parallel directions, is 0.153 cm/GW at 1 atm and it increases to 0.975 cm/GW at 10 atm. When the linear polarization directions of the two beams of light are perpendicular, the Raman gain is 0.0037 cm/GW at 1 atm and 0.019 cm/GW at 10 atm.

6.2 Fabry-Perot cavity

Cavity-enhanced stimulated Raman gain spectroscopy (CE-SRGS) is a technique that improves the sensitivity of traditional SRG by using an optical cavity, typically a FPI, to increase the interaction of light with the sample.

In SRGS, light interacts with a sample and causes vibrations in the molecules, leading to a shift in the wavelength of the light, which can be measured to gain information about the sample. However, only a small fraction of the photons is shifted, making Raman signals inherently weak and limiting the sensitivity of the technique.

The idea behind CE-SRGS is to increase the length of interactions between the light and the sample. This is done by placing the sample inside an optical cavity formed by two mirrors, which causes the light to bounce back and forth many times before it exits the cavity. Each time the light passes through the sample, there is a chance for a Raman interaction to occur. This effectively increases the path length of the light through the sample, leading to a significant enhancement of the Raman signal.

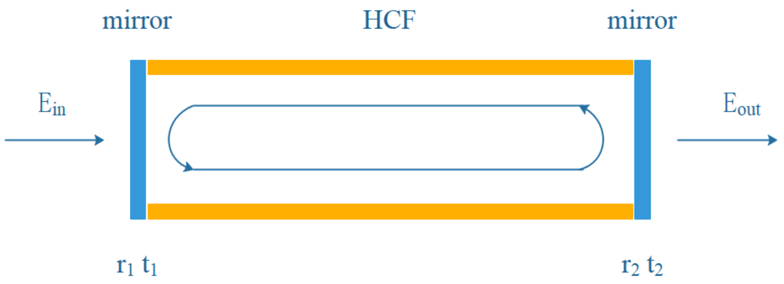

Figure 6.2 HCF FP cavity.

The Fig. 6.2 shows a HCF FP cavity, which is an optical setup composed of two mirrors facing each other along an optical HCF, separated by distance L. Assume that a monochromatic light field with a Gaussian profile, $E_0(z)$ enter the cavity [8].

$$E_{in}(z,t) = E_0(z)e^{i(\omega t - kz)} \tag{6.4}$$

$$\begin{aligned} E_{out} &= E_0(z)\sum_{p=0}^{\infty} t^2 r^{2p} e^{i\omega(t-2pL_c/c-L_c/c)-ikz} \\ &= \frac{t^2 e^{-i\omega L_c/c}}{1-r^2 e^{-i\omega t_r}} E_{in}(z,t), \end{aligned} \tag{6.5}$$

The field that is transmitted by the empty cavity, E_{out}, is given by considering all cavity round trips (where $z > L$, if we set the origin $z = 0$ at the cavity input) and shown in Equation 6.5. The transmission and reflection coefficients of the field for the two identical cavity mirrors are denoted by t, r respectively. The corresponding coefficients for the light intensity, T, R, are obtained by taking the square of these values. And the $t_r = 2n_{eff}L/c$ is the round-trip time, n_{eff} is the effective refractive index of the fundamental mode.

In a cavity with mirrors having different reflection and transmission properties (r_1, r_2 *and* t_1, t_2), the same formula still holds if we redefine r *and* t as $\sqrt{r_1 r_2}$ *and* $\sqrt{t_1 t_2}$ respectively.

The term $i\omega(t - 2pL/c - L/c)$ represents the phase change after one passage L/c and p round trips. The transmitted intensity (Equation 6.6), represented by the widely recognized Airy formula [8], is obtained by taking the absolute square value of this term, which yields a series of resonances uniformly spaced by the FSR as shown in Fig. 6.3.

$$I_{out}(\omega) = \frac{T^2}{\left|1-\mathrm{Re}^{-i\omega t_r}\right|^2} I_{in} = \frac{T^2}{(1-R)^2} \frac{I_{in}}{1+(\frac{2\sqrt{R}}{1-R})^2 \sin^2(\omega t_r/2)} \tag{6.6}$$

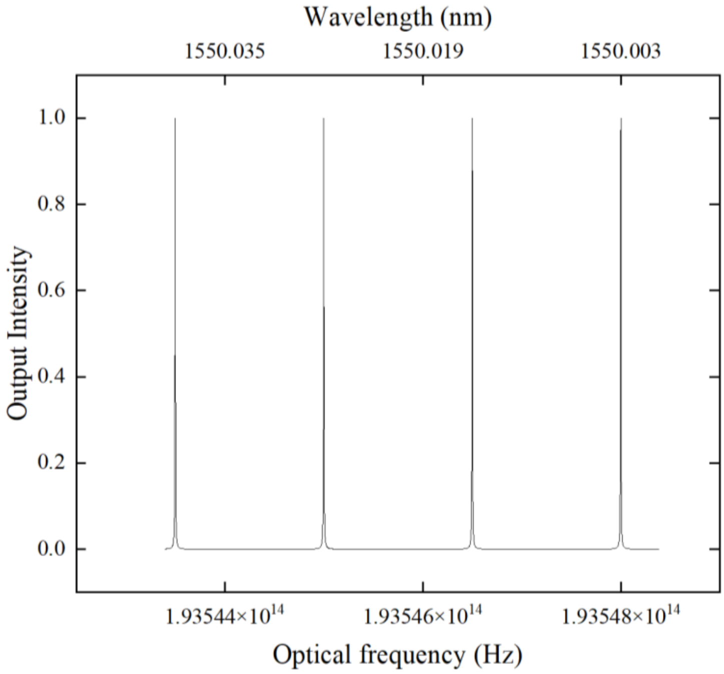

Figure 6.3 Simulated transmission spectrum around 1550 nm.

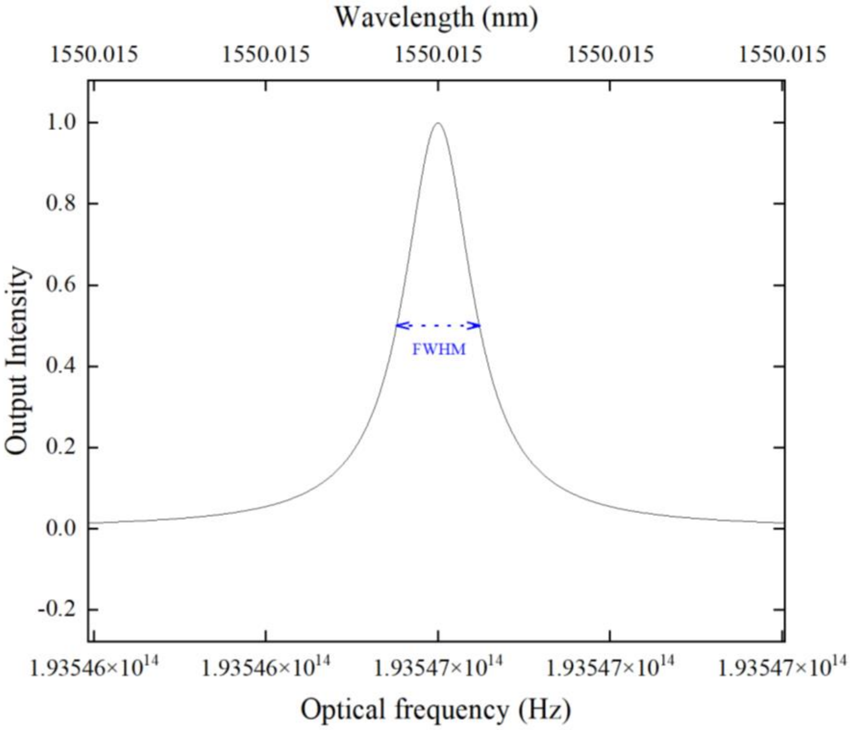

Figure 6.4 Simulated single resonance around 1550 nm

When evaluated around a resonant frequency, the transmitted intensity can be well approximated by a Lorentzian function. The FWHM of this resonance $\Delta\nu_c$, shown in Fig. 6.4, and the cavity finesse (F), are subsequently determined. The relationship between the *R* and *F* is shown in Fig. 6.5.

$$\begin{gathered}\Delta\nu_c = \frac{1}{\pi t_r}\frac{1-R}{\sqrt{R}} \\ F = FSR/\Delta\nu_c = \frac{\pi\sqrt{R}}{1-R}\end{gathered} \tag{6.7}$$

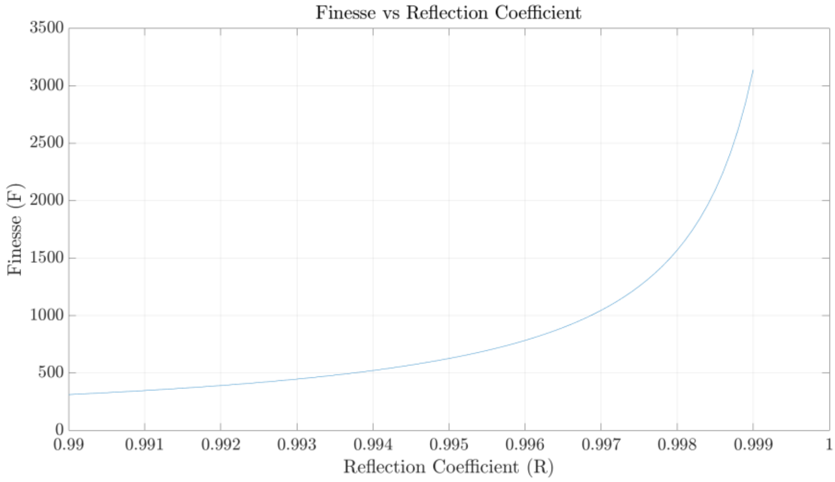

Figure 6.5 The relationship between finesse and reflection coefficient

6.3 Cavity enhanced factor for SRGS

To incorporate Raman gain $I_{out} = I_{in}(1+g_R I_p L)$ into the previous analysis, we can introduce the enhancement of the field due to the Raman effect for each passage through the cavity. During each passage through the cavity, the light traverses the sample once and is reflected by a mirror. In this context, we can associate the intra-cavity gain factor with the mirror's reflection coefficient. Furthermore, for accuracy, we need to account for the fact that the incoming light, which is directly transmitted by both mirrors during the first passage through the cavity, experiences intra-cavity gains along the cavity length. This introduces a global multiplicative factor of $1+g_R I_p L$. Considering these considerations, there is no need to repeat the previous derivation. Instead, we can directly apply these substitutions to incorporate the effects mentioned earlier:

$$\begin{aligned} r &\Rightarrow r\sqrt{1+g_R I_p L} \\ t^2 &\Rightarrow t^2\sqrt{1+g_R I_p L} \end{aligned} \tag{6.8}$$

From Equation 6.7, we can write the cavity transmission at resonance ω_0:

$$I_{out}(\omega_o) = I_{in}(\omega_o)\frac{T^2(1+g_R I_p L_c)}{[1-R(1+g_R I_p L_c)]^2} \tag{6.9}$$

One obtains to first order of Taylor series in g_R :

$$\begin{aligned} I_{out} / I_{in} &\approx \frac{T^2}{(1-R)^2}(1+\frac{2}{1-R}g_R I_P L) \\ &\approx 1+g_R I_P L_{eff} \end{aligned} \tag{6.10}$$

where the effective optical length is $L_{eff} = \frac{2}{1-R}L_c \approx \frac{2F}{\pi}L$

Considering that the pump and Stokes light undergo both co- and counter-propagating paths within the cavity, it's essential to factor in both the co-phase and counter-phase Raman gain coefficients. Due to Doppler broadening, the Raman linewidth of the backward Stimulated Raman Scattering (SRS) tends to be larger [9]. As a result, we can determine that the overall enhancement effect, denoted by $G = F / \pi$.

6.4 Preparation of HCF cavity and gas cell

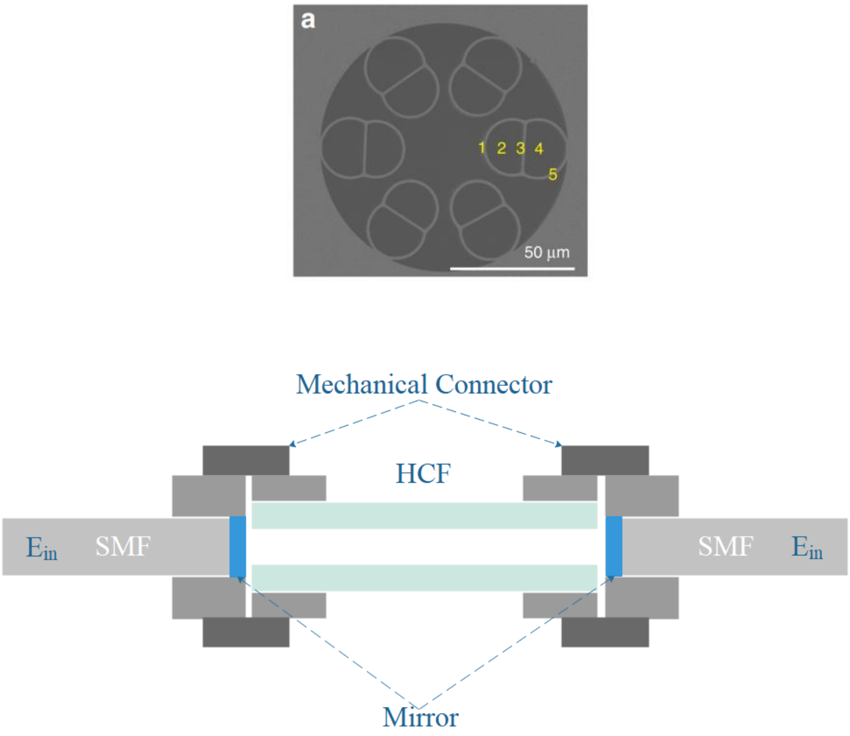

Figure 6.6 (a) SEM of the HCF [10]. (b) Schematic of an HCF FP cavity.

Fig. 6.6 presents the structure of a FP cavity gas cell utilizing HCF. The HCF employed here is a AR-HCF with interconnected tubes, featuring a core diameter measuring 30.5 µm [10]. A visual representation of the HCF cross-section is accessible in Fig. 6.6(a). This HCF exhibits multiple transmission bands, namely 700–810 nm, 900–1200 nm, and 1320–1700 nm, as shown in Fig. 6.7. At 1542 nm, the transmission loss stands around 5 dB/km.

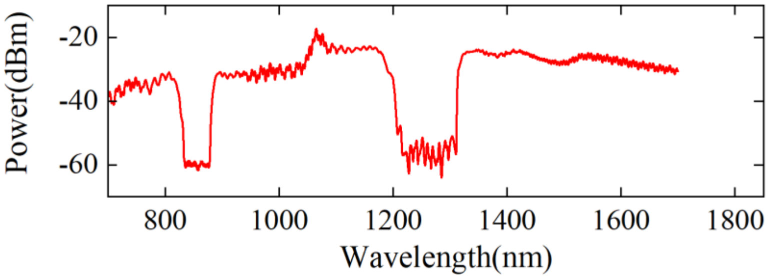

Figure 6.7 The transmission spectrum of the HCF

The FP cavity is constructed by confining a roughly 8-centimeter-long HCF between the reflective terminations of two standard single-mode fibers (SMFs). The connection between SMFs and the HCF is achieved via mechanical splicing, incorporating minute air gaps (~1 μm) that aid in the gas filling process within the hollow core.

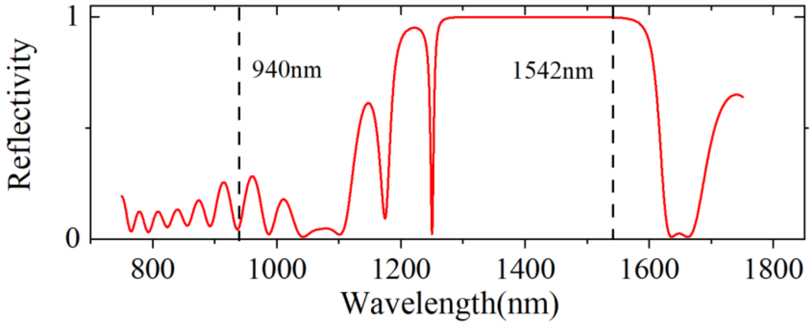

Figure 6.8 The reflectivity of the mirror

The wavelength-dependent reflectivity of the mirror's end is depicted in Fig. 6.8. Reflectivity exceeds 99.5% in the 1250 - 1570 nm range, facilitating the creation of a high finesse HCF FP cavity within this wavelength ranges. At pump wavelength of 940 nm, the reflectivity is about 4% and the gas cell can be regard as a single-pass one.

Figs. 6.9 and 6.10 illustrates the transmission of the HCF cavity near 1542 nm, the chosen probe wavelength (Stokes light) for our study. With a FSR approximating 1.87 GHz and a cavity resonance linewidth of 6.2 MHz, the cavity's finesse is calculated to be around 300.

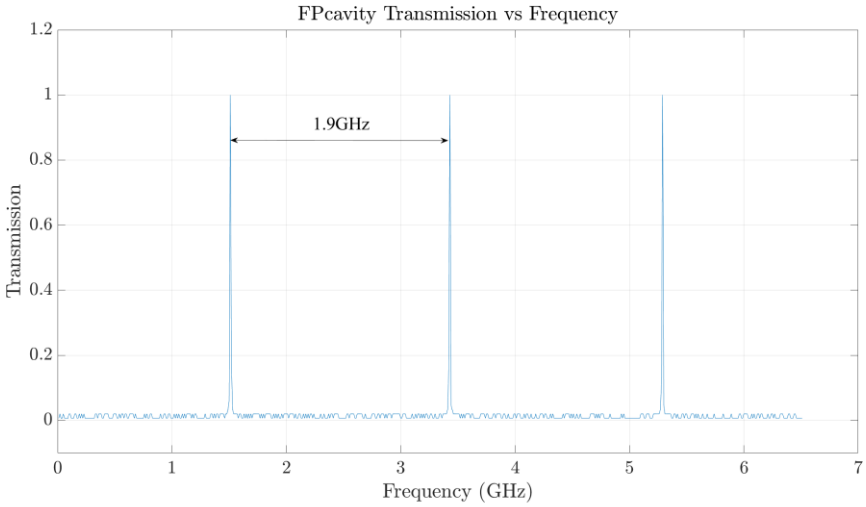

Figure 6.9 Measured transmission when the probe wavelength is scanned around 1542 nm.

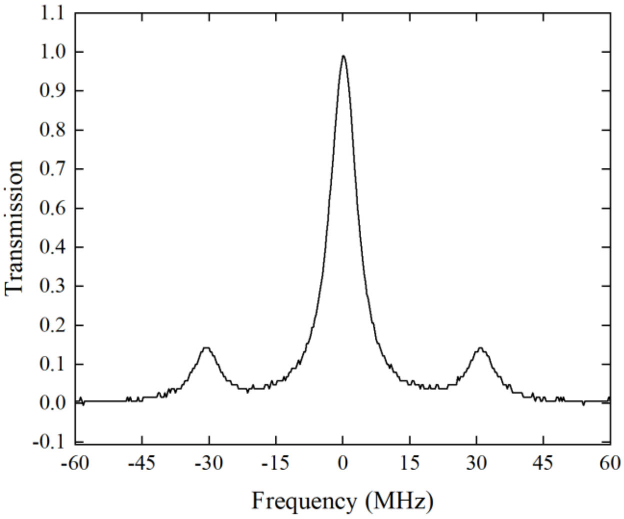

Figure 6.10 A measured single resonance when the probe light is modulated by an electro-optic modulator (EOM) at 30 MHz and scanned.

6.5 Hydrogen detection with CE-SRGS

As shown in the Fig. 6.11, the Raman shift of hydrogen spans a wide range from 350 to 4150 cm^{-1}. We have selected the $Q_1(1)$ transition, which exhibits the maximum Raman gain, with a Raman shift of 4155.84 cm^{-1}. The pump wavelength we used is 940 nm, and the probe wavelength is 1542 nm.

Tight regulation of the probe (or Stokes) wavelength to the center of an HCF-FP cavity resonance is essential for accurate measurements. Fig. 6.12 illustrates the setup for this regulation, which employs an active control loop utilizing the Pound-Drever-Hall (PDH) method [11, 12].

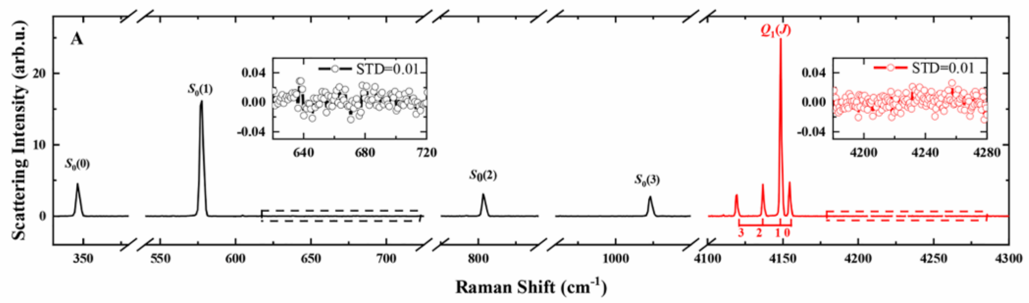

Figure 6.11 Raman spectrum of the rotational and rovibrational bands of hydrogen [13].

Initially, the probe beam is directed into an electro-optic modulator (EOM), where the phase of the probe is modulated at a frequency of Ω= 30 MHz. This modulation is generated by a function generator (FG) and gives rise to two sidebands located outside the resonance of the HCF-FP cavity. The phase-modulated probe beam, with its altered phase, is then guided into the cavity using an optical circulator (OC) and a polarization controller (PC). Due to the residual birefringence of the HCF cavity, the cavity's resonance is sensitive to the polarization state of the incident light. To address this, we utilize polarization controllers to adjust the polarization state of the incoming light beam, aligning it with one of the eigen-polarization states of the HCF cavity. This ensures optimal coupling and resonance conditions.

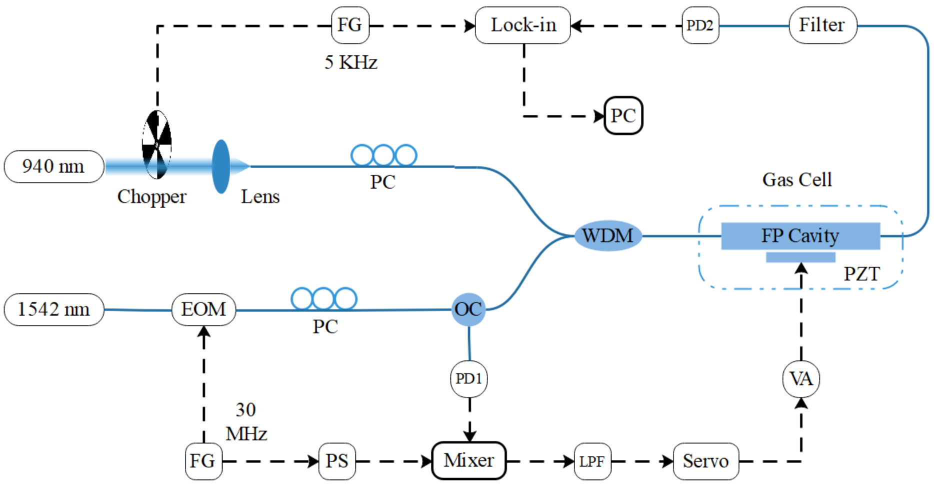

Figure 6.12 The experiment set-up. EOM, Electro-optic modulator; FG, function generator; PC, polarization controller; PS, phase shifter; OC, optical circulator; PD1,2, photodetector 1,2; LPF, low-pass filter; VA, voltage amplifier; PZT, piezo-electric transducer; PC, personal computer.

The probe beam, reflected from the HCF-FP cavity, is picked up by a photodetector 1 (PD1) with a 150 MHz bandwidth. The output of PD1 is combined with the radio frequency signal from the FG. The mixer's output's AC component is removed with a low pass filter (LPF) to produce a DC error signal. This signal is relayed to the PDH control loop to manage the probe wavelength.

The PDH control loop's output is boosted by a voltage amplifier (VA) to stimulate the HCF cavity's piezoelectric tuning mechanism. This adjustment aligns its resonance center with the wavelength of Stokes light through adjusting the length of FP cavity. PD2 monitors the HCF-FP cavity's transmission to check if the cavity length is properly adjusted.

Fig. 6.13 presents both the recorded error signal and the cavity transmission as the probe wavelength is altered across a cavity resonance. Fig. 6.14 shows the cavity transmission when the probe wavelength is precisely locked to the center of an HCF-FP cavity resonance.

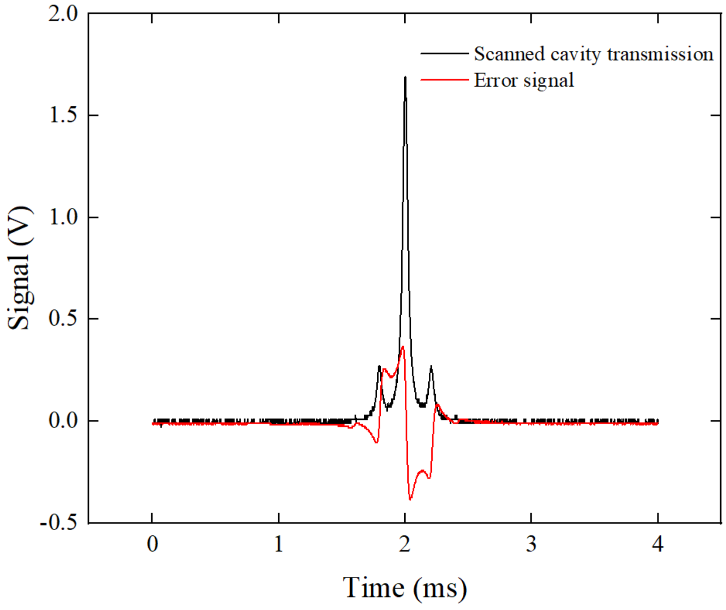

Figure 6.13 The measured error signal and cavity transmission around a cavity resonance.

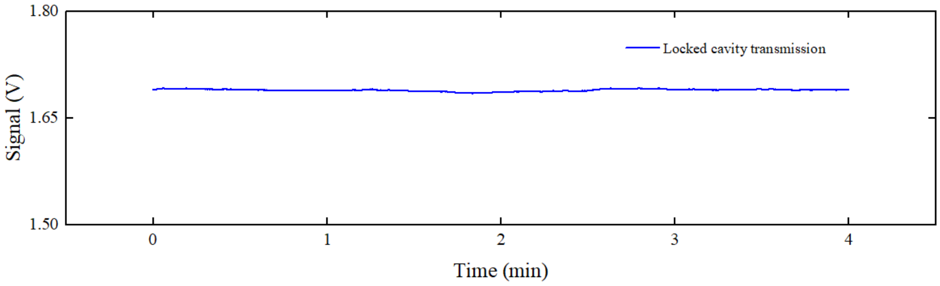

Figure 6.14 The measured cavity transmission when the probe wavelength is precisely locked to the center of an HCF-FP cavity resonance.

The set-up portrayed in the Fig. 6.12 is designed for the detection of hydrogen gas using CE-SRGS. It is comprised of two laser sources. The first one, known as the pump laser, originates from a tunable Tapered Amplifier Laser supplied by Toptica. This laser operates at a wavelength of 940 nm and can deliver an output power up to 1W with a beam size of around 3 mm. The second laser, also referred to as the probe light or the Stokes light, is an ECDL from Toptica. It possesses a tunable wavelength and boasts a linewidth smaller than 10 kHz which is important for cavity locking. The wavelength of the probe laser is set to a fixed value around 1542 nm. Then, by employing the previously mentioned PDH locking technique, the HCF cavity fitted with a PZT is locked onto the probe laser's wavelength, which is approximately 1542 nm. The pump laser, operating at 940 nm, scans across the $Q_1(1)$ Raman line of hydrogen gas at 4155.84 cm^{-1}, thanks to its in-built wavelength scanning system. Concurrently, the intensity of the 940 nm laser is modulated at 5 kHz via a mechanic chopper. The transmission signal from the FP cavity is detected by a PD2. The PD2 signal is then demodulated at 5 kHz using a LIA.

6.5.1 Experiment results

The conducted experiment entailed the precise measurement of hydrogen gas under controlled laboratory conditions—operating at a steady temperature of 298 K and a pressure equivalent to a standard atmospheric pressure. The gas samples are obtained via the controlled admixture of pure hydrogen and nitrogen, regulated meticulously by a flow control valve. Prior to the engagement of these samples, the effective pump power was accurately measured at the input end of the HCF. A chopper was employed to execute a 5 kHz intensity modulation, while demodulation—occurring at the primary harmonic, or at 5kHz—was achieved through lock-in. We fixed the probe light (also known as Stokes light) at a wavelength of 1542 nm, while the pump light resided in the vicinity of 940 nm. This corresponded to a Raman shift of 4155.8 cm^{-1}. Consequently, a scanning operation revealed the unique Raman signal of the hydrogen gas.

During this process, a lock in time constant (TC) of one second was employed. Fig. 6.15 elegantly demonstrates the robust linear relationship between the signal and gas concentration. This was observed when the pump power was fixed at 180 mW, and hydrogen gas concentrations were varied between 25% and 5%.

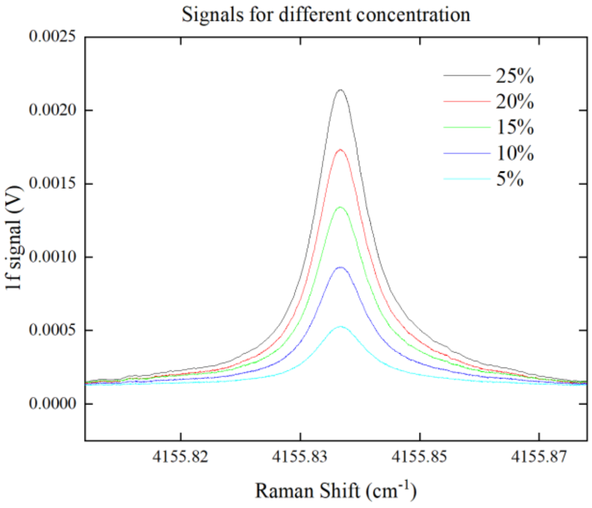

(a)

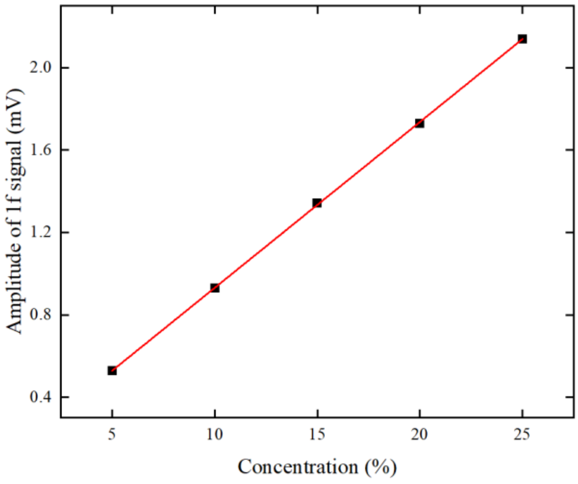

(b)

Figure 6.15 The lock-in output for different concentrations of hydrogen. (b) The relationship between signal amplitude and the concentration of hydrogen.

Moreover, in Fig. 6.16, with a constant hydrogen gas concentration of 25%, we varied the pump power from 180 mW to 37 mW. The amplitude of the signal maintained a favorable linear relationship with power. Interestingly, the signal's baseline demonstrated a similar trend, decreasing with the diminishing pump power, thereby hinting at the potential correlation between signal background and pump power—an observation meriting future exploration.

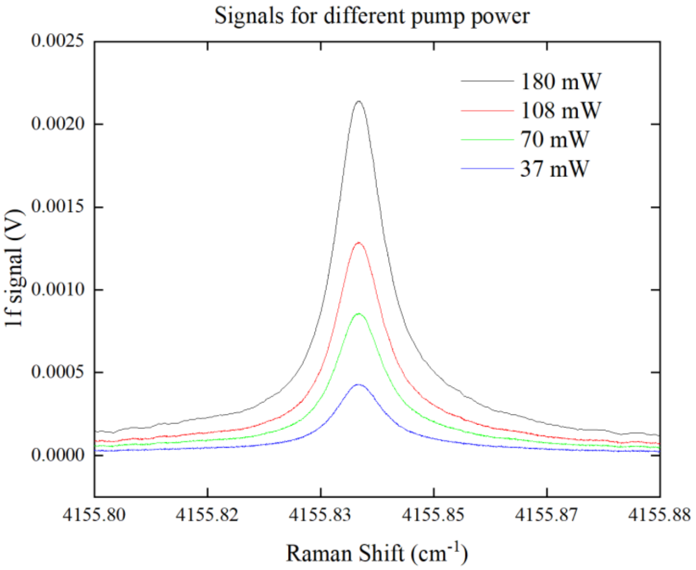

(a)

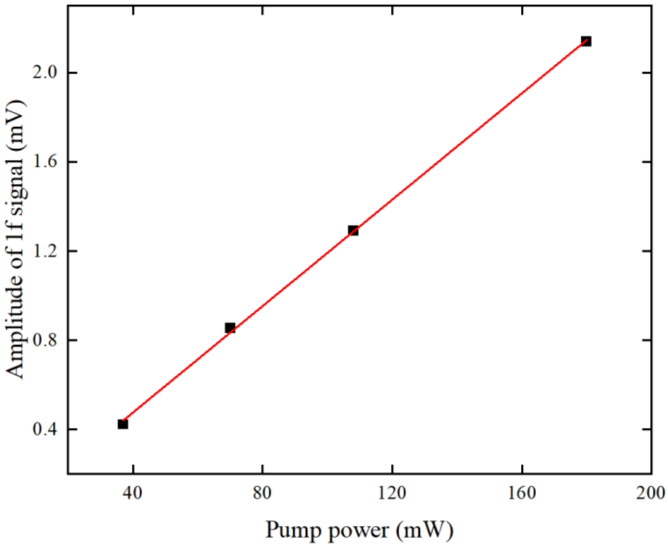

(b)

Figure 6.16 (a)The lock-in output for different pump power. (b) The relationship between signal amplitude and pump power.

Our earlier simulations concerning the Raman gain coefficients highlighted their association with the polarization states of both the pump light and Stokes light. When the polarization was parallel, Raman gain peaked, whereas it was minimal with perpendicular polarization—a roughly tenfold disparity observed at one atmospheric pressure.

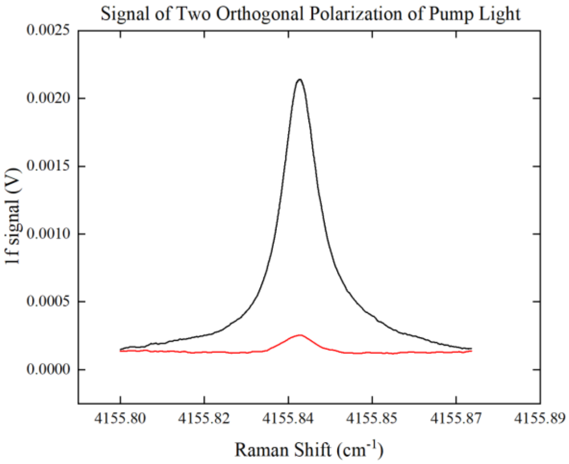

Figure 6.17 The maximum and minimum of lock-in outputs when adjusting the polarization of pump light.

Fig. 6.17 encapsulates this observation. Here, we set the pump power at 180 mW with a hydrogen gas concentration of 25% and manipulated the pump light's polarization controller to attain maximal and minimal Raman signals. The difference between the two signal intensities corroborated theoretical predictions, exhibiting a tenfold variation. The signal baselines appeared remarkably similar.

Recognizing that we employed intensity modulation, we found that the signal waveform mirrored that of the Raman line. Hence, we carried out Gauss and Lorentz fitting on the signal. The Lorentz line fitting, depicted in Fig. 6.18, aligned perfectly with the theoretical prediction. At lower pressures, Doppler broadening led to a Gaussian line shape function; however, at normal pressure, collision broadening resulted in a Lorentz line shape function. The fitted linewidth (~370MHz) resonated closely with the theoretically computed value of 355MHz.

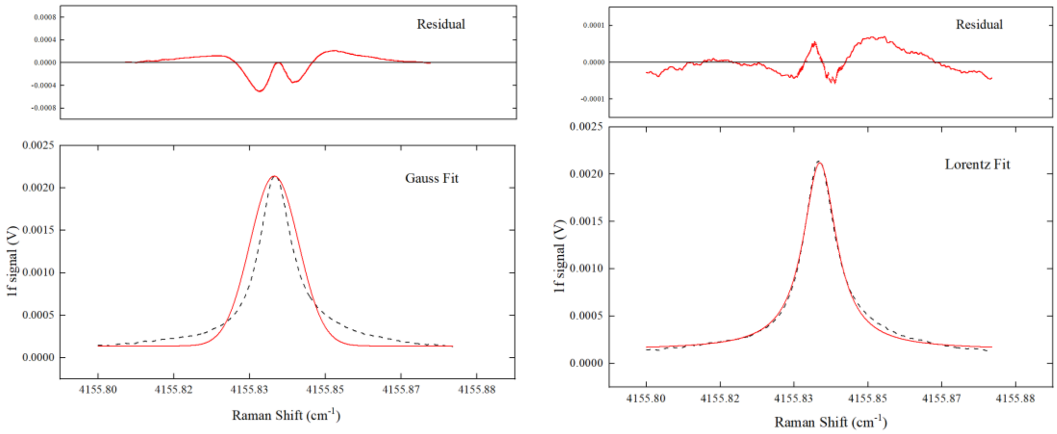

Figure 6.18 Gauss and Lorentz fit of the measured Raman signal.

Finally, to assess system noise, we introduced pure nitrogen into the gas chamber while keeping other parameters unchanged. Noise was recorded over a span of two minutes, yielding a standard deviation of 0.53 µV, which enabled a SNR computation of ~ 4000 and a NEC of 62 ppm for one second TC. Allan deviation analysis is performed and the result is shown in Fig. 6.20. The noise goes down to 0.26μV with an averaging time of ~ 90 seconds, which corresponds to a NEC of 30 ppm.

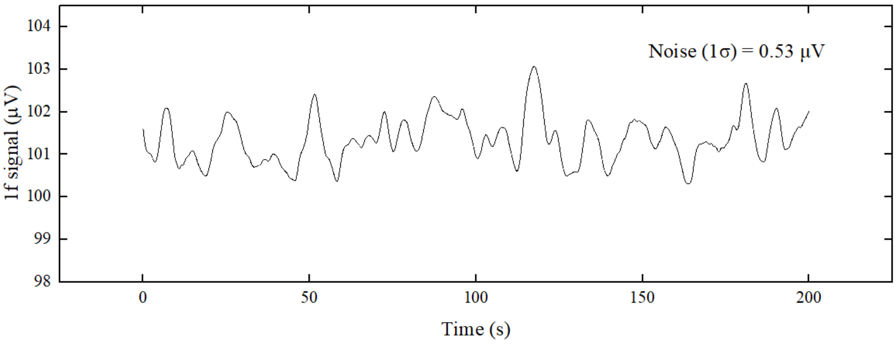

Figure 6.19 The lock-in output when the gas cell is filled with pure nitrogen for a period of 200 seconds.

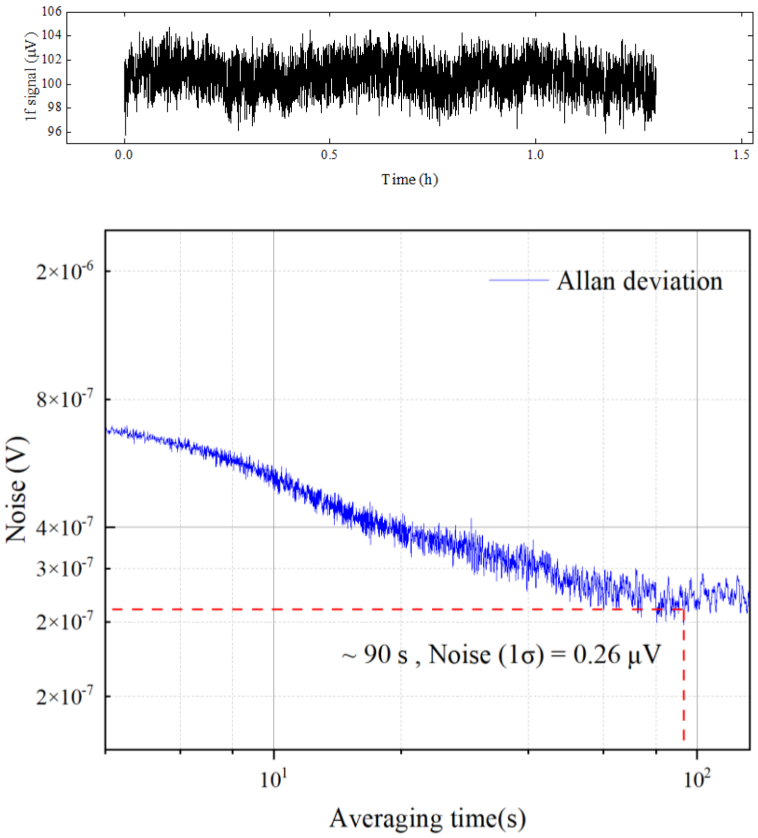

Figure 6.20 The upper panel is the lock-in output with the TC = 100 ms over a period of 1.25 h. And the lower panel is the result of Allan analysis.

6.6 Discussion and conclusion

Table 6.1 Hydrogen sensors based on HCFs.

	Spectroscopy	HCF (core diameter)	Length	Pressure	NEC (TC)
Hydrogen[6]	SRG	PBF (11 μm)	15 m single pass	1.6 bar	141 ppm (1s)
Hydrogen [14]	SRD	PBF (11 μm)	7 m single pass	3.5 bar	25 ppm (1s)
Hydrogen [15]	RPTS	AR-HCF (28 μm)	3.9 m single pass	6 bar	69 ppm (1s)
Hydrogen [this work]	CE-SRGS	AR-HCF (30 μm)	0.08 m (F/π=95)	1 bar	62 ppm (1s)

SRD, stimulated Raman induced dispersion; RPTS, Raman photothermal spectroscopy.

We have detailed several hydrogen gas measurement systems leveraging HCFs, each characterized by critical parameters such as optical path length, core diameter of the hollow-core fiber, experimental pressure, and ultimate detection limit. Impressively, our sensor achieves a detection limit comparable with the best existing sensors, given the same TC.

Deriving from theoretical formula [16]:

$$\Delta I_s / I_s = g_R I_P L \propto \alpha_P A_{eff}^{-1} P_{Pump} C L \tag{6.11}$$

Where α_P is the fractional power in the air and for HCF, it is more than 95%. A_{eff} is the MFA, P_{pump} is the pump power; L is the gas-light interaction length.

Raman gain signal exhibits a positive correlation with gas concentration and optical path length, as well as with the density of the pump light power. This implies that, under the same pump light power, a larger MFA results in lower power density and thus, a smaller Raman gain.

We employ an AR-HCF with a diameter three times that of conventional HC-PBFs, indicating an approximate tenfold reduction in Raman gain. That's why we chose the strongest Raman line, but the LOD is similar to the previous best sensor. However, our sensor has other advantages. The compact size of our sensor, merely 0.08 cm long, offers considerable advantages in both volume and response time. Moreover, cavity enhancement technology allows our sensor's equivalent optical path to reach 8 m, comparable to other sensors. We conduct our experiments under ambient pressure, contrasting with most other sensors that require high-pressure conditions.

Our Raman gain simulations indicate that below 10 bar, Raman gain is essentially proportional to pressure. Therefore, this suggests that our current system can further enhance its sensitivity by applying higher gas pressure.

In addition to increasing pressure, another viable approach to improve our system's sensitivity involves replacing the mechanical chopper with a fiber-optic Acousto-Optic Modulator (AOM). This enhancement is based on two main considerations. Firstly, our current mechanical chopper operates at a low modulation frequency of 5 kHz. This operation creates significant audible noise from the mechanical structure, thereby introducing interference in our system. Furthermore, at this relatively low frequency, the presence of certain low-frequency noise is still observed. In most SRGS-based sensors, the modulation frequency of pump light above 50 kHz are commonly utilized. Secondly, the issue of power attenuation arises from the size discrepancy between the mechanical structure and the beam spot. Specifically, our mechanical chopper's aperture is at 2 mm, which is inadequate for our beam spot size that exceeds 3 mm.

Considering these factors, adopting a fiber-optic AOM for intensity modulation presents an attractive solution. This would not only provide a quieter operational environment but also ensure a higher frequency modulation, thereby further improving the detection limit.

In conclusion, we have demonstrated HCF CE-SRGS for hydrogen detection. By employing a 0.08 m long HCF and two SMFs with high-reflection coated end faces, we assembled an HCF cavity boasting a finesse of 300. We utilized the PDH method to stabilize the cavity on a narrow linewidth probe laser at 1542 nm. Concurrently, the pump light, intensity modulated and tuned near 940 nm, was aligned to the $Q_1(1)$ Raman line of hydrogen. The signal is demodulated at 5 kHz using a LIA, and a NEC of 62 ppm for hydrogen with a TC of 1 second is achieved under 1 atm and room temperature. Further, Allan deviation analysis revealed an improved NEC of 30 ppm over an averaging time of 90 seconds. The NEC is comparable to the best existing hydrogen sensors. This cavity-enhanced technique can be used for the other spectroscopy using HCF.

6.7 Reference

1. D. N. Kozlov, M. C. Weikl, J. Kiefer, T. Seeger, and A. Leipertz, "Two-photon stimulated Raman excitation of thermal laser-induced gratings in molecular gases using broadband radiation of a single laser," Optics Express **16**, 18379-18389 (2008).
2. M. P. Buric, K. P. Chen, J. Falk, and S. D. Woodruff, "Enhanced spontaneous Raman scattering and gas composition analysis using a photonic crystal fiber," Appl. Opt. **47**, 4255-4261 (2008).
3. J. L. Doménech, and M. Cueto, "Sensitivity enhancement in high resolution stimulated Raman spectroscopy of gases with hollow-core photonic crystal fibers," Optics letters **38**, 4074-4077 (2013).
4. P. G. Westergaard, M. Lassen, and J. C. Petersen, "Differential high-resolution stimulated CW Raman spectroscopy of hydrogen in a hollow-core fiber," Optics express **23**, 16320-16328 (2015).
5. S. Hanf, T. Bögözi, R. Keiner, T. Frosch, and J. r. Popp, "Fast and highly sensitive fiber-enhanced Raman spectroscopic monitoring of molecular H2 and CH4 for point-of-care diagnosis of malabsorption disorders in exhaled human breath," Analytical chemistry **87**, 982-988 (2015).
6. F. Yang, and W. Jin, "All-fiber hydrogen sensor based on stimulated Raman gain spectroscopy with a 1550 nm hollow-core fiber," in *2017 25th Optical Fiber Sensors Conference (OFS)*(IEEE2017), pp. 1-4.
7. D. A. Long, "Raman spectroscopy," New York **1** (1977).
8. G. Gagliardi, and H.-P. Loock, *Cavity-enhanced spectroscopy and sensing* (Springer, 2014).
9. M. Maier, W. Kaiser, and J. Giordmaine, "Backward stimulated Raman scattering," Physical Review **177**, 580 (1969).
10. S.-f. Gao, Y.-y. Wang, W. Ding, D.-l. Jiang, S. Gu, X. Zhang, and P. Wang, "Hollow-core conjoined-tube negative-curvature fibre with ultralow loss," Nature communications **9**, 1-6 (2018).
11. R. W. Drever, J. L. Hall, F. V. Kowalski, J. Hough, G. Ford, A. Munley, and H. Ward, "Laser phase and frequency stabilization using an optical resonator," Applied Physics B **31**, 97-105 (1983).
12. E. D. Black, "An introduction to Pound–Drever–Hall laser frequency stabilization," American journal of physics **69**, 79-87 (2001).
13. Q.-y. Yang, Y. Tan, Z.-h. Qu, Y. Sun, A.-w. Liu, and S.-m. Hu, "Multiple Gas Detection by Cavity-Enhanced Raman Spectroscopy with Sub-ppm Sensitivity," Analytical Chemistry **95**, 5652-5660 (2023).
14. H. Bao, W. Jin, Y. Miao, and H. L. Ho, "Laser-induced dispersion with stimulated Raman scattering in gas-filled optical fiber," Journal of Lightwave Technology **37**, 2120-2125 (2019).
15. Z. yan, "High sensitivity spectroscopic gas sensing with hollow-core optical fibers," The Hong Kong Polytechnic University (2021).

16. Y. Qi, Y. Zhao, H. Bao, W. Jin, and H. L. Ho, "Nanofiber enhanced stimulated Raman spectroscopy for ultra-fast, ultra-sensitive hydrogen detection with ultra-wide dynamic range," Optica **6** (2019).

Chapter 7

7 Conclusions and future works

7.1 Conclusions

This thesis investigates gas detection using spectroscopic techniques based on HCF optics.

In chapter 3 of this thesis, we explore the sensitivity enhancement of photothermal spectroscopy for detecting gases that exhibit absorptive properties. Our research presents a significant departure from previous PTS techniques by shifting the focus to absorption lines primarily in the range of two to five micrometers. This spectrum range, which offers stronger absorptivity compared to the previously used range near 1.5 micrometers, corresponds to the intrinsic vibrational absorption bands of many gas molecules. This shift enables better gas detection limits. Using the FPI for phase detection, we detected ethane gas at 3.5 micrometers. With a HCF of 14 cm length, we achieved a LOD of 13 ppb in one second TC. We analyzed the noise sources of the FPI and concluded that increasing the length of the HCF and optimizing the reflectivity of the FP end surface would not necessarily enhance the detection performance, as the main limitation of the FPI system is the laser phase noise.

In chapter 4 of this thesis, following our exploration of the FPI for single gas detection in Chapter 3, we extended the application of the FPI to simultaneously detect three gases: carbon monoxide, carbon dioxide, and water vapor, with hybrid MIR/NIR pumps and FDM. This FDM PTS allowed us to examine the influence of varying water vapor concentration on photothermal signals of carbon monoxide and carbon dioxide, facilitating actual gas concentration computation by compensating for the effect of water vapor concentration on the photothermal signals.

In chapter 5 of this thesis, we demonstrated an approach to improve gas detection sensitivity by implementing a reflective HCF DMI for phase detection. We studied the low-noise characteristics of the DMI and combine it with a MIR pump laser. This novel configuration facilitates a reflective HCF DMI MIR PTS for gas detection. With this approach, we conduct methane detection experiment at 3.2 micrometers. Utilizing a HCF of 1.8 meters in length, we achieved an impressive LOD at ppt level, thereby demonstrating the exceptional sensitivity of our proposed system. We also analyze the noises of the DMI system and find the main source is the intensity noise and the shot noise. The sensitivity of the DMI to external perturbation is found substantially smaller than the FPI.

Chapter 6 of the thesis describes a detection method for gases without weak or no absorption features, such as hydrogen gas, through Raman spectroscopy. We analyzed the impact of different gas pressures and polarization states of lasers on the Raman gain coefficient. By combining the HCF FP cavity with the SRGS, we achieved an enhancement effect of ~100 for the Raman gain signal. Employing intensity modulation at a frequency of 5 kHz, we obtained a hydrogen gas detection limit of 62 ppm with 1 s TC and 8-cm-long HCF, which is comparable to the best existing hydrogen sensors using HCFs.

7.2 Future works

This thesis presents highly sensitive laser spectroscopy techniques based on HCFs with photothermal and stimulated Raman spectroscopy. Regarding the fabrication process of the fiber gas cells and optical cavity, as well as the sensitivity and stability of gas detection systems, there are aspects that can be further explored and improved.

For the FPI in chapters 3 and 4:

1. Further studies should focus on enhancing the stability of the FPI, a type of reflective laser interferometer. Parasitic interference within the system could affect the stability

of signal detection, necessitating comprehensive assessment and exploration of novel demodulation techniques such as white-light interferometry.

2. It's also important to investigate the impact of environmental temperature on the detected signal, including the locking stability and the fringe contrast of the FPI, and the photothermal signal itself. Systematic exploration is required over the temperature range typical for practical field applications.

3. The alignment process between the SMF and HCF warrants further exploration. The current complex fabrication process involves the use of a five-axis stage for precise alignment and the thermal broadening technique for mode-field matching to reduce insertion loss and excitation of higher-order modes. Future work could focus on simplifying this process while enhancing the stability of the structural configuration.

For the DMI in chapter 5:

1. To avoid the usage of longer fibers, the cavity enhancement method for both modes may be considered. This method aims to achieve a substantial effective gas-light interaction length with shorter HCF, requiring a suitable HCF that exhibits minimal loss for both LP_{01} and LP_{11} modes.

2. Efficient excitation of higher-order modes within the HCF is a valuable area of investigation. Future work could consider utilizing a fiber mode selector and a few-mode fiber as the HCF's input fiber to achieve more efficient excitation of LP_{11} mode.

For the Raman spectroscopy in chapter 6:

1. An interesting finding from our experiment is that the cavity has two orthogonal polarization modes that respond maximally and minimally to Raman gain. Thus, we could extract the Raman signal via differential gain between the polarization modes. Further experiments could explore whether this method could assist in noise reduction.

2. The noise-immune cavity-enhanced technique, which was previously studied with free-space optics, could be used to enhance the signal within the HCF cavity.